UNIVERSITY OF OKLAHOMA

GRADUATE COLLEGE

WAVEFORM AND TRANSCEIVER OPTIMIZATION FOR MULTI-FUNCTIONAL AIRBORNE RADAR THROUGH ADAPTIVE PROCESSING

A DISSERTATION

SUBMITTED TO THE GRADUATE FACULTY

in partial fulfillment of the requirements for the

Degree of

DOCTOR OF PHILOSOPHY

By

SHANG WANG
Norman, Oklahoma
2013

WAVEFORM AND TRANSCEIVER OPTIMIZATION FOR MULTI-FUNCTIONAL AIRBORNE RADAR THROUGH ADAPTIVE PROCESSING

A DISSERTATION APPROVED FOR THE
SCHOOL OF ELECTRICAL AND COMPUTER ENGINEERING

BY

Dr. Yan Zhang, Chair

Dr. Robert Palmer

Dr. Tian-You Yu

Dr. Joseph Havlicek

Dr. S Lakshmivarahan

Acknowledgments

I would like to thank my advisor, Dr. Yan Zhang, for providing this opportunity for me to study at the University of Oklahoma. His constant encouragement and valuable advices are essential for the completion of this dissertation. I will always be inspired by his enthusiasm and passion in research. I also deeply appreciated his support on helping me and my family overcome many difficulties we went through.

I would like to thank my committee members, Dr. Robert Palmer, Dr. Tian-You Yu, Dr. S Lakshmivarahan and Dr. Joseph Havlicek, for taking their time to serve on my committee and for the excellent classes they offered, which benefit me a lot for my research work. I am also thankful for members in RIL and ARRC, who have worked with me, helped me and inspired me during my study at OU.

Last but not least, I would like to thank my family, my lovely wife, Ying, for her understanding and support throughout the past few years; my cute baby daughter, who makes me work with passion each day; my parents, their unconditional support has always helped me in all my endeavors.

Contents

List Of Tables

List Of Figures

Abstract

Pulse compression techniques have been widely used for target detection and remote sensing. The primary concern for pulse compression is the sidelobe interference. Waveform design is an important method to improve the sidelobe performance. As a multi-functional aircraft platform in aviation safety domain, ADS-B system performs functions involving detection, localization and alerting of external traffic. In this work, a binary phase modulation is introduced to convert the original 1090 MHz ADS-B signal waveform into a radar signal. Both the statistical and deterministic models of new waveform are developed and analyzed. The waveform characterization, optimization and its application are studied in details. An alternative way to achieve low sidelobe levels without trading off range resolution and SNR is the adaptive pulse compression - RMMSE (Reiterative Minimum Mean-Square error). Theoretically, RMMSE is able to suppress the sidelobe level down to the receiver noise floor. However, the application of RMMSE to actual radars and the related implementation issues have not been investigated before. In this work, implementation aspects of RMMSE such as waveform sensitivity, noise immunity and computational complexity are addressed. Results generated by applying RMMSE to both simulated and measured radar data are presented and analyzed. Furthermore, a two-dimensional RMMSE algorithm is derived to mitigate the sidelobe effects from both pulse-compression processing and antenna radiation pattern. In addition, to achieve even better control of the sidelobe level, a joint transmit and receive optimization scheme (JTRO) is proposed, which

reduces the impacts of HPA nonlinearity and receiver distortion. Experiment results obtained with a Ku-band spaceborne radar transceiver testbed are presented.

Chapter 1

Introduction

1.1 Introduction

Most of the modern radar systems employ a pulsed waveform which provides range information accurately. For a point target, the relationship between range R and delay T is

$$R = \frac{c \cdot T}{2} \tag{1.1}$$

where c is the speed of light. A longer pulse width can achieve a larger maximum detection range, since the energy in the pulse is increased. A narrower pulse width corresponds to a better range resolution. With a signal bandwidth B, the range resolution r is expressed as (Levanon and Mozeson 2004)

$$r \approx \frac{c}{2B} \tag{1.2}$$

It is also known that the Doppler resolution is inversely proportional to the pulse width T. Radar ambiguity principle states that the spectral content of the signal determines the range resolution and the temporal structure of the signal determines the Doppler resolution. In addition, to increase the radar measurement accuracy and target sensitivity, high pulse energy is required (Skolnik 2002). Therefore, to enhance radar sensing performance, transmit signals with large time-bandwidth-energy product are required.

In general, more signal energy can only be achieved by increasing the pulse duration due to limited peak transmit power, especially for the modern solid state transmitters (Skolnik 2008). Fig. 1.1 shows the long and short pulse comparison. A long pulse with frequency or phase modulation can have the same spectral bandwidth as a short pulse. The modulated long pulse with increased bandwidth B is compressed by the receiver to a width equal to $1/B$. This process is referred to as *pulse compression*. Pulse compression allows a radar to achieve the energy of a long pulse and the resolution of a short pulse simultaneously.

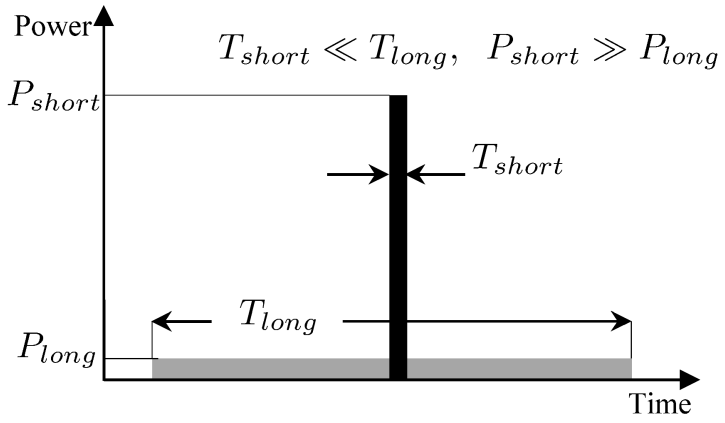

Figure 1.1: Radar long and short pulses. The two pulses have the same energy, i.e. $P_{short} \cdot T_{short} = P_{long} \cdot T_{long}$

The main drawback of traditional pulse compression is the impact of range (or time) sidelobes, which can be mistaken for targets or can mask nearby weaker targets. To achieve acceptable range sidelobe levels, additional waveform design and filtering need to be considered.

In airborne and spaceborne applications, pulse compression has been widely used for weather and surface remote sensing, while strong sidelobes generated by ground or sea surface have affected the observations (Griffiths (1993); Tanner et al. (1994)). The

NASA Ku-band Precipitation Radar (PR) for the Tropical Rainfall Measuring Mission (TRMM) satellite requires about -70 dB sidelobe level for rainfall detection (Fischman et al. 2005). Conventional windowing technique can achieve such a low sidelobe level by trading off range resolution and SNR. Other popular pulse compression techniques such as nonlinear frequency modulation and phase coding can only achieve up to -50 dB sidelobe without degradation of range resolution (Collins and Atkins (1999); Levanon (2005)).

Signal processing techniques have also been used to develop sidelobe mitigation filters. Inverse filters, which have a frequency response similar to the inverse response the transmitted waveform, have been studied in (Daniels and Gregers-Hansen 2005). Optimal mismatched filters have been derived by a constrained Least-Squares approach (Ackroyd and Ghani 1973).

Recently, a new approach based on minimum mean-square error (MMSE) formulation has been proposed in (Blunt and Gerlach 2006). This method is called RMMSE (Re-iterative MMSE) since the sidelobe mitigation is performed iteratively. RMMSE is a Least-Square based algorithm and has superior sidelobe mitigation performance compared to conventional pulse compression techniques. However, the application of RMMSE to practical radars remains uncertain. Implementation aspects of RMMSE such as waveform sensitivity, noise immunity, computational complexity as well as the feasibility to weather observation have to be addressed. The nonlinear distortion of the Solid-State Power Amplifier (SSPA) has been known to have impact on the sidelobe mitigation performance (Vincent et al. 1996). In addition, there are other nonlinear distortions existing in the radar transmit/receive chain. These distortions have to be characterized and suppressed to achieve stringent sidelobe requirement.

In this work, sidelobe mitigation algorithms and their implementations for pulse compression are addressed from the perspective of radar system design. First, the

sidelobe mitigation is explored in terms of optimal waveform design followed by an example of designing and optimizing binary phase-coded waveform. Then, the RMMSE algorithm is studied and implemented to practical radar data. Last, to achieve better control of the sidelobe level, joint transmitter and receiver optimization is investigated, the distortion effects, including HPA nonlinearity and receiver distortion are extracted and modeled. Fig. 1.2 summarizes the structure of the dissertation.

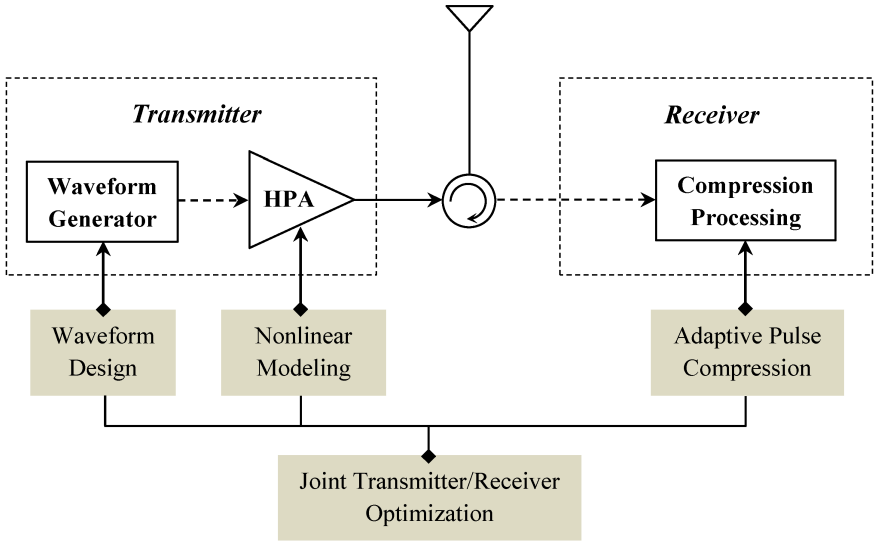

Figure 1.2: The structure of the dissertation

1.2 Organization of the Dissertation

The dissertation is organized as follows:

- **Chapter 2** reviews the basic concept of pulse compression and estimation theory. The applications of pulse compression in solid-state radar systems for both hard and distributed targets are described. Previous work on pulse compression and transceiver optimization is summarized.

- **Chapter 3** discussed the multi-functional radar waveform design methodology. First, conventional methods of pulse compression by waveform optimization are summarized. Then the importance of multi-functional radar waveforms are emphasized. In aviation safety domain, ADS-B system has both communication and non-cooperative target sensing functions. We establish a theoretical foundation of non-cooperative target detection using modulated transponder signal waveform - PPM/PM. Both the statistical and deterministic models of PPM/PM waveform are developed and analyzed. Waveform characterization, optimization and its application are studied in details.

- **Chapter 4** discussed the theory and application of adaptive pulse compression algorithm - RMMSE (Reiterative Minimum Mean-Square error). Techniques to mitigate the sidelobe effects from both pulse-compression processing and antenna pattern are discussed and Two-dimensional least-square (2D-LS) and (2D-RMMSE) algorithms are derived and applied to scenarios containing both hard targets and distributed weather targets. Simulation results based on realistic weather model outputs and scattering models are presented. Implementation issues of RMMSE are discussed with its application to practical radar data from *PX1000* and *HiWRAP*.

- **Chapter 5** proposed a novel adaptive Joint Transmitter and Receiver Optimization (JTRO) scheme. First, nonlinear distortion and its impact on sidelobe mitigation are analyzed. Then a new Kernel-based nonlinear filtering algorithm - KLMS is discussed and applied to nonlinear distortion modeling. The concept of JTRO is proposed and implemented on a Ku-band spaceborne radar transceiver testbed. Experiment results are presented followed by discussion of aspects about implementations.

- **Chapter 6** concludes the dissertation and provides future research directions.

Chapter 2

Theory and Systems of Solid-State Radars

The applications of the solid-state transmitter, pulse compression, and multi-channel antennas have become important trends of multi-mission radar sensing (Ohora and Bech (2005); Salazar et al. (2008); Heimmer (2008); Zhang (2008); Wada et al. (2009)). Extreme requirements from Unmanned Systems such as unmanned aerial system (UAS) and satellites demand small, integrated, and multi-functional radar sensor systems. In NASA's space precipitation measurement mission, a -70 dB peak sidelobe level without signal-to-noise ratio loss is required. This necessitates the use of high-performance, high-efficient and high-power solid-state transmitters. The rapid advances in the field of solid-state electronic also make feasible the integration of radar/communications systems (Hussain (2007); Thompson and Stralka (2009)). Therefore, the *size*, *weight* and *power* (SWaP) constrained designs are required to address the various challenges in modern solid-state radar systems.

2.1 Solid-State Transmitters

Recently, in commercial applications, solid-state technology has dominated the transmitters operating at VHF and below and started to migrate to higher frequency region gradually. (Skolnik 2008) listed some of the advantages of solid-state over conventional transmitters:

- **Size and cost**: The transistor amplifiers operate at much lower voltages; therefore, power supply voltages are at the order of volts rather than kilovolts, which save space and cost. This in turn make it more reliable and easier to maintain.

- **Reliability**: Transmitters designed with solid-state devices exhibit improved meantime between failures in comparison with tube-type transmitters.

- **Bandwidth**: Solid-state transmitter can achieve 50% more fractional bandwidth with acceptable power-added efficiency (PAE).

- **Integration**: A module with both transmit and receive path amplifiers, phase shifters, switches and attenuaters can be achieved. Such integration is crucial for phased array radar system.

One drawback of the solid-state radar is that the transmitted power is limited compared to the conventional high-power transmitter such as TWTs (Traveling-Wave Tube), klystrons and magnetrons. At around 10 GHz operation frequency, the typical transmit power is about several hundred of Watts for GaN (Gallium Nitride) HEMT (High Electron Mobility Transistor) and GaAs (Gallium Arsenide) PHEMT (Pseudomorphic HEMT) amplifiers. (Skolnik 2008). The required higher power levels can be achieved by combining transistors and transistor amplifier modules in parallel, which significantly increase the cost. In practice, the solid-state PA can be more efficiently operated at low peak power and large duty cycle. This usually requires the use of *pulse compression* to provide desired unambiguous range coverage together with improved range resolution. A good pulse compression algorithm is essential to the signal processing of pulse compression. One issue of solid-state power amplifier is that it degrades the performance of pulse compression when operating in saturation region. This will be addressed in Chapter 5. Throughout this work, we focus on minimizing the range sidelobe level via properly-designed waveforms, adaptive sidelobe mitigation and joint transmit/receive optimization algorithms.

2.2 Solid-State Radars Systems

2.2.1 General Architectures of Solid-State Radars

In terms of system architecture, solid-state radars are not quite different from conventional pulsed-Doppler radars using TWT transmitters. The modern Doppler radars consist of local oscillators, signal generator, power amplifier, receiver, up/down converters, antenna, digital signal processor, etc. Fig. 2.1 shows a typical configuration of a pulsed-Doppler radar utilizing digital signal processing, which is controlled by a mission processor (Skolnik 2008). This system requires coherent processing for doppler detection. The *in-phase* (I) and *quadrature* (Q) components at baseband represent the real and imaginary parts of the receive signal. The main oscillator provides a stable reference sinusoid on which the system coherency is based. The antenna is designed to be scanned mechanically or electronically. Modern Doppler radars have evolved to the use of active electronically scanned arrays (AESAs) (Hommel and Feldle 2005). A duplexer is required so that the same antenna is used for both transmit and receive. It can be a circulator or high-isolation switch. The digital IF-sampled output of the receiver is downconverted to the baseband via a digital product detector.

The I and Q signals are passed through the matched filter (MF). This radar system adopts Doppler filter bank for main-beam clutter rejection and coherent integration. The filter bank is usually realized by using the fast Fourier transform (FFT). Proper window weighting is used to reduce the filter sidelobes. The pulse compression modulation can be used on the transmit pulse to increase target sensitivity and improve range resolution. After the Doppler filter bank, the pulse compression is performed digitally in the receiver. This will ensure the Doppler effect on the pulse compression is included during the filter design stage. This is important because the doppler effect does have the same impact on the pulse compression algorithm (MF, RMMSE and

Mismatched Filter). The optimal performance of pulse compression can be achieved with the prior knowledge about the doppler shift.

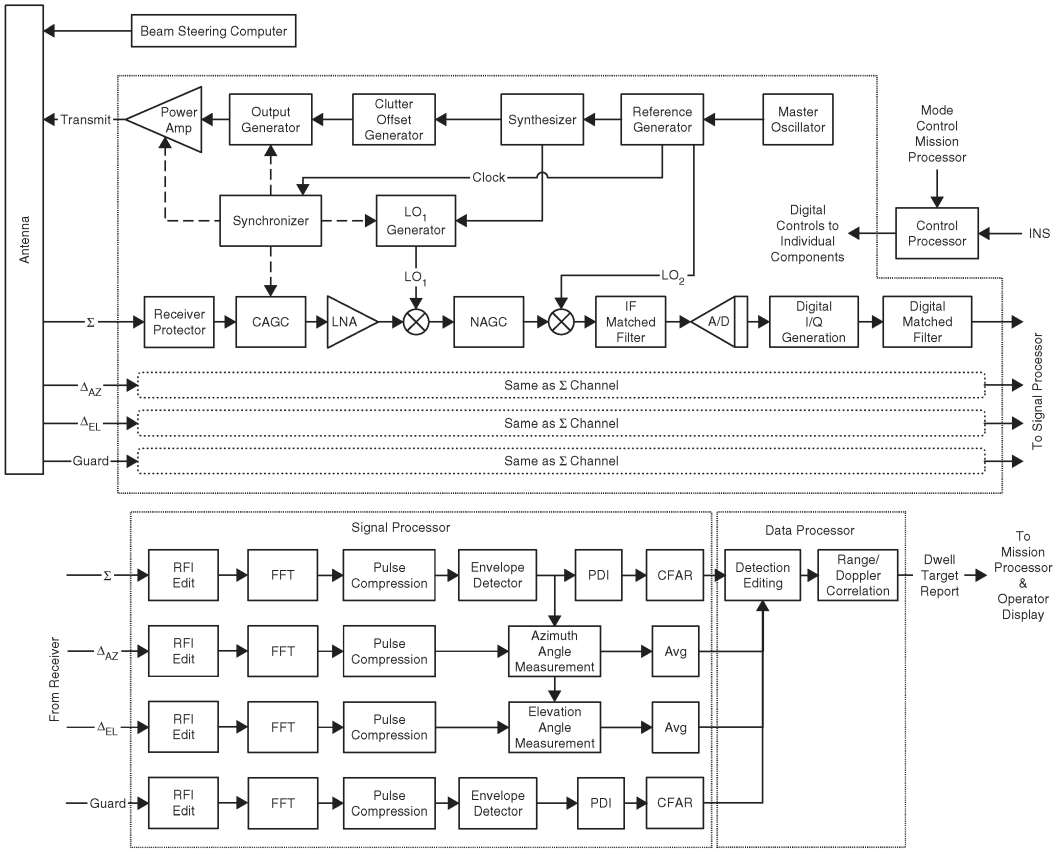

Figure 2.1: Diagram of a typical pulsed-Doppler target tracking radar (Skolnik 2008)

2.2.2 Solid-State Radars for Observing Hard Targets

2.2.2.1 Characterization of hard-targets

Limited number of point-targets constitutes hard targets such as buildings, signal towers, aircrafts, etc. For a solitary point target (a point target is a target having small dimensions compared to the angular and range resolution of the radar), the

target characteristics are described by radar cross-section (σ^2). The famous radar equation can be expressed as (Skolnik 2002) (single pulse)

$$R^4 = \frac{P_t G A_e \sigma}{(4\pi)^2 k T B F_n (S/N)} \tag{2.1}$$

where P_t is the transmitted power, G is the antenna gain, A_e is the antenna aperture, k is Boltzmann's constant, T is the receiver temperature (in degrees Kelvin), B is the receiver noise bandwidth, F_n is the noise figure and S/N is the signal-to-noise ratio (SNR).

2.2.2.2 Typical Systems

As the most important example for air-traffic control, Airport Surveillance Radars (ASR-9) have been employed since 1990's. ASR is designed for early warning, land and maritime surveillance, weather for aircraft and helicopters (Taylor and Brunins 1985). The next-generation ASR-12 (Cole et al. 1998) is a modular, fully solid-state S-Band radar systems that not only incorporate solid-state technology but also a host of other technological advancements to improve upon the performance capabilities of the current generation of terminal radars. Several new technologies have been implemented in ASR-12: (1) *Pulse compression*. The use of pulse compression is necessary to provide the required range resolution for an ATC radar. The associated sidelobe will be suppressed to $\leq -50dB$ in order to meet the operational requirement for a solid-state ATC radar. (2) *Digital receiver*. The ASR-12 adopts a digital receiver that not only performs digital pulse compression but also forms In-phase and Quadrature (I&Q) components for both long and short pulse returns. Large receiver dynamic range is a key design feature of the ASR-12. The saturation, thus the nonlinear distortion of the pulse prior to compression is a key concern since it has severe impact on range sidelobes. (3) *All solid-state transmitter*. ASR-12 uses precise pulse shaping to reduce spectrum regrowth. Combined RF power amplifiers are employed for transmission to the antenna.

In addition, many of the solid-state radars designed for hard-target detection are phased array systems. The advances in MMIC (Microwave Monolithic Integrated Circuits) technology used in T/R module design have enabled most high-frequency phased arrays. A Multifunction Phased Array Radar (MPAR) system has been proposed as the next generation solution for the Nation's weather and air surveillance needs (Herd et al. 2010). To achieve the ambitious cost targets, highly integrated IC and solid-state technologies are being implemented. In the current MPAR prototypes, the RFICs, control IC and band pass filters are integrated onto a single multi-layer printed circuit board (PCB) using best commercial practices. The critical technologies include dual-polarized balance-feed stacked patch, overlapped digital subarray beamformer, polarization flexible T/R, etc. (Herd et al. 2010). The active phased array techniques for MPAR require the cost reduction for T/R module, which is the most significant aspect of the MPAR design. The estimated total number of T/R modules is about 9000 (Galati et al. 2010). To save power budget of T/R module, MPAR utilizes pulse compression to reduce the peak transmit power to the order of Watts. Therefore, MPAR systems call for a relatively long transmit pulse, i.e. with high duty-cycle to achieve good sensitivity. The low range sidelobes have to be guaranteed (low PSL for point targets, low ISL for distributed targets) (Galati and Pavan 2011). Traditional pulse compression techniques face the problems of range resolution degradation, SNR loss, Doppler tolerance, etc. In this work, novel waveform design and adaptive pulse compression algorithms are introduced and implemented to practical radar data, which provide insights for MPAR project.

2.2.3 Solid-State Radars for Observing Distributed-Targets Sensing

2.2.3.1 Characterization of distributed-targets

For distributed targets such as precipitation, the target characteristics are accounted for in terms of reflectivity. It is a measure of the intensities of precipitation in the scanned volume. Reflectivity is the superposition of the backscattering cross sections weighed by particle size distribution. The weather radar equation is (Doviak and Zrnic 1984)

$$\bar{P}(r_0) = \frac{P_t g^2 \eta c \tau \pi \theta_1^2 \lambda^2}{(4\pi)^3 r_0^2 l^2 16 \ln 2} \tag{2.2}$$

where $\bar{P}(r_0)$ is the weather signal mean power at the antenna, g is the antenna gain, η is the reflectivity, c is the speed of light, τ is the equivalent pulse width, θ_1 is the 3-dB antenna beamwidth, λ is the wavelength, r_0 is the volume range and l is the loss factor. In practice, for the short-wavelength ($\lambda < 10cm$) radars, reflectivity is computed from

$$Z = \frac{4\lambda^4}{\pi^4 |K_w|^2} \int |f(D)|^2 N(D) dD \tag{2.3}$$

where D is the diameter of a hydrometeor, $f(D)$ is the backscattering amplitude at the horizontal polarization (calculated from Mie scattering model (Skolnik 2002)), K_ω is the dielectric factor of water, and λ is the radar wavelength. $N(D)$, which is from mixing ratio of rain, snow, hail, specifies the drop size distribution (Cheong et al. 2008).

The SNR for distributed scatterers can be obtained by dividing Eq. 2.2 by kTB_n, which is the radar receiver noise power. This makes reflectivity propositional to SNR. In this work, the intensity of both hard and distributed targets will be characterized by SNR unless otherwise noted.

2.2.3.2 Example Systems

For distributed-target radars, we focus on meteorological radars. The distinguishing factor between meteorological radar and other kinds of aviation or military radars is the nature of distributed-targets, the resulting characteristics of the radar signal, and the means by which these weather echoes are processed to suppress artifacts and generate only the significant and essential weather information (Skolnik 2008).

The application of phased array radar (PAR) to weather observations has led to innovative concepts in both sensing schemes and system architectures. The Radar Innovations Lab (RIL) at University of Oklahoma has been working with NOAA-NSSL on developing a low-cost, reconfigurable, small scale testbed for dualpolarized phased array antenna prototype (Zhang et al. 2011), which is referred to as the Conformal Phased Array Demonstrator (CPAD). CPAD is a laboratory testbed for the future MPAR antenna array system. The T/R module used for CPAD is a MMIC-based dual-polarized design (Fig. 2.2(a)). The power amplifiers used for the T/R module consist of dual Class-E GaN HPAs with high PAE (Power-Added Efficiency). Each individual TR module and radiating element can be configured in different ways to study the impact of array manifolds on the radiation pattern performance. Fig. 2.2(b) shows the CPAD in the anechoic chamber under evaluation for antenna pattern.

Nowadays, many meteorological radars have migrated to replace the conventional tube-based transmitters with solid-state HPAs. One of the examples is PX1000 (Polarimetric X-band 1000) radar, which is designed by ARRC (Advanced Radar Research Center) at the University of Oklahoma. PX-1000 is a transportable, solid-state and polarimetric (independent H/V channels) radar providing novel waveform diversity for improving polarimetric quality (Cheong et al. 2012). PX1000 can transmit up to 200-Watt total peak power using two solid-state power amplifiers (SSPA).

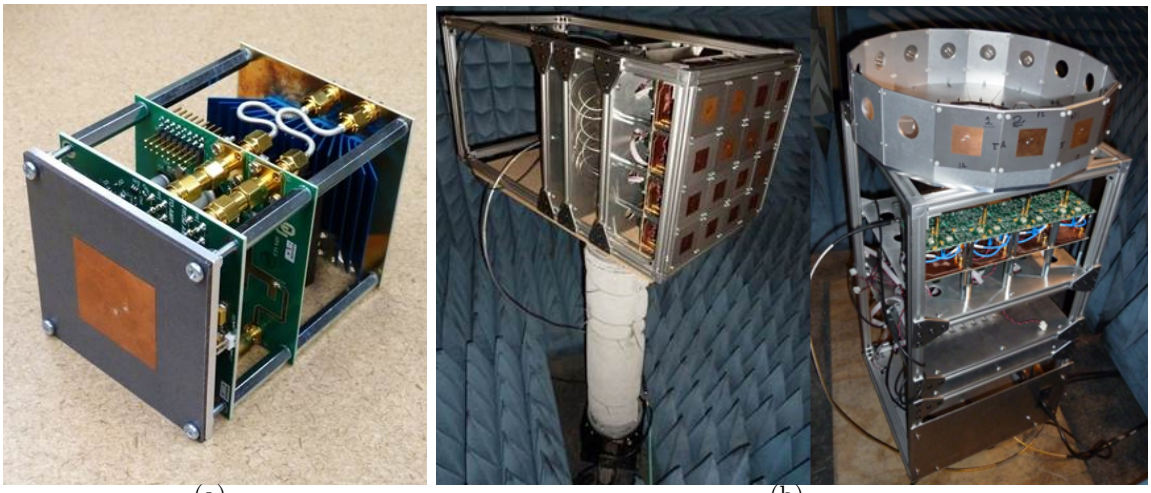

(a) (b)

Figure 2.2: The prototype of CPAD. (a) T/R module assembly (b) CPAD under evaluation.

Its operation frequency is 9550 MHz (X-band). The details about this radar will be discussed in Chapter 4.

2.3 Pulse Compression and Parameter Estimation

A pulse compression radar transmits a long pulse with pulse width T an peak power P. The pulse is processed by frequency or phase modulation to achieve a bandwidth B that is large compared to that of an unmodulated pulse with the same duration. Pulse compression originated with the purpose to amplify the signal power by temporal compression. It is a method that combines the energy of a long pulse with resolution of a short pulse. The use of pulse compression provides several advantages over unmodulated pulses: (1) The peak transmit power is reduced. The required transmit energy can be achieved by increasing the waveform pulse width without exceeding the peak transmit power constrain. Energy of long-duration, low-power pulse will be comparable to that of the short-duration, high-power pulse. The reason to reduce transmit power is that the high-power transmitters present problems such as high-voltage, low reliability, safety issue, size and weight, etc. The low pulse-power is

especially suitable for the SSPA transmitters. (2) The maximum range is expected according to the conventional radar equation - Eq. 2.1. (3) The compressed pulse can obtain a better range resolution compared to unmodulated one. The resolution is improved by a metric called pulse compression ratio, which is approximately the time-bandwidth (TB) produce of the waveform. The pulse compression ratio is usually much larger than unity. (4) The pulse compression radars are less vulnerable to interfering signals that differ from the modulated transmit signal. In addition, the coded waveform also has better jamming immunity (Skolnik 2008).

Conventional pulse compression techniques are facing challenges on modern radar systems, especially with solid-state transmitters. Limited power budget calls for long transmit pulses, which require a large compression ratio. In the mean time, traditional methods of pulse compression can only achieve sufficient sidelobe suppression with the compromised range resolution or target sensitivity. Advanced waveform design and pulse compression techniques have to be developed for excellent sidelobe mitigation capabilities without tradeoffs. In this work, new methods of waveform and pulse compression optimization will be discussed in Chapter 3∼5.

2.3.1 Matched Filter

The impulse response of a traditional matched filter is defined by the particular signal to which the filter is matched. Under the matching circumstance, the maximum signal-to-noise ratio (SNR) of the filter output is achieved as long as the receiver noise is Gaussian. The impulse response of the matched filter is defined as (Skolnik 2002)

$$h(t) = c \cdot s^*(t_0 - t) \tag{2.4}$$

where $s(t)$ is the transmit signal, c is a constant and t_0 is the time when the receiving signal is sampled.

The receiving signal at the l-th range gate can be expressed as (discretized version)

$$y(l) = \sum_i s(i)x^*(l-i) \tag{2.5}$$

where $x(i)$ is the impulse response of the i-th range gate.

Consider $\mathbf{x} = [x(1)\ x(2)\ \cdots\ x(L)]^T$ as a vector containing L samples of the range profile impulse response within the processing window. Then the summation term of Eq. (2.5) can be readily converted to an expression of matrix multiplication

$$Y = S \cdot \mathbf{x} \tag{2.6}$$

where $Y = [y(1)\ y(2)\ \cdots\ y(L+N-1)]^T$ and S is the waveform matrix defined as

$$S = \begin{bmatrix} s_0^* & 0 & \cdots & & \cdots & 0 \\ \vdots & s_0^* & & & & \vdots \\ s_{N-1}^* & \vdots & \ddots & & & \\ 0 & s_{N-1}^* & & \ddots & & \vdots \\ \vdots & 0 & \ddots & & \ddots & 0 \\ & & & \ddots & & s_0^* \\ \vdots & \vdots & & & \ddots & \vdots \\ 0 & 0 & \cdots & \cdots & 0 & s_{N-1}^* \end{bmatrix}$$

S is actually a Toeplitz matrix (Golub and Loan 1996) of $L+N-1 \times L$. N is the number of waveform samples.

Eq. (2.6) plays an important role in pulse compression theory from digital signal processing perspective. It makes possible to incorporate some key linear system and matrix theory into the pulse compression framework. The matrix expression is also a preferred style of expression for parallel computing. Adaptive pulse compression is one of the examples that can take advantage of parallel processing. This will be discussed in Chapter 4.

Traditionally, the range sidelobe is suppressed by applying a windowing weighting either on the waveform or after the matched filter. Fig. 2.3 shows the diagram of a typical radar system utilizing conventional pulse compression and window weighting.

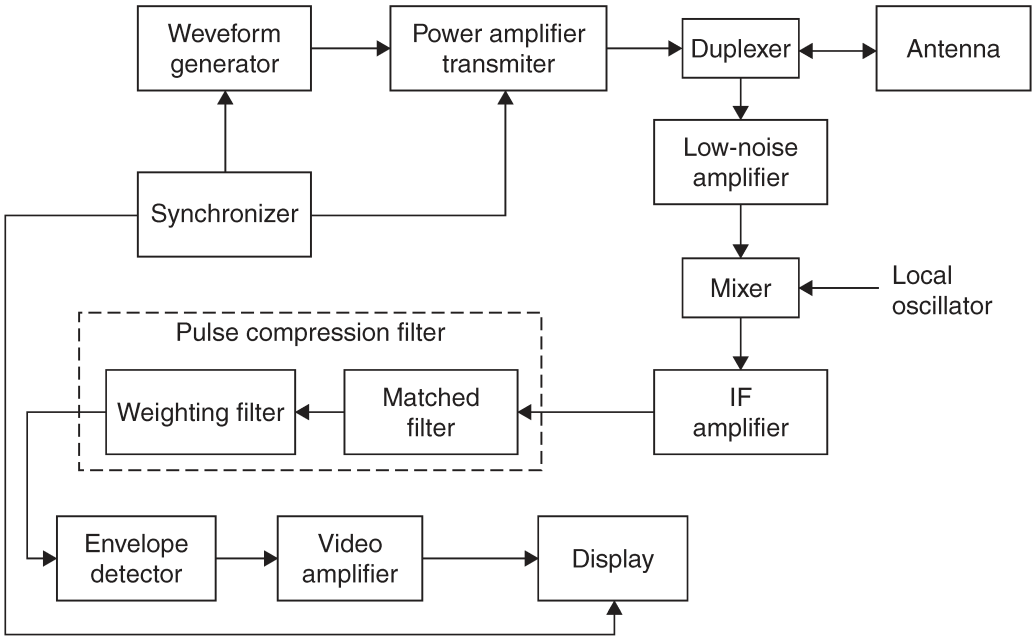

Figure 2.3: Diagram of a typical pulse compression radar

2.3.2 Least-Square (LS) Estimation Algorithm

LS estimate has been successfully applied to the optimization of pulse compression waveform and algorithms. For instance, (Baden and Cohen 1990) proposed a optimal mismatched filter for biphase coding waveform using iteratively reweighted least squares and (Blunt and Gerlach 2006) suggested an adaptive pulse compression algorithm based on reiterative minimum-mean-square errors.

The problem of the statistical least square estimate can be stated as follows (Lewis et al. 2006): Given an unknown variable x and the known observation y, find the best linear estimation for x, when x and y are related as

$$y = Hx + v \tag{2.7}$$

where H is a known matrix and v is the additive random noise corrupting the observation. The noise vector v has a zero-mean and positive definite covariance matrix R. In addition, v and x are uncorrelated. The residual cost function is defined as

$$c = \|y - Hx\|^2 \tag{2.8}$$

The derivation of least square estimate is by minimizing Eq. (2.8). The details can be found in literature such as (Lewis et al. 2006). The best estimate in the least square sense is concluded as:

$$\hat{x}_{LS} = (H^T R^{-1} H)^{-1} H^T R^{-1} y \tag{2.9}$$

Gauss-Markov Theory states that among the class of all linear estimates of the state variable x, $\hat{x}_{LS}$ is the best linear unbiased estimate (BLUE) (Lewis et al. 2006).

2.4 Previous Work On Waveform and Radar Transceiver Optimization

2.4.1 Conventional Methods for Improved Pulse Compression

One of the methods for improving pulse compression performance is waveform design, which is an important aspect of radar and communication theory. (Pillai et al. 2011) suggests the use of various waveforms (signals) in both transmitter (Tx) and receiver (Rx) designs for improving the overall performance such as mitigation of range sidelobe, and detection/identification of targets in interference and noise. Previous

examples on waveform design include phase coding, nonlinear frequency modulation, step-frequency modulation, etc.

Phase coding: (Frank 1963) first proposed an N-phase codes which have an autocorrelation function with one main peak and very small side peaks. (Lewis and Kretschmer 1981) suggests another new class of codes that are not subject to mainlobe to sidelobe ratio degradation caused by bandlimiting prior to sampling and digital pulse compression. They are referred to as P3 and P4 codes. To further improve the antocorrelation sidelobes and tolerance of low Doppler shifts, (Felhauer 1994) presented the P(n,k) codes which are derived by step approximation of the phase function of a nonlinear-frequency modulated. For biphase coding, Barker codes are well-known to have the best autocorrelation function. (MacWilliams and Sloane 1976) summarized the properities of the pseudo-noise (PN) binary sequences (a.k.a maximal-length shift-register sequences, or m-sequences). In order to apply PN codes to pulse compression for lower sidelobe level, (Ackroyd and Ghani 1973) suggested the use of least-square approximate inverse filtering techniques to radar range sidelobe reduction. (Baden and Cohen 1990) demonstrated the generation of mismatched filters to minimize the peak sidelobe of the biphase codes. In order to achieve the optimal peak sidelobe and integrated sidelobe level, it is important to choose a signal with favourable autocorrelation (Levanon 2005). The biggest issue for mismatched filters is the mismatch loss due to the use of cross-correlation instead of autocorrelation.

LFM and Weighting: One of the important technologies in the pulsed radar is the pulse compression by means of chirp signals. The chirped waveform obtained by linear frequency modulation of the pulse is used for transmission. At the reception, a correlation process with the transmission waveform is carried out to obtain a ideal impulse response. To suppress the range sidelobes, the frequency characteristics of the pulse compression filter may be weighted. The popular choices of weighting functions are *Hamming*, *Cosine-squared*, *Kaiser*, *Blackman*, etc. (Zhu et al. 2008) reported

the use of double Kaiser windows for sidelobe suppression and the Peak Sidelobe Level (PSL) can reach -75 dB. The well-known issue for weighing is the SNR loss and range resolution degradation. There exists a tradeoff between sidelobe level and range resolution.

Nonlinear frequency modulation: In airborne and satellite-borne applications, however, the sidelobes of the ground echo (both in range and azimuth/elevation) must be sufficiently low. (Griffiths and Vinagre 1994) described a technique for the design of a radar waveform with ultralow range sidelobes ($<$ -60 dB), by means of piecewise nonlinear FM (NLFM) waveform. Later, a continuous NLFM waveform design capable of achieving range sidelobe levels of better than -70 dB was introduced in (de Witte and Griffiths 2004).

Other methods of pulse compression include *step-frequency modulation* (Gill 1996), *CLEAN* algorithm (Deng 2004), *doppler-tolerant* waveform (Yang 2007), *neural network match filter* (Baojun et al. 2000), *compressive sensing* (Xu 2012), etc.

In the field of weather application, (Keeler and Hwang 1995) investigated several coded waveforms and compression filters for weather radar applications. Minimum integrated sidelobe (inverse) filters were demonstrated to be superior to matched filters for compression processing of distributed weather echoes. (Mudukutore et al. 1998) developed a simulation procedure to accurately describe the signal returns from distributed weather targets, with pulse compression waveform coding. It takes into account the effect of target reshuffling during the pulse propagation time. Pulse compression data from the CSU-CHILL radar were analyzed. (Alberts et al. 2008) evaluated pulse compression for use in phased array weather radar systems. The performance of the codes with regard to errors in estimating equivalent reflectivity, radial velocity, and spectral width is examined. In addition, the pulse compression scheme implemented on the Imaging Wind and Rain Airborne Proler (IWRAP) is described

in (McManus et al. 2008). IWRAP is a dual-band (C and Ku) Doppler scatterometer designed to map the atmospheric boundary layer wind fields, ocean surface wind fields, and precipitation within tropical cyclones (McManus et al. 2008). Recently, (Bharadwaj and Chandrasekar 2012) demonstrated the blind-range mitigation that is inherent in pulse compression by using a time-frequency multiplexed waveform while compression is performed in pure software architecture.

2.4.2 Radar Transceiver Optimization

Recall from Eq. 2.5 that the signal echo y is equal to the convolution between the transmitted signal s and the target impulse response h. Maximization of the receiver output SNR in white noise scenario leads to the matched filter. Since the output SNR depends on the transmitted signal s, further improvement in the output SNR can be obtained by exploiting the freedom present in selecting s at the transmitter. Thus, by combining the matched filter receiver with the transmit signal design problem, we are able to achieve a joint optimal transmitter-receiver design. This is equivalent to solving the following constrained optimization problem,

$$\text{maximize} \sum_{l=0}^{L} |y(l)|^2 \quad \text{subject to} \quad \sum_{l=0}^{N} |s(l)|^2 = C \tag{2.10}$$

where L is the number of range gate, and N is the number of waveform samples. t_0 is the moment when the receiver samples the echo signal. y is defined in Eq. 2.5.

More generally, the desired target is buried in both interference and noise. The transmit signal excites the target and interference simultaneously. The interference is often signal-dependent, which requires comprehensive transmit and receive designs. The goal of the receiver design is to enhance the target returns and simultaneously

suppress both the interference and noise signals. Thus, the signal power to average interference pulse noise ratio (SINR) at the receiver output can be used as an optimization goal. (Pillai et al. 2011) derived the maximum obtainable SINR

$$\mathrm{SINR}_{max} = \frac{1}{2\pi}\int_{-\infty}^{+\infty}\frac{|H(\omega)|^2|S(\omega)|^2}{H_c(\omega)|S(\omega)|^2 + H_n(\omega)}d\omega \tag{2.11}$$

where $H(\omega)$ is the Fourier transform of $h(l)$. $S(\omega)$ is the Fourier transform of $s(l)$. $H_c(\omega)$ and $H_n(\omega)$ are the power spectrum of interference and noise, respectively. The corresponding optimal receiver impulse response is defined as

$$W_{opt}(\omega) = \frac{H^*(\omega)S^*(\omega)}{H_c(\omega)|S(\omega)|^2 + H_n(\omega)}e^{-j\omega t_0} \tag{2.12}$$

in which $(^*)$ denotes the complex conjugate operation. Thus, the optimal transmit signal can be obtained by maximizing Eq. 2.11 subject to the energy constraint (the transmit signal pulse has finite energy)

$$\frac{1}{T}\sum_{l=0}^{N}|s(l)|^2 = \frac{1}{2\pi}\int_{-\infty}^{+\infty}|S(\omega)|^2 d\omega = E \tag{2.13}$$

where T is the sampling interval and E is the energy constrain. (Pillai et al. 2011) proved the *minimum phase* condition of the optimum solution of joint optimization and summarized the various aspects of waveform diversity designs. In Chapter 5, we will discuss a novel solution of joint transmit and receive optimization for mitigation of nonlinear distortion together with adaptive pulse compressions.

Chapter 3

Multi-Functional Radar Waveforms Design and Application

3.1 Introduction of Multifunctional Radar Waveform

Radar technology is advancing towards higher resolution, better precision and more versatile functions. In spaceborne application for example, NASA first demonstrated the combination of radar and communication functionality in Tracking and Data Relay Satellite System (TDRSS) (Cager et al. 1978). Recently, as with the advance of solid-state electronic and optoelectronic devices, the principles of carrier-free radar and radio communications have been implemented into practical systems (Taylor (1995); Di Benedett (2006)). (Surender and Narayanan 2006) suggested a combination of UWB waveform and OFDM technology to achieve a dynamic, ad-hoc, and covert communication network. This hybrid system also has the advantage of Low-Probability of Interception (LPI), which benefits from the noise-like spectrum behavior of UWB waveform. Fig. 3.1 depicts the simplified waveform generation portion of such system.

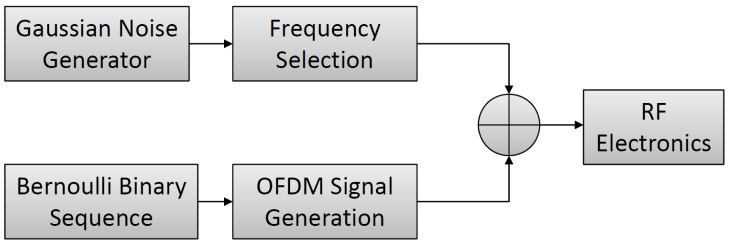

Figure 3.1: UWB OFDM waveform generator

Another field getting a lot of attentions recently is the aviation safety, where collision avoidance is one of the most critical issues involving detection, localization and alerting of external traffic. External traffic can be cooperative (with transponder response) or non-cooperative. It is believed that the combination of primary and secondary surveillance radar on a single aircraft platform is a promising solution to this situation, i.e., the radar receivers can use the reflected transponder signals from non-cooperative targets for detection and even tracking. If this is possible, both cooperative and non-cooperative targets can be detected using a single avionics. The concept and system aspects of using multi-functional ADS-B signal waveform for primary surveillance was first described in (Zhang et al. 2008), in which a binary phase modulation is introduced to convert the original 1090 MHz ADS-B signal waveform into a radar signal, and a "burst" of the reflected pulses from targets can be compressed to enhance the signal-to-noise ratio (SNR). Fig. 3.2 shows the diagram of ADS-B system. In this chapter, the basic concept of radar ambiguity function and sidelobe constrain will be reviewed, followed by the introduction of basic waveforms. Those are the building blocks of the multi-functional waveforms. Then the PPM/PM waveform characterization, optimization and its application are studied in details.

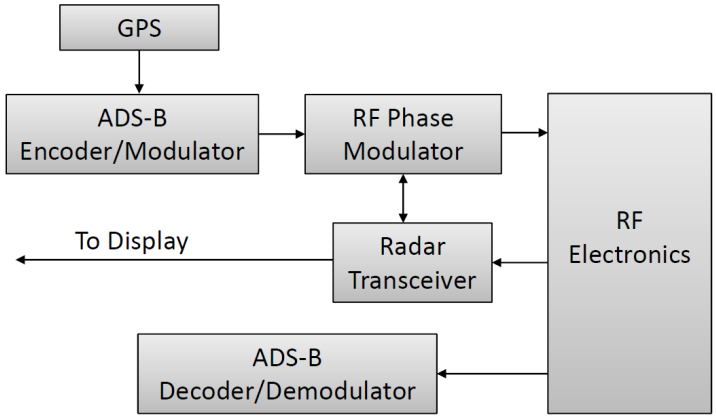

Figure 3.2: Concept of a multi-functional Sense and Avoid (SAA) system (Zhang et al. 2008)

3.2 Radar Ambiguity Function

Before we proceed with discussion of any type of radar waveforms, it is necessary to reiterate the concept of radar ambiguity function. The ambiguity function (AF) is defined as the time response of a filter matched to a given finite energy signal when the signal is received with a delay τ and a Doppler shift of ξ relative to the nominal values (zeros) expected by the filter (Levanon and Mozeson 2004). It describes how the receiver system can discern targets with different distance and velocity. The AF is defined as

$$\chi(\tau, \xi) = \int_{-\infty}^{\infty} u(t) u^*(t+\tau) e^{j2\pi\xi t} dt \tag{3.1}$$

The definition Eq. (3.1) can be extended to the cross ambiguity function by simply replacing the second u term with a new waveform w, where w is another set of waveform instead of the original waveform.

To simplify the calculation, AF can be obtained by applying the Fourier Transform on the waveforms first and then calculating the multiplication of Fourier Transforms

instead of convolution in the time domain. It is demonstrated by the following equations:

$$\chi(\tau,\xi) = \int_{-\infty}^{\infty} u(t) w^*(t+\tau) e^{j2\pi\xi t} dt \tag{3.2}$$

$$= \int_{-\infty}^{\infty} \left[u(t)e^{j2\pi\xi t}\right] w^*\left[\tau-(-t)\right] dt \tag{3.3}$$

$$= \left[u(t)e^{j2\pi\xi t}\right] \otimes \left[w^*(-t)\right] \tag{3.4}$$

$$= \mathscr{F}^{-1}\left[U(\xi-f)\cdot W^*(\xi)\right] \tag{3.5}$$

where $U(\xi)$ and $W(\xi)$ are the Fourier Transforms of $u(t)$ and $w(t)$, respectively.

3.3 Phased-Modulated Waveform

3.3.1 Linear Frequency-Modulated Waveform

Linear frequency modulation (LFM) waveform is the first and most popular pulse compression method. It achieves a large Time-Bandwidth (TB) product by a nonlinear phase modulation. The advantage of LFM is that it can tolerant large Doppler shift of the return signal. This tolerance significantly reduces the complexity of the signal processing system. The disadvantage of the LFM is also obvious: the output response has a time delay propositional to Doppler shift. Another drawback of LFM is the high sidelobe response of the matched filter. This can be overcome by applying windowing on the waveform, but with the trade off of spacious resolution (Skolnik 2002).

The complex LFM waveform with a rectangular pulse shape can be expressed as

$$s(t) = u(t)e^{j2\pi f_0 t} = \frac{1}{\sqrt{T}} rect(\frac{1}{T}) e^{j2\pi(f_0 t + Kt^2/2)} \tag{3.6}$$

where

$$u(t) = \frac{1}{\sqrt{T}} rect(\frac{1}{T}) e^{j\pi K t^2}, K = \frac{B}{T}$$

T is the pulse width and B is the LFM bandwidth. The spectrum of LFM is expressed as (Levanon and Mozeson 2004)

$$U(f) = \frac{1}{2KT} e^{-j\pi f^2/K} \left[\{C(U_1) + C(U_2)\} + j \{S(U_1) + S(U_2)\} \right] \tag{3.7}$$

where

$$C(x) = \int_0^x \cos(t^2)dt, S(x) = \int_0^x \sin(t^2)dt, U_1 = \sqrt{2K}(\frac{T}{2} - \frac{f}{K}), U_2 = \sqrt{2K}(\frac{T}{2} + \frac{f}{K})$$

As the TB product becomes large, the spectral amplitude of LFM is approximately a rectangle while the phase converges to $-\pi f^2/4 + \pi/4$. According to Eq. (3.1), the LFM AF is calculated as

$$|\chi(\tau, \xi)|^2 = \left| \frac{\sin \pi(\xi - K\tau)(T - |\tau|)}{\pi(\xi - K\tau)(T - |\tau|)} (1 - \frac{|\tau|}{T}) \right|^2, |\tau| \leq T \tag{3.8}$$

Fig. 3.3 shows the ambiguity function of a LFM waveform with $B = 4MHz$ and $T = 2\mu s$

3.3.2 Nonlinear Frequency Modulation Waveform

The autocorrelation function of the unweighted LFM waveform suffers from relatively high sidelobe level (approximately -13.2dB). Applying a certain weighting window function on LFM can significantly reduce the sidelobes, but the mismatch introduced by windowing can cause serious SNR loss. Shaping the transmitting waveform could also results in nonuniform amplitude of the pulse, which requires linear power amplifiers. Backing off from the saturated power is not efficient. The windowing method is actually trying to control the waveform spectrum. Another way of shaping the waveform spectrum is by weighting on the phase instead of the amplitude of LFM. This approach is termed Nonlinear Frequency Modulation (NLFM). The design details of NLFM can be found in literature such as (Johnston and Fairhead (1986); Collins and Atkins (1999)).

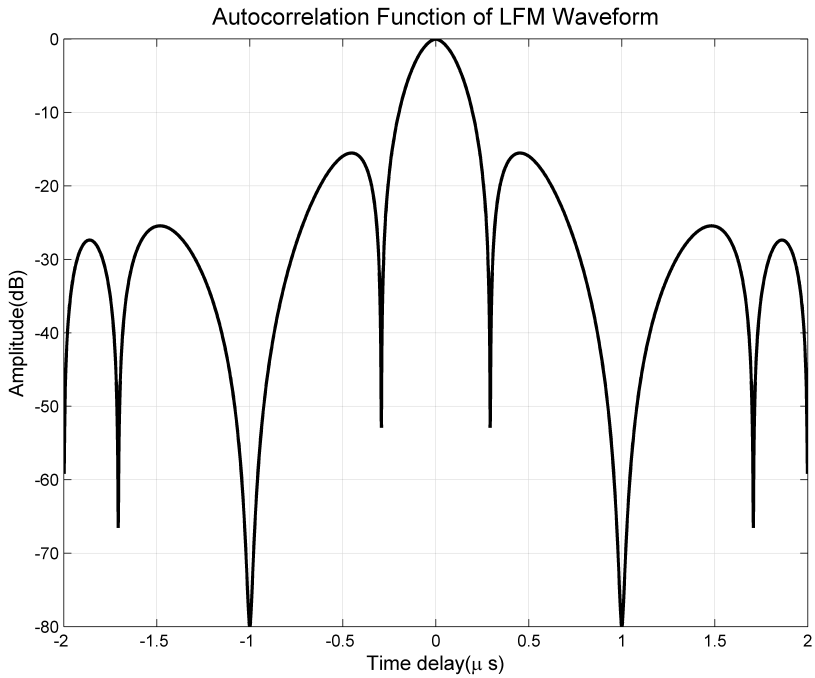

(a)

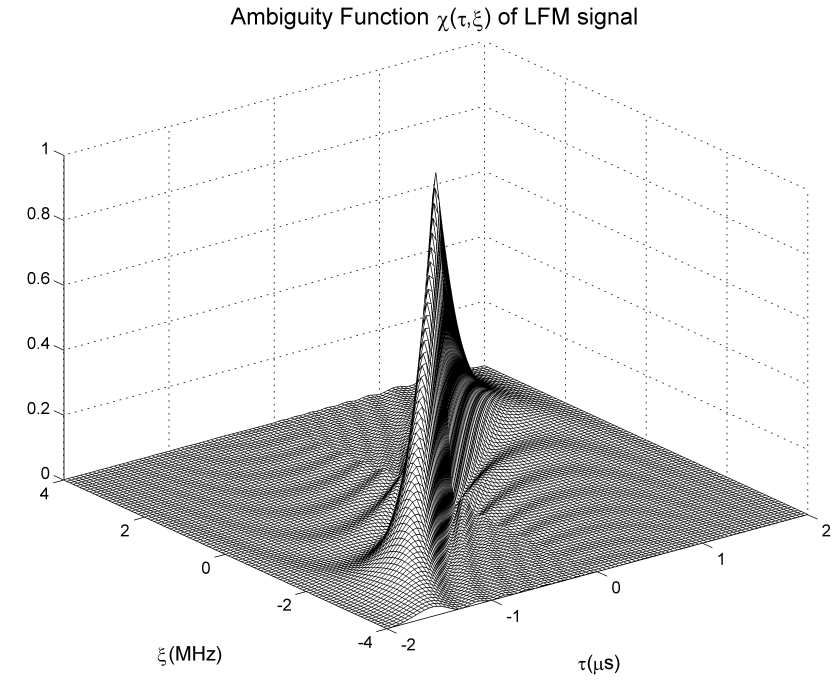

(b)

Figure 3.3: The autocorrelation function and ambiguity function of a LFM waveform with $B = 4MHz$ and $T = 2\mu s$.(a) LFM autocorrelation function; (b) Ambiguity function

3.4 Phased-Coded Waveform

One of the early methods for pulse compression is phased-coding (PC). Its phase modulation function has finite states. This is different from LFM waveform whose phase modulation is continuous. Most of these waveform utilize pseudo-random (PN) coding. The complex form of PN waveform is defined as

$$u\left(t\right)=\frac{1}{\sqrt{N}}\sum_{n=0}^{N-1}c_n\cdot p\left(t-nT\right) \tag{3.9}$$

where

$$p(t)=\begin{cases}\frac{1}{\sqrt{T}}, & 0<t<T\\ 0, & \text{otherwise.}\end{cases} \tag{3.10}$$

c_n is the PN sequence. $p(t)$ is the subpulse function. T is the pulse repetition time (PRT). N is the code length.

The power spectrum density (PSD) of the phase code is defined as

$$U(f)=\sqrt{\frac{T}{N}}\frac{\sin(\pi fT)}{\pi fT}e^{-j\pi fT}\left[\sum_{k=0}^{N-1}c_k e^{-j2\pi fkT}\right] \tag{3.11}$$

The spectrum of the phase code is primarily determined by the spectrum of the pulse itself.

3.4.1 Barker Code

Barker sequence is a special type of binary pseudo-random code. The binary pseudo-random code is a pulse compression code whose periodic auto-correlation function satisfies

$$\chi(m,0)=\sum_{k=0}^{N-1}c_k c_{k+m}=\begin{cases}N, & m=0(\text{mod }N)\\ a<N, & m\neq 0(\text{mod }N)\end{cases} \tag{3.12}$$

Barker code has a more strict aperiodic auto correlation function as follows

$$\chi(m,0)=\sum_{k=0}^{N-1-|m|}c_k c_{k+m}=\begin{cases}N, & m=0(\text{mod }N)\\ 0\text{ or }\pm 1, & m\neq 0(\text{mod }N)\end{cases} \tag{3.13}$$

Obviously, $|\chi(m,0)| \leq 1, m \neq 0$. Therefore, Barker sequence is also called the "best" finite binary sequence. There are only 7 Barker codes available. The longest has 13 bits. The 13-bit Barker code will be used in the Chapter 4 and 5.

3.4.2 M-Sequence

Another commonly-used code is m-sequence (MacWilliams and Sloane 1976). It is also known as *maximal-length shift register sequence*. Its periodic auto-correlation function is also very ideal and its ambiguity function has a thumbtack shape. m-sequence is generated by a linear feedback shift register (LFSR), which is the heart of many digital systems that rely on pseudorandom sequence. To construct an m-sequence of length $N = 2^m - 1$, one needs a primitive polynomial $g(x)$ of degree m. For instance, the following expression corresponds to a polynomial degree of 7,

$$g(x) = x^7 + x + 1 \tag{3.14}$$

Eq. (3.14) specifies a LFSR as shown in Fig. 3.4. Theoretically, the side lobe level of m-sequence's aperiodic auto-correlation function is approximately $\sqrt{N}$.

This type of waveform will be designed and optimized for radar sensing application later in this chapter.

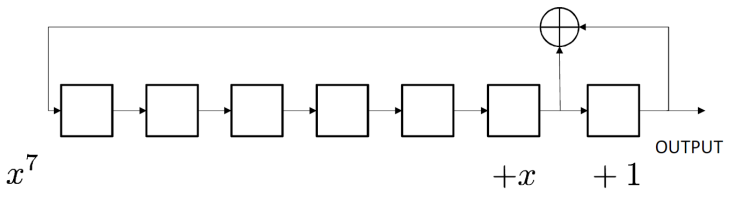

Figure 3.4: Feedback shift register corresponding to $x^7 + x + 1$

3.4.3 Polyphase Code

Barker code and m-sequence are both binary codes. Efforts have been done to search for polyphase codes with good sidelobe ratio and Doppler tolerance. Of the many polyphase codes, Frank code (Frank 1963) is most frequently used. Based on Frank code, a new class of symmetric radar pulse compression codes was introduced in (Lewis and Kretschmer 1981). They are P3 and P4 codes.

P3 Code: Define the signal bandwidth B and pulse width T. Then the phase of successive code samples is defined as

$$\Phi_k^{(3)} = \frac{\pi(k-1)^2}{BT} \tag{3.15}$$

P4 Code is defined as (Phase):

$$\Phi_k^{(4)} = \frac{\pi(k-1)^2}{BT} - \pi(k-1) \tag{3.16}$$

Table. 3.1 shows the phase for P3 and P4 code samples with $BT = 16$.

k	1	2	3	4	5	6	7	8
$\Phi_k^{(3)}$	0	$\pi/16$	$4\pi/16$	$9\pi/16$	π	$25\pi/16$	$4\pi/16$	$17\pi/16$
$\Phi_k^{(4)}$	0	$17\pi/16$	$4\pi/16$	$25\pi/16$	π	$9\pi/16$	$4\pi/16$	$\pi/16$
k	9	10	11	12	13	14	15	16
$\Phi_k^{(3)}$	0	$17\pi/16$	$4\pi/16$	$25\pi/16$	π	$9\pi/16$	$4\pi/16$	$\pi/16$
$\Phi_k^{(4)}$	0	$\pi/16$	$4\pi/16$	$9\pi/16$	π	$25\pi/16$	$4\pi/16$	$17\pi/16$

Table 3.1: Phase for P3 and P4 codes (modulo 2π), with $BT = 16$. $\Phi_k^{(3)}$ and $\Phi_k^{(4)}$ are the phase for P3 and P4 codes, respectively. It is noticed that the largest adjacent phase difference is in the middle of P3 code but on the two ends of P4 code.

3.5 Waveform Optimization For Low Sidelobe

In multi-target environment, the sidelobe of a strong target or clutter tends to overlap with the weak targets. Certain sidelobe suppression techniques must be adopted to prevent target from fading and increase the capability of detection for pulse compression systems. It is often desired to control the range-time sidelobe characteristic of waveforms. For point targets, the sidelobe and pulse compression performance can be characterized by the following definitions:

$$PSL = 10\log_{10}\frac{\text{Max sidelobe power}}{\text{main lobe power}} \tag{3.17}$$

$$ISL = 10\log_{10}\frac{\text{Total sidelobe power}}{\text{main lobe power}} \tag{3.18}$$

$$SNR_L = 10\log_{10}\frac{\text{SNR of weighting network}}{\text{SNR of matched filter}} \tag{3.19}$$

PSL, ISL and SNR_L refer to as *peak sidelobe level*, *integrated sidelobe level* and *SNR loss* respectively. The most commonly-used sidelobe rejection approach is by applying weighting function in the transmitter or receiver end (Skolnik 2002). Another notable method is mismatched filter (Ackroyd and Ghani 1973). The pulse compression receiver uses an optimized correlation filter to achieve the best sidelobe performance.

3.5.1 Weighting Method

LFM is the primary waveform for weighting method. From previous section we know that the sidelobe characteristic for LFM is approximately a sinc function. The maximum sidelobe level is -13.2 dB and the rest of sidelobes decays at a rate of $1/x$. As a spaceborne radar of NASA Tropical Rainfall Measuring Mission (TRMM), the Second-Generation Precipitation Radar (PR-2) adopts a LFM signal with $B =$

4 MHz and $T = 50\ \mu s$ (Fischman et al. 2005). After applying Kaiser window, the near surface sidelobes can be suppressed to -55 dB. Table. 3.2 compares the performance of different window functions applied to the LFM signal.

Window functions	Sidelobe (dB)	Mainlobe width (μs)	SNR_L (dB)	Sidelobe decay (dB/octave)
Rectangle	-13	0.22	0	6
Hanning	-31	0.36	1.49	18
Hamming	-42	0.33	1.34	6
Blackman	-58	0.42	1.89	18
Kaiser(β=6)	-58	0.35	1.66	12

Table 3.2: Pulse compression performance comparison for different window functions ($B = 4\ MHz, T = 50\ \mu s$)

3.5.2 Mismatched Filter

The idea of mismatched filter was first proposed and applied to polyphase code pulse compression (Baden and Cohen 1990), in which the ISL optimized filter is calculated initially, then the PSL optimized filter can be derived iteratively.

The polyphase code is defined as $\{s_i\}$ with a length of N and the mismatched filter is h of length $P \geq N$. h will minimize the PSL of the cross correlation between s and h. The details about optimal mismatched filter theory will be discussed within the following section.

3.6 Pulse Position and Phase Modulation Waveform Design and Application

In this section, we will discuss the design, optimization and application of a waveform with both phase modulation (PM) and pulse position modulation (PPM). The general concept of ADS-B radar system using this waveform is described in (Zhang et al. 2008). As mentioned before, the purpose of such waveform is to support detecting and tracking noncooperative collision threat in the airspace, while maintaining compatibility with the standard ADS-B transponders. This requires that the matched filter output have a low sidelobe level to recover the targets masked by the coupling signal of the transmitted waveform. The original transponder signal PPM waveform does not possess a stable sidelobe structure. The PM coding technique is applied to PPM waveforms to improve the auto-correlation and side-lobe performance.

3.6.1 Waveform Characterization

3.6.1.1 Waveform Description

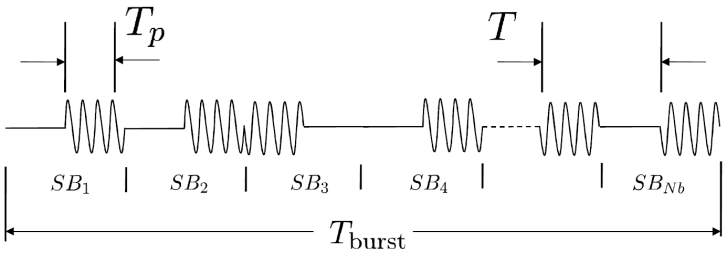

Figure 3.5: The structure of phase-modulated transponder waveform

Fig. 3.5 shows a simplified model for phase-modulated transponder signals. The pulses are transmitted in bursts, i.e., N_b Pulse-Position-Modulation (PPM) symbols are transmitted during T_{burst} time period. For binary PPM used in most transponders,

each PPM symbol contains a pulse having pulse width T_p , which is placed at either the first or the second half of the symbol period T. Moreover, each pulse is phase-modulated. The simplest binary phase modulation (PM) results in either 180° or −180° phase of each pulse in the burst, which correspond to either '0' or '1' in the binary phase codes. The 1090 ADS-B standard is the focus of this work. For this particular transponder standard, the parameter values in the signal model are $N_b = 112$ (ignoring the header pulses), $T_{burst} = 112\ \mu s$, $T_p = 0.5\ \mu s$ and $T = 1\ \mu s$. The pulse-burst is transmitted once per second. The carrier frequency of pulses is 1090 MHz. On the other hand, the discussions in this work can be easily generalized to other parameter sets or other transponder waveform standards.

There are two reasons PM is important to convert the transponder waveform to radar signals. First, since the PPM is used to carry the aircraft location information, it is not under the waveform designers control, the phase modulation improves the correlation performance and sidelobe structures, thus enabling the possibility of waveform optimization. Second, the PM code allows the discrimination of reflected transponder signals from the received transponder signals broadcast from other aircrafts. Even though random PM creates a spectrum spreading effect, it can be shown that the detection and demodulation specifications of the ADS-B signals can still be met. Therefore, there is no significant difference between normal transponder signals and phase-modulated transponder signals to those aircraft with general Mode-S or ADS-B transceivers.

3.6.1.2 Statistical Signal Model

The statistical model of the phase-modulated transponder signal is used to study the power spectrum density (PSD) of the waveform over a sufficiently long observation time. This is the key to facilitate the compliance and interference analysis. In general,

a phased-coded, PPM modulated long signal $u(t)$ observed over a long time can be modeled as

$$u\left(t\right)=\sum_{n=-\infty}^{\infty}a_{n}p\left(t-nT-\varepsilon_{n}\right) \tag{3.20}$$

which is a pulse train consisting of an infinite number of received pulse bursts, where T is the pulse repetition period. The single pulse $p\left(t\right)$ is defined as

$$p(t)=\begin{cases}\frac{1}{\sqrt{T_{p}}}, & 0<t<T_{p}\\ 0, & \text{otherwise.}\end{cases} \tag{3.21}$$

At baseband, both the PM symbols a_n and the PPM sequence ε_n are binominal-distributed random processes, and their probability distribution functions are given by

$$\Pr\left\{a_{n}\right\}=\begin{cases}p, & a_{n}=1\\ 1-p, & a_{n}=-1\end{cases} \tag{3.22}$$

and

$$\Pr\left\{\varepsilon_{n}\right\}=\begin{cases}q, & \varepsilon_{n}=0\\ 1-q, & \varepsilon_{n}=\varepsilon_{0}\end{cases} \tag{3.23}$$

ε_0 in Eq. (3.23) represents the pulse position in term of delay-time. For a particular case of transponders, $\varepsilon_0 = T/2$. Assuming a_n is a wide sense cyclostationary (WSCS) process with period N_b, following similar analysis procedures in (Win (1998); Durnea (2007)), it is seen that the PSD of $u\left(t\right)$ is the summation of both continuous and discrete components. The continuous portion of the spectrum is given by

$$S_{u}^{c}\left(f\right)=\frac{1}{T}\left|P\left(f\right)\right|^{2}\sum_{l=-\infty}^{\infty}\left[\frac{1}{N_{b}}\sum_{n=0}^{N_{b}-1}K_{a,\varepsilon}\left(n,l,f,f\right)\right]e^{-j2\pi flT} \tag{3.24}$$

where

$$\begin{aligned}K_{a,\varepsilon}\left(n,l,f,f\right)=&E\left\{a_{n}a_{n+l}^{*}\right\}E\left\{e^{-j2\pi f\varepsilon_{n}}e^{+j2\pi f\varepsilon_{m}}\right\}-\\ &E\left\{a_{n}\right\}E\left\{a_{n+l}^{*}\right\}E\left\{e^{-j2\pi f\varepsilon_{n}}\right\}E\left\{e^{+j2\pi f\varepsilon_{m}}\right\}\end{aligned} \tag{3.25}$$

$E\left\{.\right\}$ denotes statistical average. The discrete portion of the spectrum is given by

$$S_u^d(f) = \frac{1}{(N_b T)^2} \sum_{l=-\infty}^{\infty} \left| P\left(\frac{l}{N_b T}\right) \right|^2 \left| \sum_{n=0}^{N_b-1} E\{a_n\} E\left\{ e^{j\frac{2\pi\varepsilon_n l}{N_b T}} \right\} e^{j\frac{2\pi n l}{N_b}} \right|^2 \delta\left(f - \frac{l}{N_b T}\right) \tag{3.26}$$

where $\delta(\cdot)$ is the Dirac Delta function. It is evident that

$$E\left\{ e^{j2\pi f \varepsilon_n} \right\} = q + (1-q) \cdot e^{j2\pi f \varepsilon_0} \tag{3.27}$$

and

$$E\left\{ e^{j2\pi f \varepsilon_n} e^{-j2\pi f \varepsilon_m} \right\} = \begin{cases} 1, & m = n \\ 1 - 4q(1-q)\sin^2(\pi f \varepsilon_0), & m \neq n \end{cases} \tag{3.28}$$

If the sequence a_n is assumed to be wide sense stationary (WSS), the continuous spectrum in Eq. (3.24) can be simplified as

$$S_u^c(f) = \frac{1}{T} |P(f)|^2 K_0(f) + \sum_{\substack{l=-\infty \\ l \neq 0}}^{\infty} K(f) e^{-j2\pi f T l} \tag{3.29}$$

where

$$K_0(f) = 1 - (2p-1)^2 \left[1 - 4q(1-q)\sin^2(\pi f \varepsilon_0) \right]^2 \tag{3.30}$$

and

$$K(f) = (2p-1)^2 \left[q^2 - j2q(1-q)\sin 2\pi f \varepsilon_0 - (1-q)^2 e^{j4\pi f \varepsilon_0} \right] \tag{3.31}$$

In order to match this model with actual transponder waveforms, and obtain convergent summation of the exponential series in Eq. (3.29), we limit the range of the index from $-M$ to $+M$ (M is a sufficiently-large positive integer), which leads to

$$S_{u,M}^c(f) = \frac{1}{T} |P(f)|^2 K_0(f) + K(f) \cdot \frac{\sin(M\pi f T)}{\sin(\pi f T)} \cos\left[(M+1)\pi f T\right] \tag{3.32}$$

Similarly, the discrete spectrum portion in Eq. (3.26) can also be simplified with the WSS assumption. The result is given by

$$S_u^d(f) = \frac{1}{T^2} \sum_{l=-\infty}^{\infty} \left| P\left(\frac{l}{T}\right) \right|^2 |G(l)|^2 \delta\left(f - \frac{l}{T}\right) \tag{3.33}$$

where $G(l)$ is related to p and q through

$$G(l) = (2p-1)\left[q + (1-q)\, e^{j2\pi l}\right] \tag{3.34}$$

Given the pulse shape in Eq. (3.21) and the PPM/PM codes (with statistics p and q), and the length parameter M, the PSD of the pulse burst can be predicted by Eq. (3.24), (3.26), and (3.30)$\sim$ (3.34). The analytical predictions of this model are compared with the spectrum analysis results of actual PPM/PM pulse bursts. The actual PPM/PM bursts are recorded from the repeating output of an arbitrary waveform generator. One example is given in Fig. 3.6. It is seen that besides some noise effects, the analytic results match the actual signal spectrums shape, spectrum width, and spectrum peak locations. Especially, the locations of the discrete line spectrum are accurately predicted.

The impact of phase modulation on the PSD can be observed from Eq. (3.29) $\sim$ (3.34). When there is no phase modulation (i.e., $p = 1$), the PSD is dominated by the PPM sequence. If the entire PPM message is '0' or '1', that is equivalent to a simple periodic pulse-train, the continuous spectrum vanishes and the discrete spectrum remains. On the other hand, the phase modulation tends to reduce the level of the discrete spectrum. If the phase modulation has sufficient randomness ($p = 0.5$), the second part of the continuous spectrum and the discrete spectrum will disappear, and the PSD of the modulated transponder waveform is equivalent to the PSD of a single pulse in the burst.

The spectrum width of $u(t)$ is a parameter of interest because it is related to the evaluation of whether the phase-modulated transponder signals still be processed by standard ADS-B receivers (RTCA 2003) and whether it can be easily intercepted or jammed. It can be seen from Eq. (3.34) that the PM changes the overall power level, but not the structure of $S_u^d(f)$. Therefore, the spectrum width is determined by the continuous portion $S_u^c(f)$. As such, the spectrum width factor can be defined as

$$\sigma_u^2 = \int_{-\infty}^{\infty} \omega^2 S_u^c(\omega)\, d\omega - \left[\int_{-\infty}^{\infty} \omega S_u^c(\omega)\, d\omega\right]^2 \tag{3.35}$$

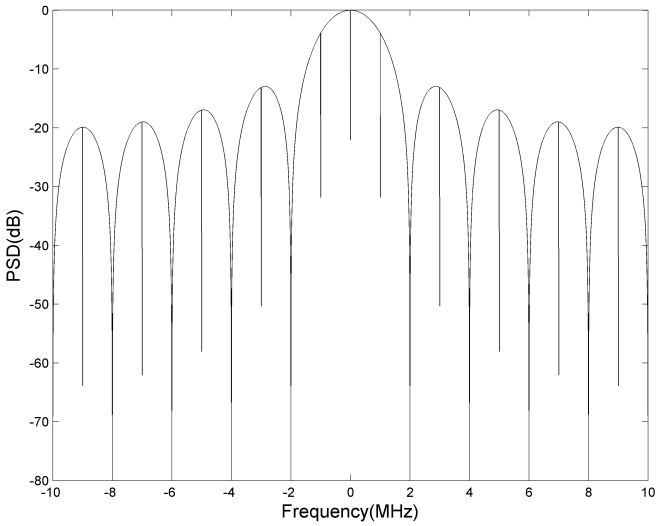

(a)

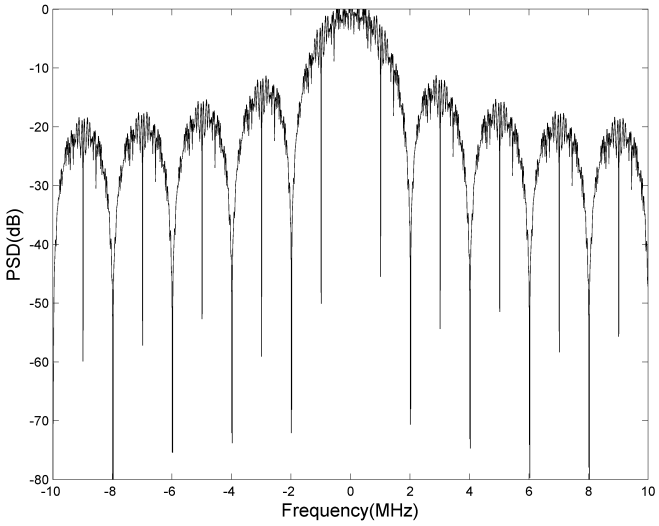

(b)

Figure 3.6: Example of theoretically predicted PSD compared with calculated PSD for repeating baseband PPM+PM pulse burst. The PPM and PM codes are both pseudo-random code with length N_b of 127. $T_p = 0.5$ s, $T = 1$ s, $p = 0.496$ and $q = 0.52$. (a) Analytical PSD from Eq. (3.24) and (3.26), and (b) PSD of a PPM/PM code calculated by periodogram.

where $\omega = 2\pi f$. For ADS-B standard pulse burst, Fig. 3.7 shows a numerically calculated 2D plot of σ_u^2 with p and q run from 0 to 1, respectively. Different combinations of PPM and PM codes can result in up to 9 dB variation in the spectrum width factor. It can be seen that if the PM code is random enough, e.g., p has values within the range of 0.3∼0.7, the effect of PPM on the spectrum is very small (less than 1 dB on σ_u^2). This observation indicates it is possible to control the correlation properties of the waveform independently through phase modulation. Large amounts of simulations with different PM codes also show the 3dB bandwidth of the phase-modulated PPM sequences still satisfies the roll-off requirement of the ADS-B standard.

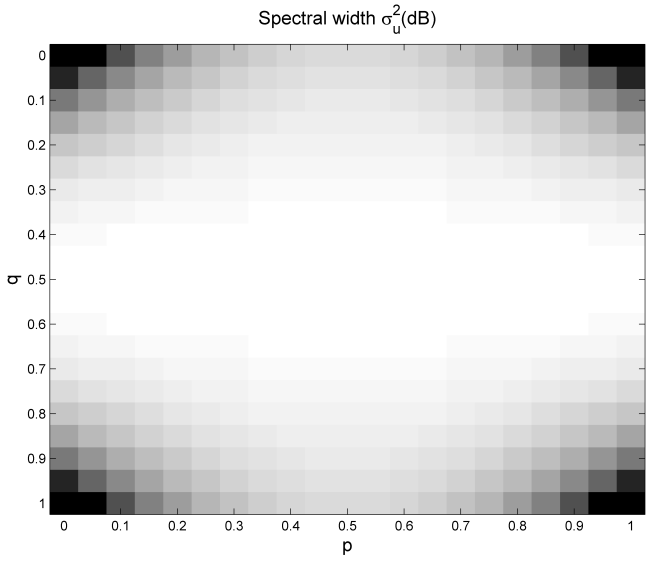

Figure 3.7: Calculated spectrum width factor versus different p and q

3.6.1.3 Deterministic Signal Model

The statistical signal model of the PPM/PM pulse burst is able to predict the ensemble-averaged behavior of the waveform when a large number of waveform realizations are stored and processed. In reality, however, the data available for real-time radar detection is generally a single-burst of pulses, which is just one realization of

the waveform and has limited time span. This case is especially important for waveform optimization, i.e., finding the best PM code sequence for target detection given a PPM sequence in the pulse burst. A deterministic signal model is used in such situations, which is given by

$$u_N(t) = \sum_{n=0}^{N_b-1} a_n p(t - nT - \varepsilon_n) \tag{3.36}$$

where N_b is the number of pulses in a pulse burst, a_n (taking values +1 and -1) and ε_n (taking values 0 and ε_0) are now deterministic sequences. The autocorrelation of $u_N(t)$ is

$$\begin{aligned} &R_u(\tau) = \int_{-\infty}^{\infty} u_N(t) u_N^*(t+\tau)\, dt \\ &= \sum_{n=0}^{N_b-1} \sum_{m=0}^{N_b-1} a_n a_m^* \int_{-\infty}^{\infty} p(t - nT - \varepsilon_n) p(t + \tau - mT - \varepsilon_m)\, dt \end{aligned} \tag{3.37}$$

The integral in respect to t in Eq. (3.37) only depends on the PPM sequence, and can be defined as

$$R_{PPM}(m, n, \tau) = \int_{-\infty}^{\infty} p(t - nT - \varepsilon_n)\, p(t + \tau - mT - \varepsilon_m) dt \tag{3.38}$$

and Eq. (3.37) is then reduced to

$$R_u(\tau) = \sum_{n=0}^{N_b-1} \sum_{m=0}^{N_b-1} a_n a_m^* R_{PPM}(m, n, \tau) \tag{3.39}$$

Eq. (3.39) is applicable to any pulse shape. For general transponder signals, $p(t)$ is considered as a square pulse, or in the more specific case of ADS-B, $T_p = T/2$. With such assumptions, in order to yield non-zero values in Eq. (3.38), the following condition needs to be satisfied:

$$|(m - n)T - \tau + (\varepsilon_m - \varepsilon_n)| \leq T_p \tag{3.40}$$

Eq. (3.40) indicates that when the PPM sequence as well as τ and n are given, not all the values of m will contribute to the autocorrelation. For general PPM modulated transponder burst, considering

$$|\varepsilon_m - \varepsilon_n| \leq \frac{T}{2} \tag{3.41}$$

there are only two possible values of m that can satisfy Eq. (3.41):

$$m = [n + \tau], m = [n + \tau] + 1 \tag{3.42}$$

where $[\cdot]$ denotes taking the closest integer value (rounded down). Next, for every index value n, we define $\Delta\varepsilon_{n,k}$ as the time-position difference between the n th and the $n + k$ th PPM pulse, i.e.,

$$\Delta\varepsilon_{n,k} = \varepsilon_{n+k} - \varepsilon_n \tag{3.43}$$

then the autocorrelation is further simplified as

$$R_u(\tau) = \sum_{n=0}^{N_b-1} a_n a_{n+[\tau]} R_p(n, \tau) + \sum_{n=0}^{N_b-1} a_n a_{n+[\tau+1]} R_p(n, \tau + 1) \tag{3.44}$$

and

$$R_p(n, \tau) = \int_{-\frac{T}{2}}^{\frac{T}{2}} p(t) p\left\{[\tau] T - \tau + \Delta\varepsilon_{n,[\tau]}\right\} dt, \tag{3.45}$$

$$R_p(n, \tau + 1) = \int_{-\frac{T}{2}}^{\frac{T}{2}} p(t) p\left\{[\tau + 1] T - \tau + \Delta\varepsilon_{n,[\tau+1]}\right\} dt \tag{3.46}$$

Eq. (3.44) through Eq. (3.46) separate the effects of PPM and PM in the deterministic autocorrelation function. For the special cases where $q = 1$ or $q = 0$ (all '0' or all '1' in the PPM message), Eq. (3.44) indicates that the autocorrelation at delay τ is nothing but the weighted-average of $R_{PM}([\tau])$ and $R_{PM}([\tau + 1])$, which are the autocorrelations of the elementary pulses at two consecutive time delays. The autocorrelation function Eq. (3.44) derived from the deterministic model is the basis of the time-domain waveform optimization in the following sections.

3.6.1.4 The Radar Ambiguity Function and Receivers

It is interesting to observe the characterizations of hybrid PPM/PM waveforms in presence of both time delay τ and Doppler shift ξ . Also, how the modulation coding schemes affect the radar waveform characterizations is also a critical issue. The radar ambiguity function (Skolnik (2002); Levanon (2005)) can be analyzed for such

purposes. The traditional definition of the ambiguity function assumes a correlation receiver, or matched filter, is used. For the phase-modulated transponder waveforms, however, two important aspects need to be emphasized: (1) the ambiguity function depends not only on the coding scheme, but also the relative change of PM codes within a sequence; (2) since the length of the transponder signal burst is short (112 pulses in one burst of ADS-B signal), the sidelobe structures of the autocorrelation result may not meet the detection requirements at certain SNR. A new category of receiver technique, called mismatched filtering (Baden and Cohen (1990); Ackroyd and Ghani (1973); Griep et al. (1995); Levanon (2005); Davis et al. (2007)), could be used if better sidelobe performance is desired. The cross ambiguity function should be used for this case. See Eq. 3.5.

To further elaborate on the ambiguity functions and take into account the combined impact of the PPM and PM on autocorrelation, the general ambiguity function can be expressed as the convolution of the pulse train and associated modulations (Titlebaum and DeClaris 1966), i.e.,

$$\chi(\tau,\xi) = \chi_1(\tau,\xi) \otimes_\tau \chi_2(\tau,\xi) \tag{3.47}$$

$$= \sum_{i=-(N_b-1)}^{N_b-1} \chi_1(\tau - iT,\xi)\chi_2(iT,\xi) \tag{3.48}$$

where $\chi_1(\tau,\xi)$ and $\chi_2(\tau,\xi)$ are the ambiguity functions of $p(t)$ and $v(t)$, respectively, and $\otimes_\tau$ denotes convolution with respect with τ .

The ambiguity function for the rectangular signal $p(t)$ can be easily calculated as:

$$\chi_1(\tau,\xi) = e^{j\pi\xi(T_p-\tau)} \frac{\sin \pi\xi(T_p - |\tau|)}{\pi\xi(T_p - |\tau|)} \left(1 - \frac{|\tau|}{T_p}\right), |\tau| < T_p. \tag{3.49}$$

The ambiguity function of $v(t)$ can be derived in a similar manner as in Eq. (3.37),

$$\chi_2(\tau,\xi) = \frac{1}{N_b}\sum_{k=0}^{N_b-1}\sum_{l=0}^{N_b-1}\int_{-\infty}^{+\infty} a_k a_l \cdot \delta(t-kT-\varepsilon_k)\cdot\delta(t+\tau-lT-\varepsilon_l)e^{j2\pi\xi t}dt \quad (3.50)$$

$$= \frac{1}{N_b}\sum_{k=0}^{N_b-1}\sum_{l=0}^{N_b-1}\int_{-\infty}^{+\infty} a_k a_l \cdot \delta(t)\cdot\delta[t+\tau-(l-k)T-(\varepsilon_l-\varepsilon_k)]e^{j2\pi\xi(t+kT+\varepsilon_k)}dt \quad (3.51)$$

$$= \frac{1}{N_b}\sum_{k=0}^{N_b-1}\sum_{l=0}^{N_b-1} a_k a_l e^{j2\pi\xi(kT+\varepsilon_k)}\delta[\tau-(l-k)T-(\varepsilon_l-\varepsilon_k)]e^{-j2\pi\xi[\tau-(l-k)T-(\varepsilon_l-\varepsilon_k)]}dt \quad (3.52)$$

It is obvious that $\Delta\varepsilon = \varepsilon_l - \varepsilon_k \in \left\{-\frac{T}{2}, 0, \frac{T}{2}\right\}$ and since the double summation is nonzero only for $\tau = (l-k)T + \Delta\varepsilon$, let $\tau = mT/2$, where m is an integer. We could further simplify $\chi_2(\tau,\xi)$ to yield single summation forms:

$$\chi_2\left(\frac{mT}{2},\xi\right) = \begin{cases} \frac{1}{N_b}\sum_{k=0}^{N_b-1} a_k a_{[\frac{m}{2}+k]}\cdot e^{j2\pi\xi(kT+\varepsilon_k)}, \Delta\varepsilon = 0, \text{m is even}, \\ \frac{1}{N_b}\sum_{k=0}^{N_b-1} a_k a_{[\frac{m\pm1}{2}+k]}\cdot e^{j2\pi\xi(kT+\varepsilon_k)}, |\Delta\varepsilon| = \frac{T}{2}, \text{m is odd}. \end{cases} \quad (3.53)$$

From Eq. (3.53), the ambiguity function of this combined PPM/PM signal heavily depends on the coding and receiving schemes. It is seen that the ambiguity function is symmetrical for $m < 0$ and $m > 0$. Also, we can conclude from Eq. (3.53) that as an impact of random PPM modulation, $\chi_2(\tau,\xi)$ has different expressions depending on $|\Delta\epsilon| = 0$ or $|\Delta\epsilon| = T/2$. This is because when the Doppler shift ξ is constant, the PPM modulation affects the correlation structure of the PM codes and introduces additional phase change like a filter.

To illustrate the radar ambiguity function for phase-modulated transponder waveforms, several ambiguity function plots computed for different PPM/PM coding schemes are shown in Fig. 3.8∼3.10. These figures are representative examples of large amounts of computation results from different code selections. It is noted that both PPM and PM codes can be random binary numbers (MacWilliams and Sloane 1976). Normally, they can be generated from either a Linear Recursive Sequence

(LRS) with random initial register states, or Maximum Length Binary (MLB) sequence (also called m-sequence) (MacWilliams and Sloane 1976) as a smaller code space. Simulated bursts of PPM/PM binary codes with ADS-B waveform parameters are used for the computations in Eq. (3.5). Since PM is of more concern, we only change the PM codes for Fig. 3.8∼Fig. 3.9 while the PPM codes are the same. In Fig. 3.8, a specific realization of the general pseudo-random code is used for PPM and an MLB code is used for PM. The detailed procedure of generating the mismatched filter coefficients for a particular waveform is given in the next section. An example of the calculated cross ambiguity function is depicted in Fig. 3.10.

It is well-known that an MLB sequence has excellent autocorrelation sidelobe performance. From the zero-delay cut of the ambiguity functions in Fig. 3.8 and Fig. 3.9, it is observed that using MLB in phase modulation also gives better delay-correlation performance for the hybrid PPM/PM waveform. The simulations also show that using the MLB code in phase modulation can also improve the sidelobes in the Doppler plane, thus reduce the velocity ambiguity. However, both the general LRS and MLB result in satisfactory Doppler response. This indicates that the range correlation performance has a higher priority in waveform optimizations. In Fig. 3.10, the lowest sidelobe level in the time-delay domain is achieved through mismatched filtering, although there is ignorable SNR loss. This owes to the excellent sidelobe suppression property of the mismatched filter. Compared to the range correlation performance, the Doppler response in Fig. 3.10 has relatively larger sidelobes and lower resolutions. This is due to the fact that these codes are optimized numerically for good autocorrelation sidelobes instead of joint range-Doppler performance. On the hand, it is seen from the zero-Doppler cuts that Doppler performance similar to the conventional pulsed Doppler radars can be achieved.

In summary, the ambiguity function of a PPM/PM hybrid signal is characterized by a thumbtack shape and is appropriate for radar application. In addition, large

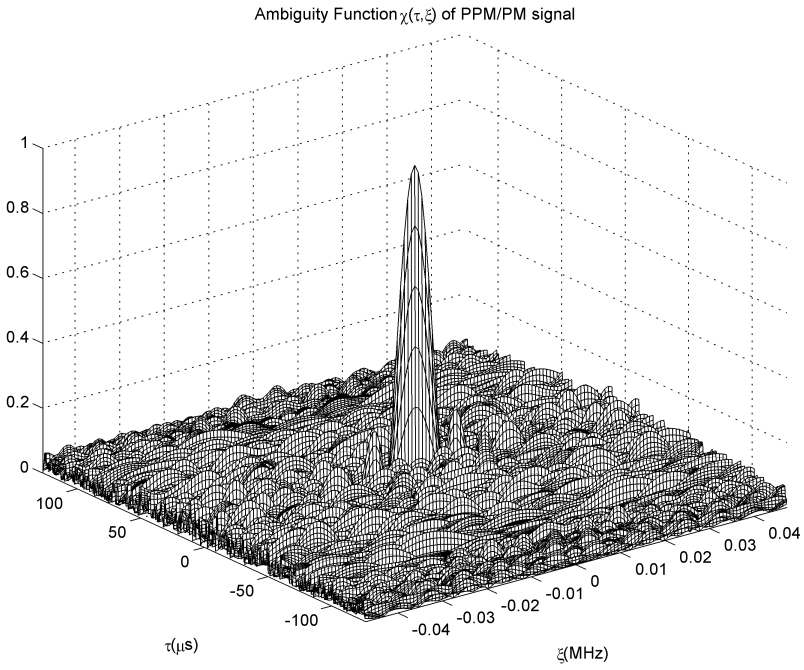

(a)

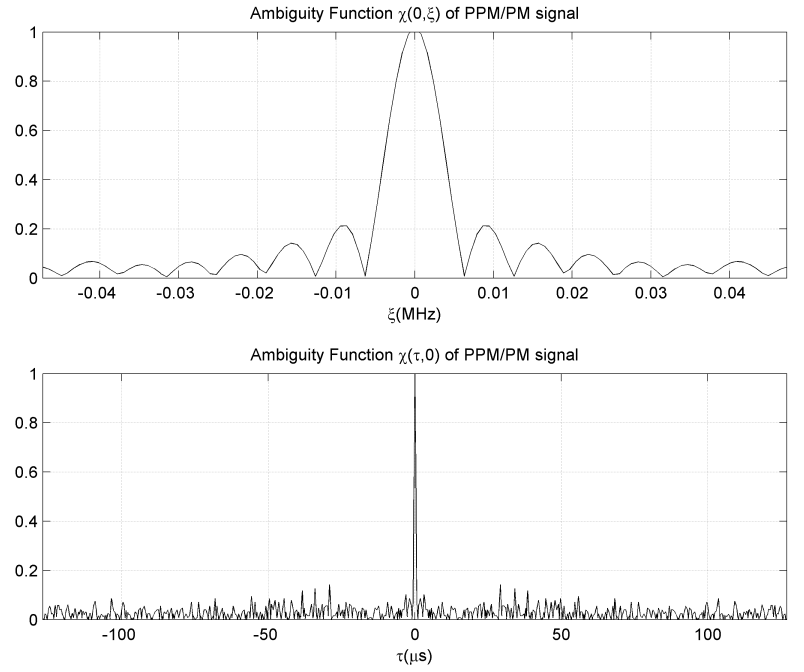

(b)

Figure 3.8: An Illustration of radar ambiguity function (a) Ambiguity function $\chi(\tau, \xi)$. (b) Zero-Doppler $\chi(\tau, 0)$ and zero-delay cut $\chi(0, \xi)$. The PPM code is generated by a normal LRS random code generator and the PM code is produced by MLB code generator.

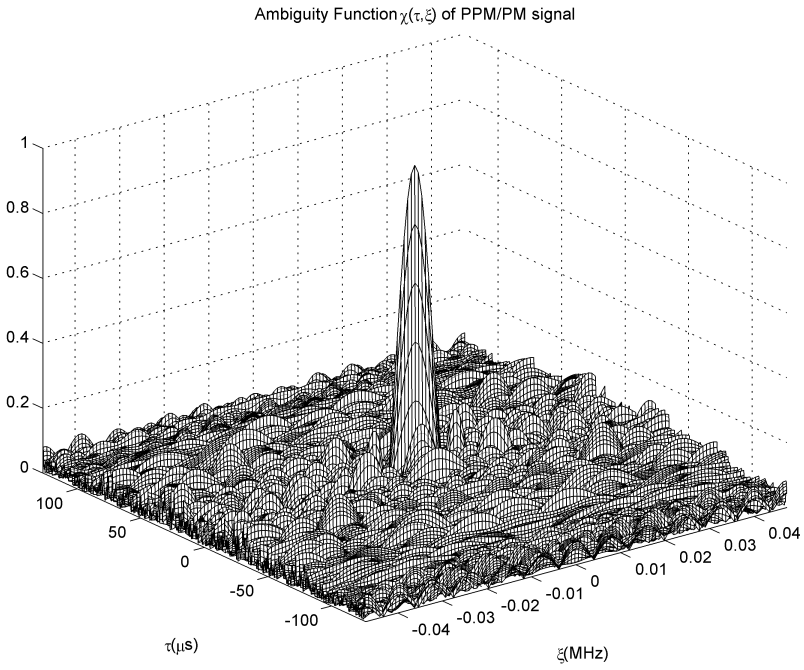

(a)

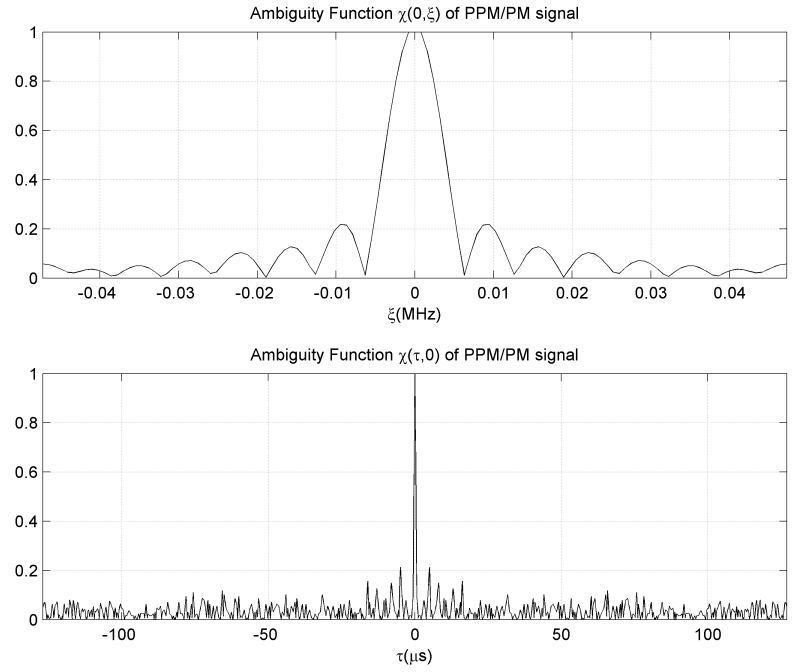

(b)

Figure 3.9: Same as Fig. 3.8 except that both the PPM and PM modulation codes are generated by a normal LRS random code generator.

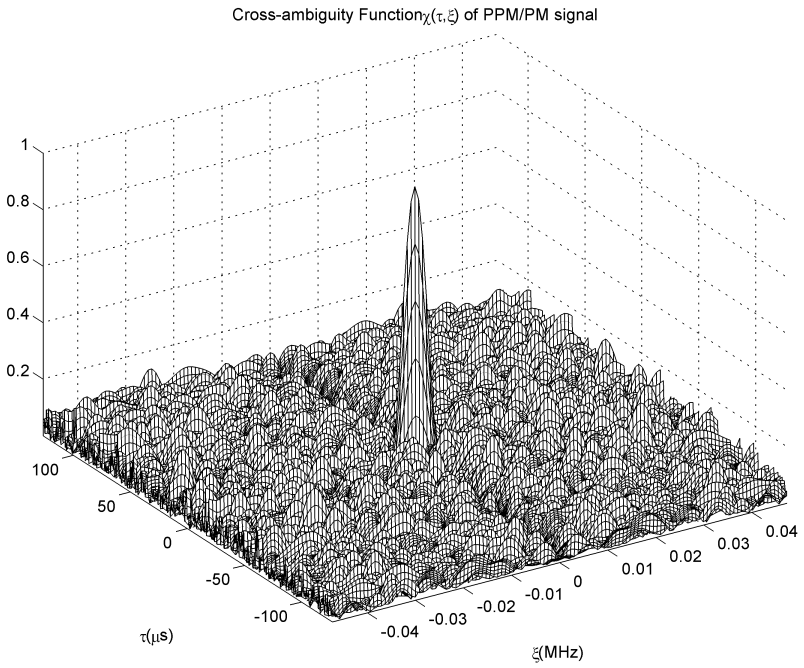

(a)

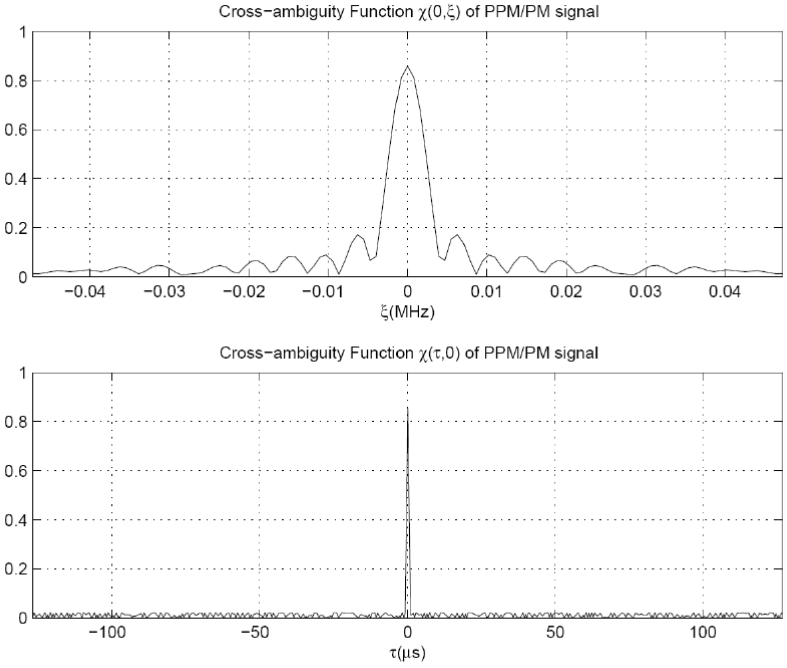

(b)

Figure 3.10: An Illustration of radar cross-ambiguity function based on the mismatch receiver: (a) Cross-ambiguity function $\chi(\tau, \xi)$ (b) Zero-Doppler $\chi(\tau, 0)$ and zero-delay cut $\chi(0, \xi)$. Both the PPM and PM modulation codes are generated by a normal LRS random code generator.

amounts of simulations show that once the PM code is fixed, choosing different PPM codes does not affect the overall shape of the ambiguity function. It is concluded from these observations that the phase modulations may play a dominate role in the waveform designing. This is a useful result since the PPM codes (ADS-B messages) cannot be controlled by waveform designers.

3.6.2 Waveform and Receiver Optimization

3.6.2.1 Criteria

For every PPM transponder message consisting of N symbols, there are 2^N possible binary sequences for phase coding (e.g., 2^{112} for ADS-B burst). Each PPM/PM combination displays unique correlation/ambiguity functions, which makes it not feasible to search all the possible codes for optimization. Also there is no algorithm developed to automatically compose the optimal PM codes given the PPM messages. Therefore, the current solution to such a challenge is to search in an organized manner, i.e. having specific criteria and construct the PM codes progressively in a minimized set to satisfy the criteria. Based on the discussions of Section 3.6.1, there are three conclusions that can help the optimization process: First, the PPM modulation is not under control, and does not have significant impact compared with to PM. The MLB sequence for PM is shown to have superior performance for ambiguity functions. Second, the range correlation performance has more variety than the Doppler plane performance with different PM codes. Third, the simplified, analytical solutions for correlation functions are available.

As a consequence, the priority of waveform optimization of a PPM/PM signal has been focused on the optimization of the range sidelobes based on different criteria. Since the PM code is seen to play a dominant role in correlation performance, it should be treated with higher priority. In addition to the general criteria for waveform optimizations (Golomb and Gong 2005), the following specific criteria are used

in this work: (a) Integrated Sidelobe Level (ISL) (for a scenario dominated by distributed clutter), and (b) Peak Sidelobe Level (PSL) (for a scenario requiring target detection in the presence of large discrete clutter). And if neither ISL nor PSL of the autocorrelation (matched filter) is satisfactory, mismatched filtering could be utilized to suppress the time sidelobe power. Also, the sidelobes of strong mutual coupling interference can be subtracted, similar to the "first order" implementation of the CLEAN algorithm in (Deng 2004). To further reduce the computation load, the ISL and PSL can be applied to a "localized" time-delay region, i.e. the area where the targets of interest may reside.

3.6.2.2 Optimization Algorithms

The procedure of PPM/PM code optimization is introduced in Fig. 3.11. Given the PPM message (generated by the transponder) and the area of interest (as a range of delay $[\tau_a, \tau_b]$), the optimization procedure first searches possible MLB sequences to satisfy the ISL and PSL requirements, based on $R_u(\tau)$ calculations from Eq. (3.44). If none of the possible MLB sequences satisfies the ISL/PSL requirements, this step ends with a PPM/PM combination with achievable minimum-sidelobe autocorrelation. The PPM and PM-MLB codes are merged together to form an Extended Code Sequence (ECS) to be optimized, and the mismatched filtering procedure is then invoked. Filter coefficients h_{ISL} are calculated in the first iteration. If the sidelobes of the *cross-correlation* between ECS and h_{ISL} are not satisfactory, further iterations to improve the mismatched filtering coefficients (h_{PSL}) need to be computed. The procedure finally results in an optimized MLB sequence for PM modulation and the corresponding receiver coefficients for sidelobe control. Several details of this procedure are elaborated as follows:

a. ISL/PSL optimization for matched filtering For this specific ADS-B application, the pulse compression ratio is 112. The code length is first designed

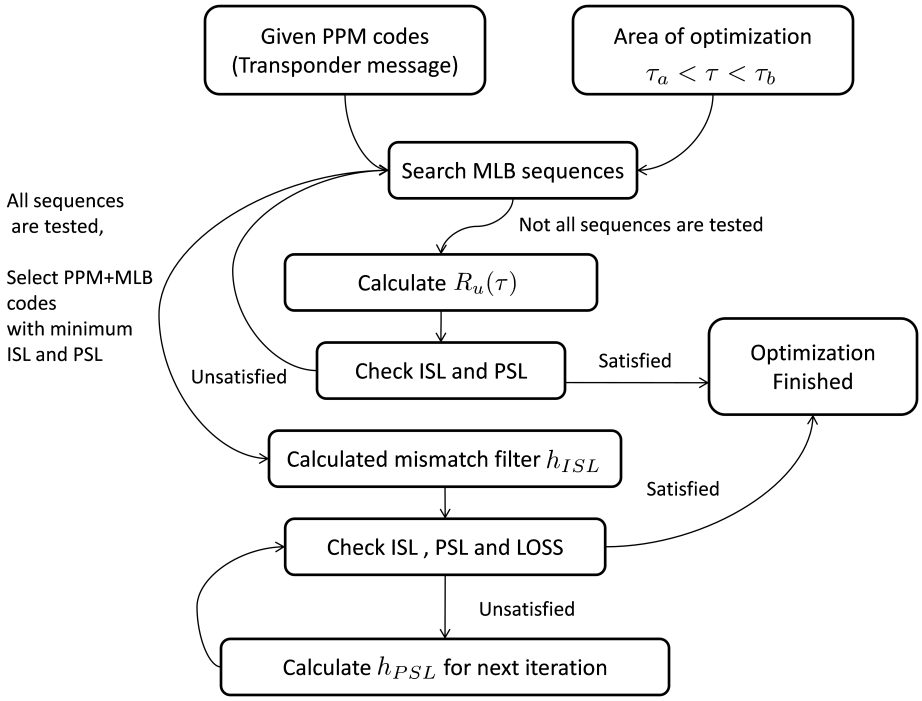

Figure 3.11: The flowchart of PM code optimization process used in transponder-based radar systems

No.	$x^7+x^6+x^5+x^4+x^3+x^2+x+1$							
1	1	0	0	0	0	0	1	1
2	1	0	0	0	1	0	0	1
3	1	0	0	0	1	1	1	1
4	1	0	0	1	0	0	0	1
5	1	0	0	1	1	1	0	1
6	1	0	1	0	0	1	1	1
7	1	0	1	0	1	0	1	1
8	1	0	1	1	1	0	0	1
9	1	0	1	1	1	1	1	1
10	1	1	0	0	0	0	0	1
11	1	1	0	0	1	0	1	1
12	1	1	0	1	0	0	1	1
13	1	1	0	1	0	1	0	1
14	1	1	1	0	0	1	0	1
15	1	1	1	0	1	1	1	1
16	1	1	1	1	0	0	0	1
17	1	1	1	1	0	1	1	1
18	1	1	1	1	1	1	0	1

Table 3.3: All possible MLB generators for $n = 7$

to be 127 and then truncated to 112, which introduces a 1.3 dB loss of PSL. Again, we only focus on the MLB code, which is a commonly used low-sidelobe pseudorandom code generated by shift registers (or a generator polynomial $h(x)$). The length of the code is $N = 2^n - 1$. Fig. 3.4 has shown one example configuration of the phase registers for 127/112 bit sequence generation. In order to obtain an MLB sequence, the polynomial of the MLB generator must be irreducible and primitive (Tan and Godfrey 2001). According to this principle, all the possible structures of MLB generators are found and summarized in Table. 3.3. A search in this set of $127 \times 18 = 2286$ codes for the optimal ISL and PSL of the PPM/PM signal is performed. This search process is illustrated in Fig. 3.12, where the PSL and ISL of all possible MLB codes for 4 particular PPM codes are depicted.

It is seen from Fig. 3.12 that a -21 dB PSL sidelobe level is attainable for the four example PPM codes. The calculated ISL is around -3 dB, except for the all-one PPM scenario, because half of the autocorrelation results are actually zero, resulting in the loss of half of the ISL power. This rarely happens in real-life scenarios, since there is always some meaningful information contained in the PPM sequence.

b. Mismatched filtering for further sidelobe control The ISL optimization for the mismatch filtering is essentially a process to solve a least-square-error minimization problem (Baden and Cohen (1990); Griep et al. (1995)), and the solution has the following form:

$$h_{ISL} = \mathbf{B}^{-1} s \left(s^* \mathbf{B} s\right)^{-1} N \tag{3.54}$$

where

h_{ISL}: The optimal ISL mismatched filter coefficients;

s: The ECS (Extended Code Sequence), which consists of a series of -1, 0, 1

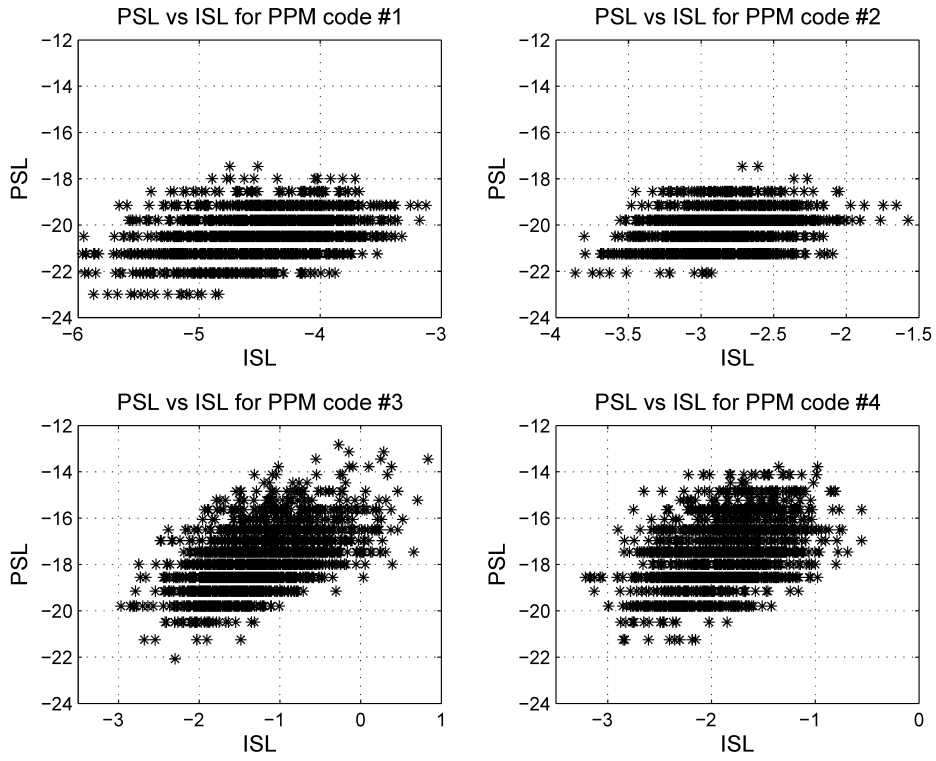

Figure 3.12: Illustration of PSL versus ISL (in dB) of 2286 possible PPM/PM codes for four different PPM message codes. PPM#1: 127 1s ($11111\cdots$); PPM#2: 127 alternative 0s and 1s ($010101010101\cdots$); PPM#3: pseudo-random code generated by MATLAB 'rand' command; PPM#4: 40 0s plus 47 1s plus 40 0s ($00000\cdots11111111\cdots000000$);

codes. They are combined PPM/PM baseband symbols, e.g., If PPM and PM codes are both 112 in length, then s is 224 in length.

$\mathbf{B} = \mathbf{XFX}^*$: Quadratic function of the original code s;

$\mathbf{X}$: Hankel matrix of the code s vector, or

$$X = \begin{bmatrix} 0 & \dots & 0 & s_0 & s_1 & \dots & s_{N-1} \\ \vdots & 0 & & & \dots & & 0 \\ 0 & s_0 & s_1 & \dots & s_{N-1} & 0 & \vdots \\ s_0 & s_1 & \dots & s_{N-1} & 0 & \dots & 0 \end{bmatrix} \tag{3.55}$$

$\mathbf{F}$: The weighting matrix used to place arbitrary weights on the sidelobes in the minimization problem;

Thus, $\mathbf{y} = \mathbf{sh}^*$ defines the cross-correlation between the original code and the filter. $E = \mathbf{yFy}^*$ defines the sidelobe energy, and the final optimal ISL solution actually minimizes the variable E. (Griep et al. 1995) suggests a set of steps of general PSL mismatched filter optimization, which iteratively solves the ISL optimization problems with updated $\mathbf{F}$ until the specific lower bound is reached. This method will be applied to the ADS-B-based phase coding optimization scheme.

3.6.2.3 Examples of Waveform Optimization

As an example, the PPM/PM code#3 from Fig. 3.12 was selected, and the corresponding ISL and PSL optimal filters are calculated. The result is shown in Fig. 3.13. The first plot of Fig. 3.13 is the autocorrelation of optimized PPM/PM code for PPM#3 in Fig. 3.12; the second one is the cross-correlation between the original PPM/PM code and the ISL mismatched filter; the third plot is the cross-correlation

between the PPM/PM code and the PSL mismatched filter. Along with the tremendous sidelobe suppression for mismatched filters (-35.18 dB for ISL, -42.34 dB for PSL), there is a *LOSS* of -3.557 dB and -3.35 dB for ISL and PSL filters, respectively.

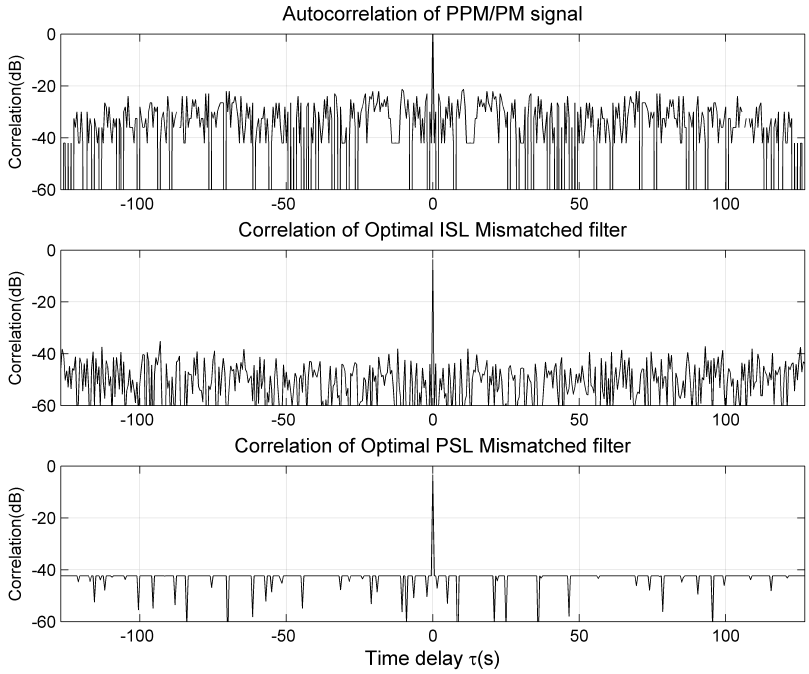

Figure 3.13: Time correlation of matched filter and mismatched filter

3.6.3 Prototype Radar Transceiver System

3.6.3.1 Transceiver Architecture

To further investigate the waveform design and detection performance, a prototype radar transceiver system is designed and fabricated. As is shown in Fig. 3.14, depending on the target range in the experiment, the PPM sequence is generated first, and the waveform optimization procedure is performed to generate the PM codes. The intermediate frequency (IF) PPM/PM waveform (modulated ADS-B waveform)

is generated at 70 MHz carrier, and then loaded into an arbitrary waveform generator (AWG). This signal is upconverted to 1090 MHz (Transponder band), then fed through a narrow band filter centered at 1090 MHz with 2% fractional bandwidth. The signal is amplified to 10 watt (+40 dBm) then transmitted to antenna. Both the 1090 MHz horn antenna and the omni-directional antennas (as are in transponders) are used in the experiments. At the receiver side, the signals from the receive antenna are first filtered at 1090 MHz center frequency, then down-converted and filtered before the I & Q data is extracted. The received IF signals are passed through 70 MHz low pass filters, amplified, and then sampled by a high-speed digital storage oscilloscope (DSO). It is emphasized here that for sidelobe and noise reduction, a data acquisition system with high bit-resolution (> 10 bit) is preferred. The acquired waveforms from the DSO are processed using either auto-correlation or mismatched filtering (cross-correlation) for target detection.

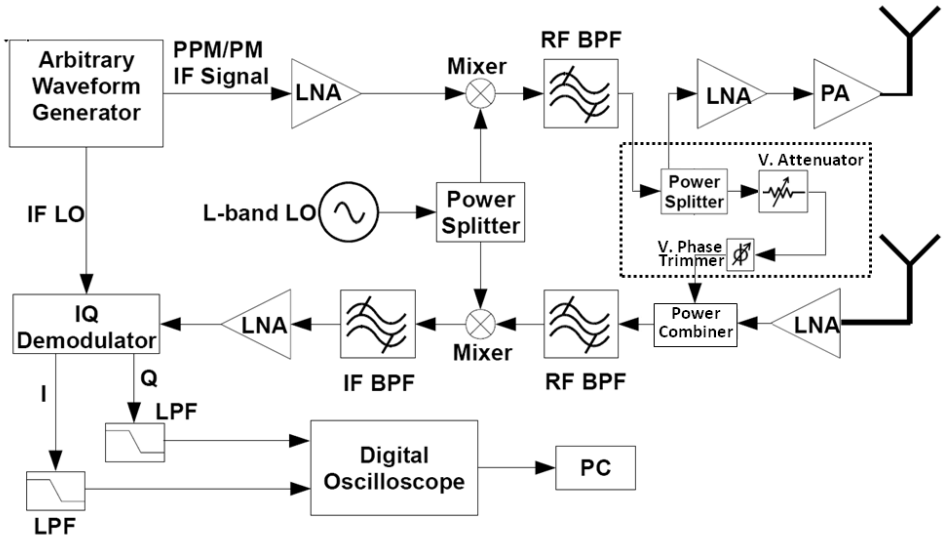

Figure 3.14: Simplified block-diagram of a transponder based PPM/PM radar system with interference cancellation circuitry.

3.6.3.2 Coupling Interference Control

The transponder-based radar faces various kinds of interference including multipath and direct antenna coupling. The generated signal is 112 μs in length, effectively making this a continuous wave system for target distances less than 33.6 km. The direct coupling from the transmitter can be a severe limiting factor of the receiver's dynamic range. The waveform optimization is able to minimize the sidelobes from direct coupling correlation, but these sidelobes may still be stronger than the target signal at particular ranges. As such, interference between transmit and receive due to coupling needs to be carefully managed.

Using directional, low sidelobe antenna is the most effective hardware solution to the direct coupling problem. Since an omni-directional TCAS (Traffic Collision Alerting System) antenna is used in the experiment, a ground plane can be inserted between the transmit and receive antennas to reduces coupling, and interference is further reduced by the introduction of additive cancellation at the front-end. For a given cable length and antenna spacing, the path due to direct coupling is predominantly a single path and fairly stable. This path is measured, and a secondary path is introduced using a 180° power splitter (shown in the dashed box, Fig. 3.14. The secondary path is tuned using a variable attenuator and phase trimmer until the coupled signal and secondary signal are lined up and 180° out of phase. A power combiner adds them together, resulting in destructive interference. Fig. 3.15 shows the output of the canceller for a single 0.5 μs pulse, as well as the entire 112 μs burst. Together with a directional transmit antenna, a larger than 50 dB total transmit-receive isolation can be achieved.

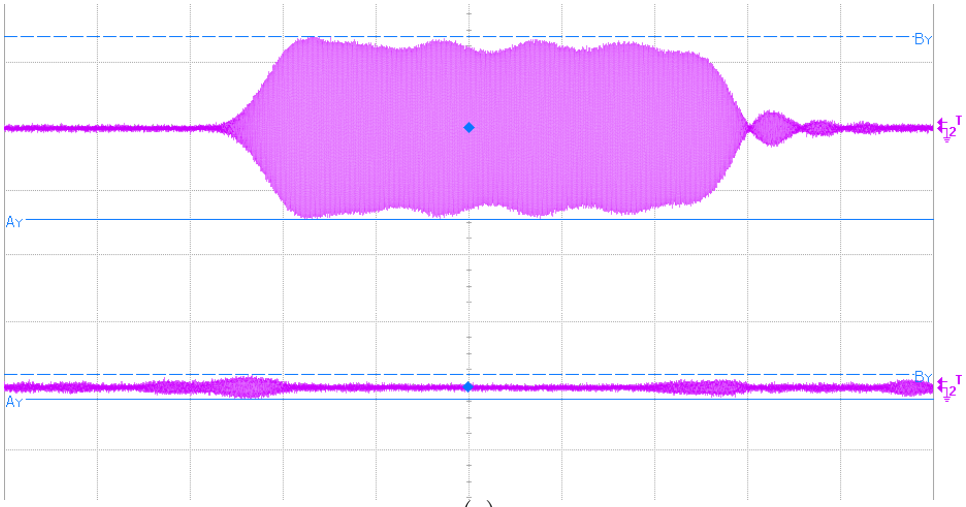

(a)

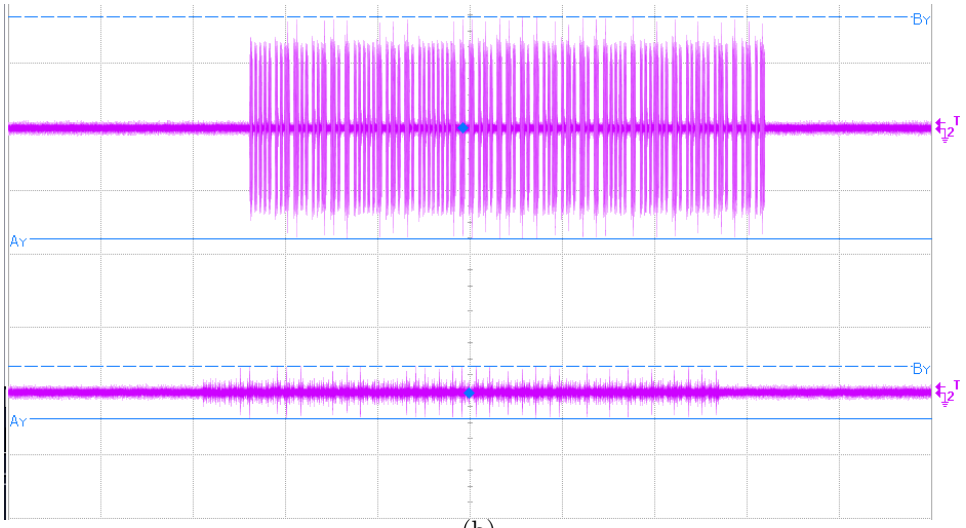

(b)

Figure 3.15: Effectiveness of active cancellation of direct coupling interference at front-end: (a) Measured interference, single pulse before (top) and after (bottom) additive cancellation. (b) Cancellation results of entire 112 μs burst for the emulated PPM/PM waveform.

3.6.4 Indoor and Field Experiments

3.6.4.1 In-door Hardware Emulation

A hardware emulation experiment is performed in an RF chamber using the transceiver system discussed in the previous section. The generated radar IF waveform is embedded with a simulated target signature (which is scaled according to the predicted return power and delayed transmit replica), and this combined waveform is transmitted to the empty range. Meanwhile, the waveform is coupled back from the transmitter to the receiver. As a result, the emulation accurately preserves the direct coupling interference and tests the receiver performance under various Signal-to-Interference (SIR) Ratios. Since the receive signal comes mostly from direct coupling with the transmit signal, the actual echo from the target would be hardly distinguishable in reality. In this particular case, the simulated signal power is 20 dB below the direct coupling interference. The received coupling signal is sampled and processed. Fig. 3.16 shows the example results of detecting such a simulated target at 4 μs. Both correlation reception and mismatched filters are utilized. Also, the receiver output when there is no target present is subtracted as "background". This can be considered as cancellation of the coupling interference in the digital domain. The cross-correlation receiver output, as shown in Fig. 3.16(a), results in a target peak about 10 dB higher than the nearest sidelobe. The mismatched filtering result shows significant improvement (almost 10 dB) on the target peak to sidelobe ratio. Note that an arbitrarily selected, un-optimized PM code can easily result in a sidelobe peak at the target location and overwhelm the true target signature.

3.6.4.2 Field Test With Stationary Targets

The first field experiment uses a water tower (considered to be a steel sphere with about 13-meter diameter) as the stationary target and the radar system was placed at two different observation locations with 300 m and 200 m range from the target,

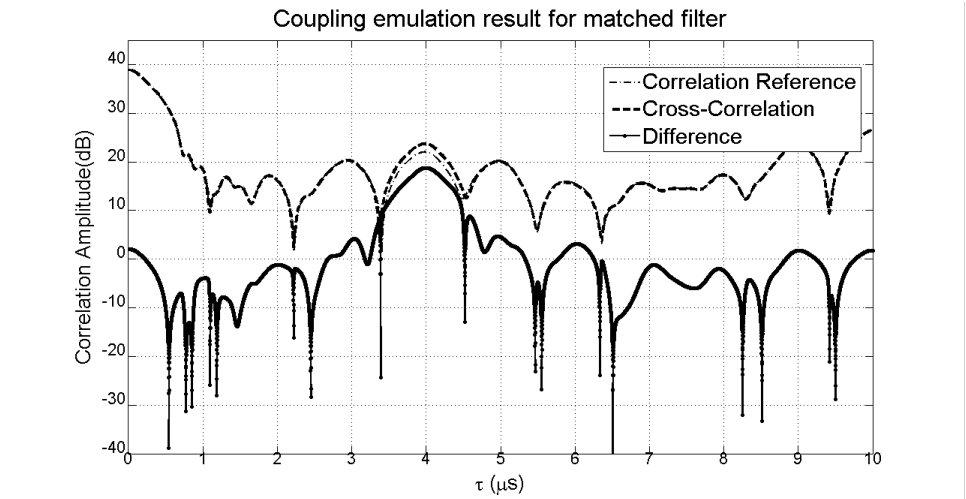

(a)

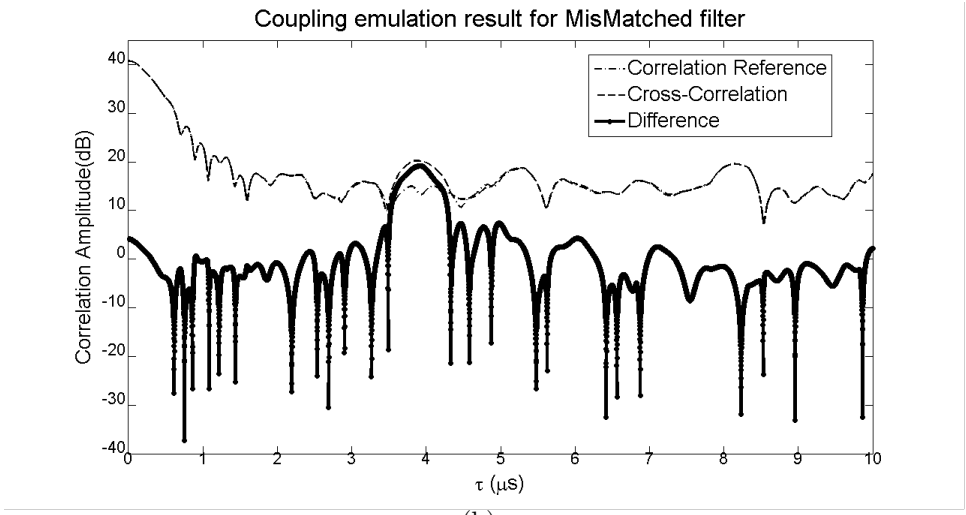

(b)

Figure 3.16: The in-door emulation experiment embeds a simulated target signature into the transmit waveform and receives through the direct coupling channel. The received signals contains direct coupling and processed to detect the simulated target. (a) Processing result using correlation receiver and digital cancellation, (b) Processing result using mismatched filtering and digital cancellation.

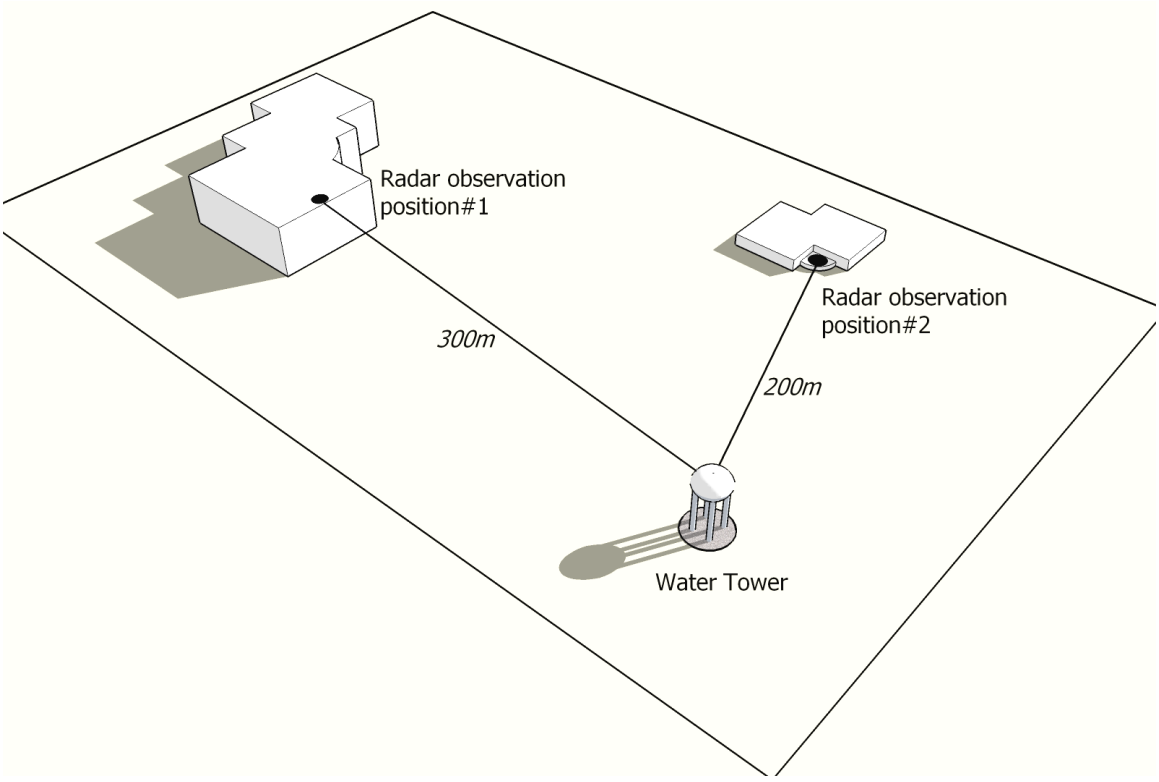

Figure 3.17: Field experiment setup schematic diagram.

respectively. Fig. 3.17 shows the geometry of the experimental setup. There is strong ground clutter present in this scenario, so it is seen that the target cannot be detected using un-optimized PPM/PM waveforms. Again, the digital cancellation technique is performed. The correlation output when the transmit antenna is aimed at clear sky is the background for the cancellation operation. The PPM/PM code in the modulated ADS-B waveform has been optimized by selecting MLB sequences satisfying the minimum ISL/PSL over the desired target range.

The measured range profiles based on these two optimized waveform and cross-correlation receivers are displayed in Fig. 3.18$\sim$ 3.19. It is seen that there are strong interference signatures around 0.6$\sim$1.0 μs, which are caused by ground clutter (the radar is set on the roof of Building#1 and on the balcony of Building#2). In Fig. 3.18, the peak at 2.0 μs is identified as the target echo with 300 m range. In Fig. 3.19, the peak appearing at 1.35 μs is the target echo with 200 m range. In both scenarios,

there are some sidelobes and targets further away, which are much lower than the expected target signal levels. The range profiles obtained from mismatched filtering do not display significant improvement in terms of the target peak to sidelobe ratios, due to the fact that the outdoor environment is much more complicated than the RF chamber, thus ground clutter and other interference at L band can alter the return signal structure optimized for specific filter coefficients. On the other hand, ground clutter will be a less severe factor for actual mid-air collision avoidance scenarios, and optimal mismatched filtering can be improved by incorporating the clutter and interference knowledge as long as they are available.

3.6.4.3 Field Test With Moving Airborne Target

A flight test using a small twin-engine, general aviation aircraft was performed on Oct 29, 2008 at the Max Westheimer research campus airport of the University of Oklahoma. The basic setup and geometry of this flight test is shown in Fig. 3.20. The aircraft approached the runway (a flight path shown in white arrows) at a fixed height of 100$\sim$200 feet and normal landing speed. And the radar observation position is located at about 300 feet away from the center of the runway. The PPM/PM waveform was optimized and generated from an arbitrary waveform generator, a directional horn antenna and high-power amplifier were used for transmit ($\sim$ 60 watts peak power), and signals from one channel of the TCAS antenna were recorded once per second. The received signals from the antennas are correlated with transmit templates, and each correlation result represents a "scan" of the interested ranges. Combination of these scanning data results in a two dimensional scan-range map as shown in Fig. 3.21.

Since the transmit antenna and the receive beam of the TCAS channel pointed in a fixed direction perpendicular to the runway, the target signature is expected to reach peak amplitude when the aircraft is within the transmit beam. This expectation is

well-validated by the scan-range map illustrated in Fig. 3.21, where the "zooming in" scan-range map around the expected target range (0.7 μs) are illustrated. Fig. 3.21(a) and (b) display the target signatures of two consecutive approach flights, respectively. The amplitude of the correlation signature first becomes stronger as the airplane enters the radar beams, and then diminishes as the target exits the radar beams. The strongest target signature appears at $6 \sim 8$ seconds, which corresponds to the time the target enters transmit illumination. It is seen from the flight test result that it is possible to use a basic correlation receiver (matched filter) to detect or even track a moving target, with PM-optimized transponder-type signals.

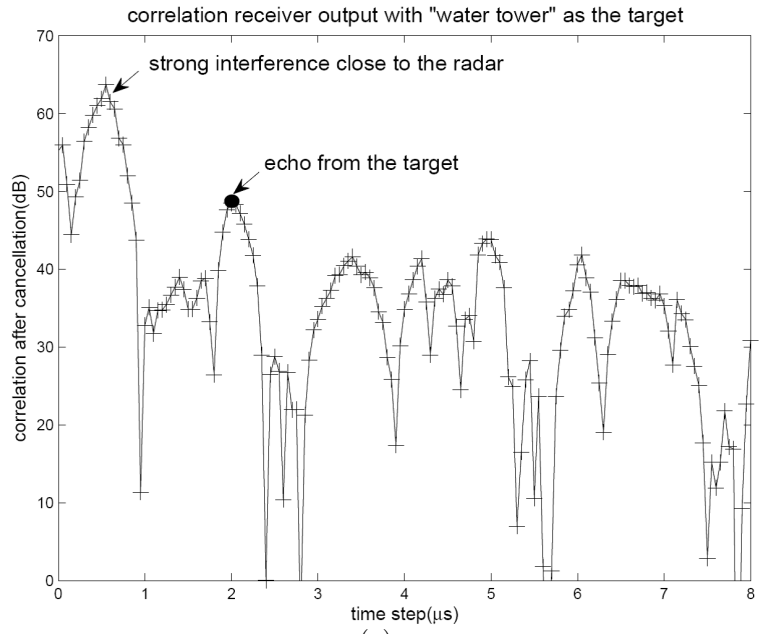

(a)

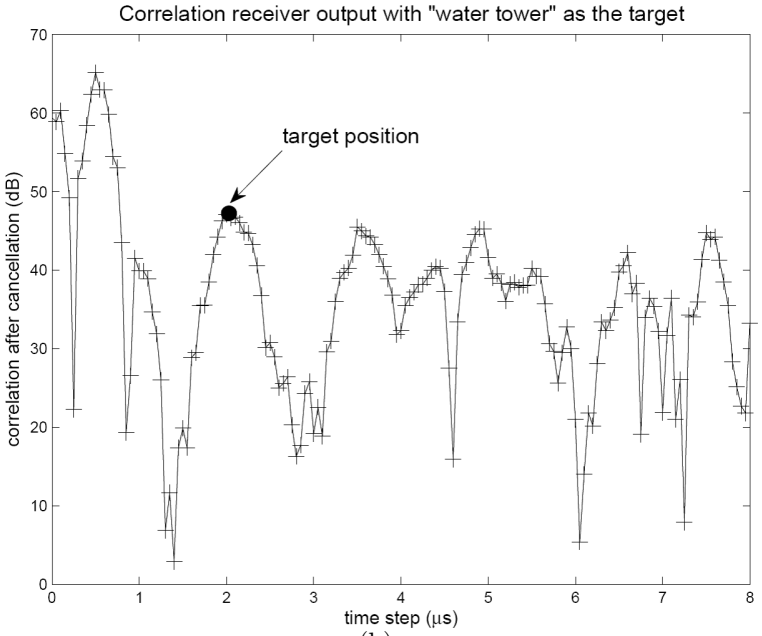

(b)

Figure 3.18: Field experiment result with "water tower" as the target. The water tower is about 300m away from the radar observation position#1. (a) and (b) are results from two different PPM/PM waveforms, both meet the optimization criteria.

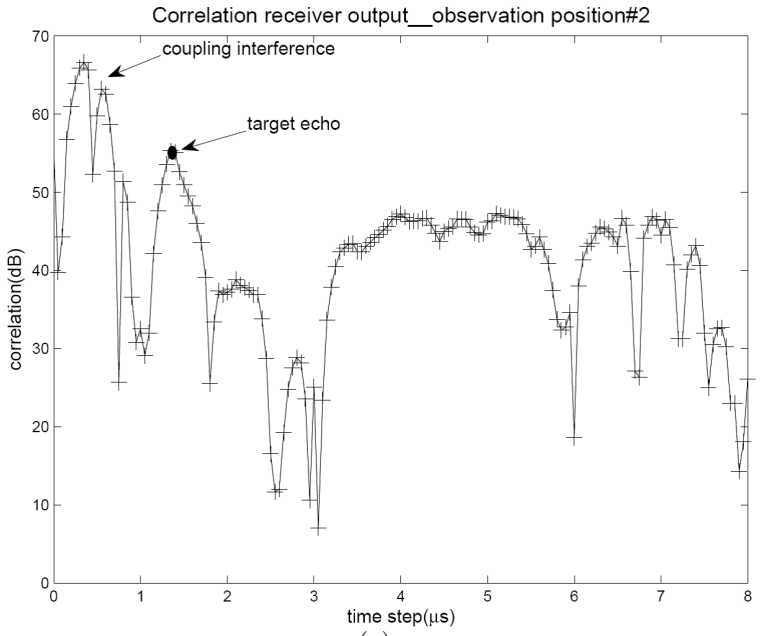

(a)

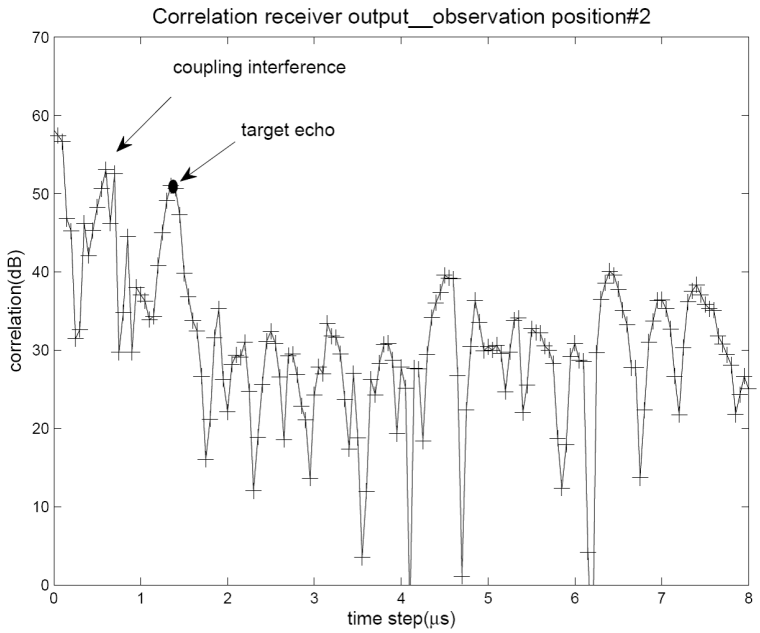

(b)

Figure 3.19: Field experiment result with "water tower" as the target. The water tower is about 200m away from the radar observation position#2. (a) and (b) are results from two different PPM/PM waveforms corresponding to Fig. 3.18 (a) and (b).

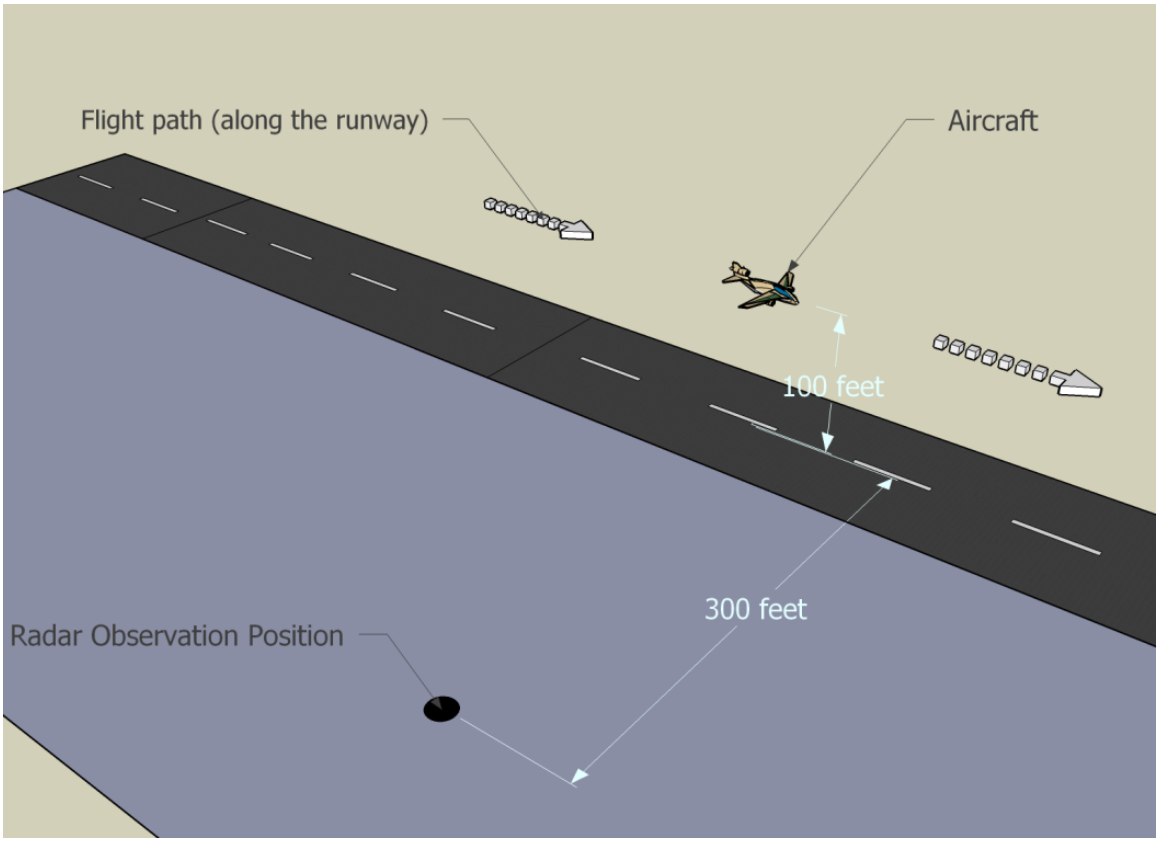

Figure 3.20: The setup for the airport flight test. The aircraft cruises along the runway (a flight path shown in white arrows) at a fixed height of 100 feet. And the radar observation position is located at about 300 feet away from the center of the runway.

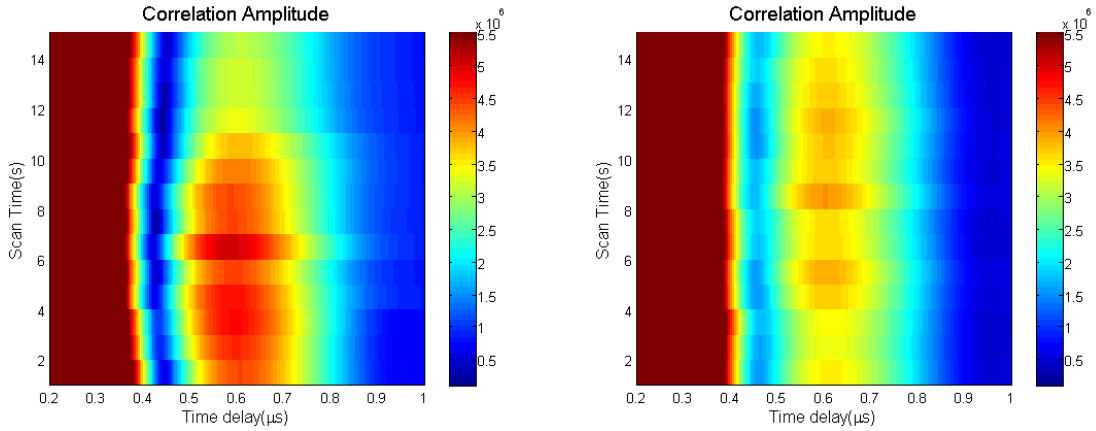

(a) (b)

Figure 3.21: Flight experiment result with significant target signatures. The horizontal coordinate is the time delay based on distance between the radar and the target; the vertical coordinate is the time step of the radar data (one scan for every second) when the aircraft is flying along the runway (15 second data are collected in this case). The figures show the amplitude of the matched filter correlation. (a) Flight #1, flight altitude 100 ft, (b) Flight #2, flight altitude is 200 ft.

Chapter 4

Adaptive Pulse Compression

4.1 Adaptive Sidelobe Mitigation Algorithms

In the previous Chapter, we focus on the sidelobe mitigation algorithm of pulse compression. In particular, we are seeking a methodology for waveform design optimization. A good autocorrelation function of the waveform itself is fundamental to our optimization problem. It sets a lower bound for the sidelobe level that can be reached. In this Chapter, however, we pay our attention to a waveform-independent sidelobe mitigation algorithm, which intends to further reduce the sidelobe levels set by the waveform itself and achieve optimal estimation of ground-truth.

4.1.1 Least Square (LS) Estimation

Consider a discrete radar signal model, where the transmitted waveform signal is defined as $\mathbf{s} = [s_0\ s_1\ \cdots\ s_{N-1}]^T$. The radar scattering field is described by L samples of the range profile impulse response: $\mathbf{x} = [x(0)\ x(1)\ \cdots\ x(L-1)]^T$. The received echo signal is denoted as $\mathbf{y} = [y(0)\ y(1)\ \cdots\ y(L+N-2)]^T$. The length of $\mathbf{s}$, $\mathbf{x}$ and $\mathbf{y}$ are N, L and $L+N-1$, respectively. Fig. 4.1 shows the concept of the signal model.

With the above definition, the receiving signal samples $\mathbf{y}$ is related to the transmitted signal $\mathbf{x}$ by

$$\mathbf{y} = \mathbf{S} \cdot \mathbf{x} + \mathbf{v} \tag{4.1}$$

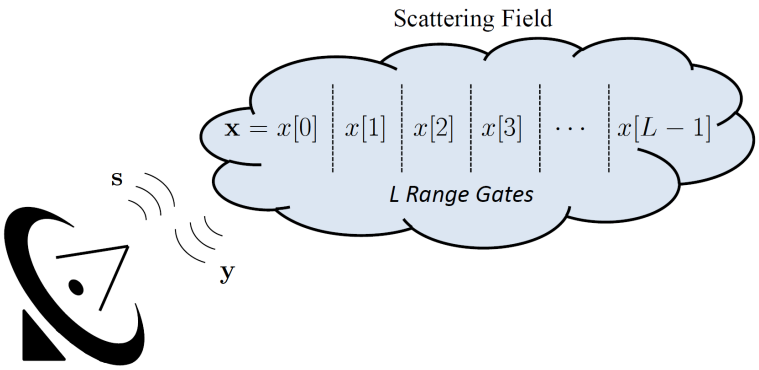

Figure 4.1: Concept of radar signal model

where

$$\mathbf{S} = \begin{bmatrix} s_0^* & 0 & \cdots & & \cdots & 0 \\ \vdots & s_0^* & & & & \vdots \\ s_{N-1}^* & \vdots & \ddots & & & \\ 0 & s_{N-1}^* & & \ddots & & \vdots \\ \vdots & 0 & \ddots & & \ddots & 0 \\ & & & \ddots & & s_0^* \\ \vdots & \vdots & & & \ddots & \vdots \\ 0 & 0 & \cdots & \cdots & 0 & s_{N-1}^* \end{bmatrix} \tag{4.2}$$

$\mathbf{v}$ is a white noise vector of length $L+N-1$. $\mathbf{S}$ is a Toeplitz matrix (Golub and Loan 1996) of $L-N+1 \times L$.

Then, the least square estimate can be employed to derive the optimal ground truth impulse response estimation:

$$\hat{x}_{LS} = (\mathbf{S}^T\mathbf{R}^{-1}\mathbf{S})^{-1}\mathbf{S}^T\mathbf{R}^{-1}\mathbf{y} \tag{4.3}$$

where $\mathbf{R}$ is the $L+N-1 \times L+N-1$ covariance matrix of noise vector $\mathbf{v}$.

One of the drawback of LS algorithm is that it requires available all the receiving samples corresponding to one transmitted pulse, i.e. $L+N-1$ samples. In order to reduce the number of samples required for each processing, we can truncate the

receiving samples into blocks with size of N. This can reduce significant amount of memory especially when $L >> N$. This truncated LS algorithm is called TLS (Truncated Least Square). The implementation of TLS is similar to LS as in Eq. (4.3). Replace the original variables with truncated ones, yields

$$\hat{x}_{TLS} = (\mathbf{S}_t^T \mathbf{R}_t^{-1} \mathbf{S}_t)^{-1} \mathbf{S}_t^T \mathbf{R}_t^{-1} \mathbf{y}_t \tag{4.4}$$

where $\mathbf{S}_t, \mathbf{R}_t$ and $\mathbf{y}_t$ are truncated version of $\mathbf{S}, \mathbf{R}$ and $\mathbf{y}$.

4.1.2 Recursive Minimum Mean Square Error (RMMSE) Algorithm

LS algorithm should obtain statistically optimized estimation of ground truth in theory. However, implementation of LS to pulse compression faces issues such as large matrix for inversion, windows effect, and sensitivity to noise. To overcome the drawback of direct calculation algorithms such as LS, an adaptive iterative algorithm was proposed by (Blunt and Gerlach 2006). Instead of a matrix-wise cost function in LS algorithm, the RMMSE algorithm employs a point-wise cost function. This is equivalent to transforming the overall optimization problem into a partial solution without significantly degrading the performance. The MMSE cost function is,

$$\mathbf{c}(n) = \mathbf{E}\left[\|x(n) - \mathbf{w}^H(n)\mathbf{Y}(n)\|^2\right] \tag{4.5}$$

where $n = 0, 1, \cdots, L-1$. $\mathbf{E}$ denotes expectation. $\mathbf{w}(n)$ has a dimension of $N \times 1$, which is to match the waveform length N. $\mathbf{Y}(n) = [y(n)\ y(n+1)\ \cdots\ y(n+N-1)]$. Take the partial derivative of both sides of Eq. (4.5) with respect to $\mathbf{w}(n)$, the MMSE filter is found to take the form of

$$\mathbf{w}(n) = (\mathbf{E}[\mathbf{Y}(n)\mathbf{Y}^H(n)])^{-1}\mathbf{E}[\mathbf{Y}(n)x(n)] \tag{4.6}$$

Also, the matrix form of the signal model can be expressed as

$$\mathbf{Y}(n) = \mathbf{A}(n)\mathbf{s} + \mathbf{v} \tag{4.7}$$

where $\mathbf{A}(n)$ is the matrix of the ground truth

$$\mathbf{A}(n) = \begin{bmatrix} x(n) & x(n-1) & \cdots & x(n-N+1) \\ x(n-1) & x(n) & \ddots & \vdots \\ \vdots & \ddots & \ddots & x(n-1) \\ x(n+N-1) & \cdots & x(n+1) & x(n) \end{bmatrix} \tag{4.8}$$

Using Eq. (4.7), Eq. (4.6) can be further simplified as

$$\mathbf{w}(n) = \rho(n)(\mathbf{C}(n) + \mathbf{R})^{-1}\mathbf{s} \tag{4.9}$$

where $\rho(n) = |x(n)|^2$, and $\mathbf{R}$ is the $N \times N$ noise covariance matrix similar to that in Eq. (4.3) . $\mathbf{C}(n) = \mathbf{E}[\mathbf{A}^T(n)\mathbf{s}\ \mathbf{s}^H\mathbf{A}^*(n)]$, The details of this algorithm and implementation related issues can be found in (Blunt and Gerlach 2006).

4.2 Performance Evaluation of 1D RMMSE Algorithm

In this section, the MF, LS, and RMMSE algorithms will be applied to various scenarios where pulse compression is employed. The simulation scenario includes both hard/point and distributed targets. Since the processing of sidelobe is dedicated to range domain, we refer it as 1D algorithm, specifically 1D-RMMSE, 1D-MF (Matched Filter) and 1D-LS (Least Square). In the next section, we will consider the 2D scenario where antenna sidelobe effect is incorporated.

4.2.1 RMMSE with Hard Targets

(Blunt and Gerlach 2006) discussed a scenario where only 2 solitary point targets are present. Fig. 4.2 depicts a similar simulation in which RMMSE, LS, and MF algorithm are compared. The ground truth response is used as a reference. Table. 4.1

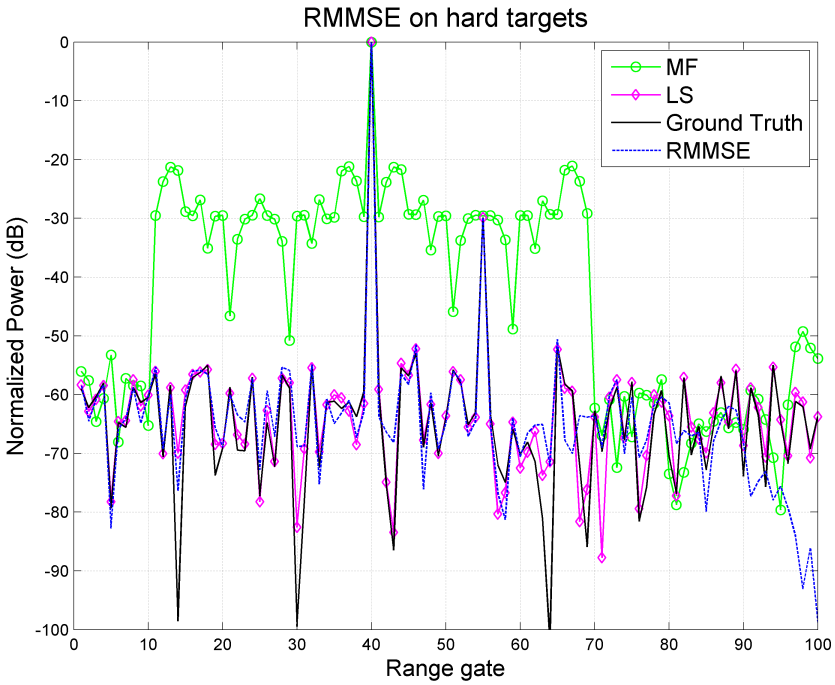

Figure 4.2: Simulation of RMMSE on hard targets

System parameter	Values
Waveform	P3 code
SNR	60 and 30 dB
Target position	gate 40 and 55

Table 4.1: Radar parameters for RMMSE simulation

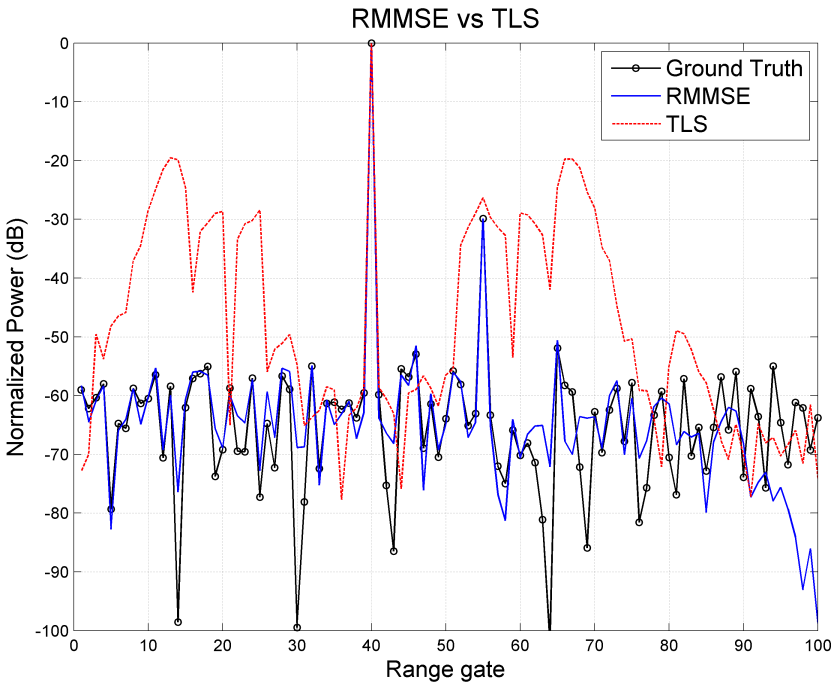

Figure 4.3: Simulation of RMMSE and TLS

lists the key parameters for RMMSE simulation. Fig. 4.3 also shows the results of TLS.

According to the simulation, all the algorithms can accurately estimate the position and signal level of the strong target. For MF algorithm, the sidelobe generated by the strong target is about -22 dB, which corresponds to a SNR of 38 dB. This indicates that anything with a SNR less than 38 dB is very likely to be masked by the strong sidelobe, especially if the weak target lies in proximity of the strong one. MF in this case fails to discern the secondary target. For TLS algorithm, although the weak targets can be recovered, some artifacts also appear due to the truncation effect. Both RMMSE and LS can predict the targets accurately. One interesting observation is that at around gate # 90, RMMSE shows a "drooping" effect. The reason is that ideally RMMSE needs more receiving samples to achieve the similar result as LS. The additional number of samples is proportional to the iteration number.

For a 3-iteration RMMSE, the $2(N-1)$ additional samples are required to obtain comparable result to LS.

To numerically characterize the sidelobe mitigation performance, the estimations are further compared with the ground truth. The normalized mean-square-error (MSE) is calculated by using the ground truth as the reference,

$$NMSE(dB) = 10\log\left(\frac{\|\hat{\mathbf{x}}-\mathbf{x}\|^2}{\|\mathbf{x}\|^2}\right) \tag{4.10}$$

where $\hat{\mathbf{x}}$ and $\mathbf{x}$ are the estimate and the ground truth respectively.

Table. 4.2 lists the NMSE for different algorithms, which is based on the simple cases illustrated here. RMMSE for general hard target scenarios has been studied extensively in previous literatures.

Algorithm	NMSE(dB)
MF	-12.33
TLS	-14.02
LS	-54.77
RMMSE	-48.22

Table 4.2: NMSE for hard-target scenario

4.2.2 RMMSE with Distributed Targets

In case of distributed targets, the adjacent ground truth impulse responses are not *uncorrelated*. The potential correlation might affect the estimation accuracy. This can be demonstrated with a scenario where some distributed scatterers are manually created. Fig. 4.4 shows the result. The SNR of the distributed targets varies from 0∼10 dB and they are located from gate #25∼#45. The strong solitary target is about 70 dB above the noise floor. The distributed targets are set to an extreme case where the signal is barely above the noise floor. Form Fig. 4.4, it is obvious that MF

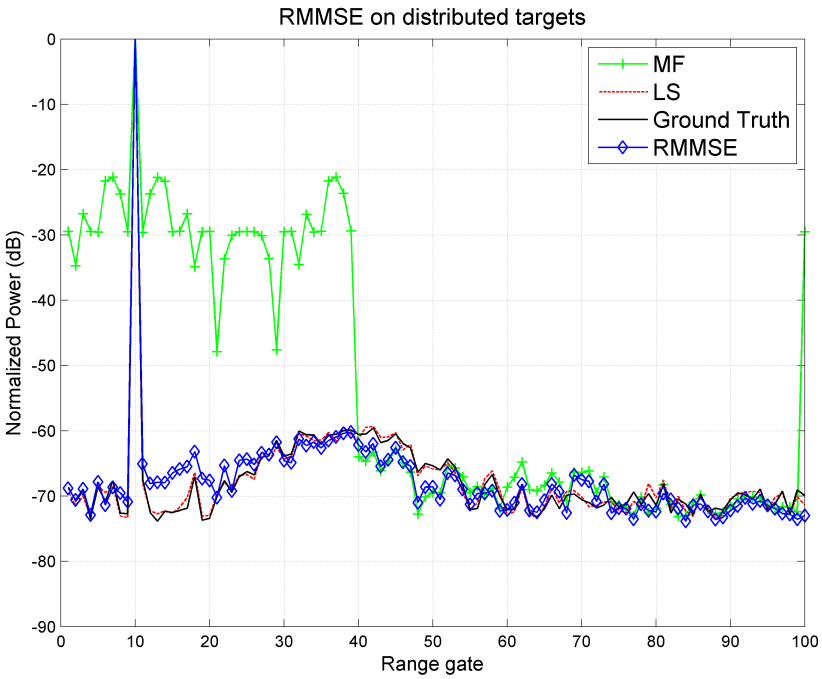

Figure 4.4: Simulation of RMMSE on distributed targets

has a bad correlation with the ground truth. LS has excellent performance. When it comes to RMMSE, the estimation is not as good as LS. In some region close to the strong peak, the sidelobe is much higher than that of LS. This is due to the fact that the "adjacent impulse response" is not uncorrelated. Despite its imperfect estimate accuracy, RMMSE is a much more flexible algorithm in terms of adaptivity, efficiency and tolerance to noise. This will be further discussed. Table. 4.3 lists the NMSE for this example.

4.2.3 Simulation of Weather Radar Observations

The RMMSE algorithm has been applied to an atmospheric filed generated from a high-resolution numerical weather model. A realistic numerical simulation can provide a deterministic and controlled environment for the pulse compression study. There are large amount of random variable having impacts on radar observations.

Algorithm	NMSE(dB)
MF	-10.7
TLS	-13.64
LS	-65.8
RMMSE	-56

Table 4.3: NMSE for distributed-target scenario

The NWP-model based simulation (Alberts et al. (2007); Cheong et al. (2008)) has been accepted as a realistic approach for weather radar simulations and algorithm performance evaluations. Also, the simulations provide important ground truth information for result comparisons. Table. 4.4 lists the key sensor parameters used in this simulation.

Parameters	*Values*
Operating frequency	14 GHz (Ku Band)
PRF	3 KHz
Pulse width	$10\mu s$
Waveform	13-bit Barker code
Receiver Sensitivity	-100 dBm
Max SNR of weather field	45 dB
Scan coverage angle	$-30^\circ \sim 30^\circ$
Number of range gates	$L = 200$
Azimuth resolution	3°

Table 4.4: Key Radar Parameters for Weather Simulation

The simulation begins with the input of Advanced Regional Prediction System (ARPS) data (Xue et al. (2000); Xue et al. (2001); Xue et al. (2003)). Following the

basic procedures given in (Cheong et al. 2008), the input data, including mixing ratio of rain, snow, hail ($[q_r, q_s, q_h]$), wind velocity components ($[u, v, w]$) and turbulent kinetic energy (tke), of each sample point in a severe weather field are read from ARPS, and reflectivity (Z_e) is then calculated from $[q_r, q_s, q_h]$. Monte Carlo simulation is performed for each sample, where 500 scatterers are put into a cubic volume of 1000 m^3. The amplitude and phase of each scatterer are composited together to form the return signal at that particular sampling time. As shown in Eq. (4.11), $x_i[m, n]$ is the return signal for the ith pulse before overlapping at mth gate and nth time step (sub-pulse):

$$x_i[m, n] = \sum_{s'=0}^{S'-1} A^{(s')} exp[-j(\psi^{(s')} + \phi_n)] \tag{4.11}$$

where $A^{(s')}$ and $\psi^{(s')}$ are the amplitude and phase of the s'-th scatterer in the volume as given in (Cheong et al. 2008). ϕ_n is the phase of th waveform sample, $n = 1, 2, \cdots, N$. S' is the number of scatterers in the volume. At the next time step, position of each scatterer is updated according to the wind field and turbulent kinetic energy. Totally N time steps are taken for each range gate, matching the case where N sub-pulse within one pulse arrives sequentially. After samples from all azimuth and range positions are taken, return signal is superposed from gate to gate to form oversampled return with sidelobe effects, as given in Eq. (4.12):

$$y[i, j] = \sum_{\forall m+n-1=j} x[m, n] + \nu \tag{4.12}$$

where $y[i, j]$ is the radar signature for the jth gate of ith pulse (PRTs) and ν represents additive white Gaussian noise. After superposing, the antenna steers to the next azimuth direction, and repeats the above procedures until the complete scan is finished.

In addition to the numerical model, the simulation also emulates two hard targets with a SNR of 45 dB and 25 dB. The RMMSE, LS, MF and TLS algorithms are then applied to the above mixed scenario. Fig. 4.5 shows the result.

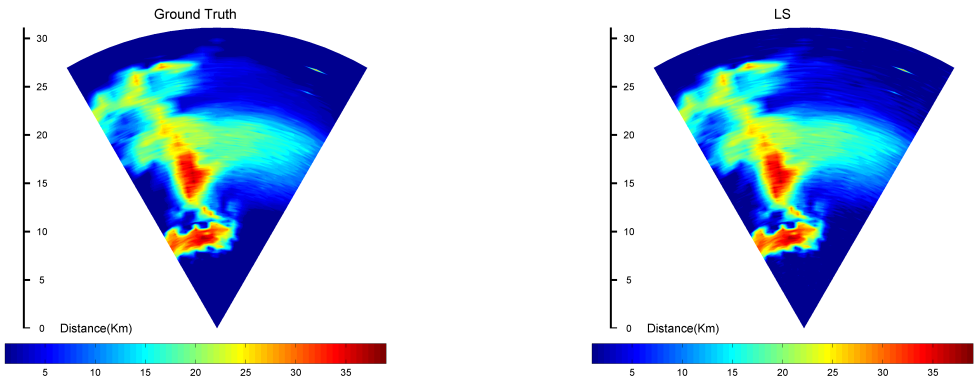

(a)

(b)

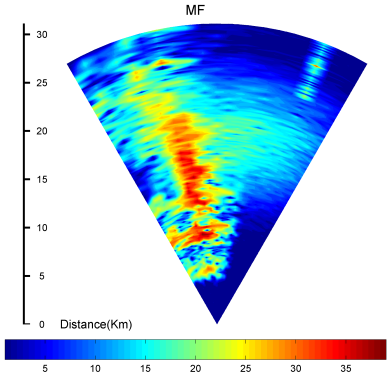

(c)

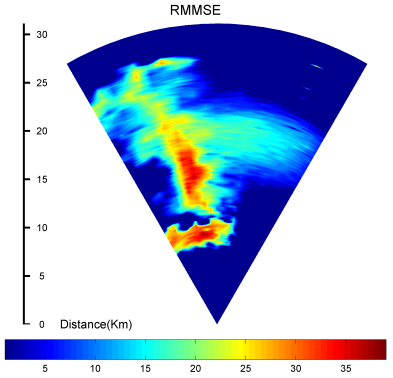

(d)

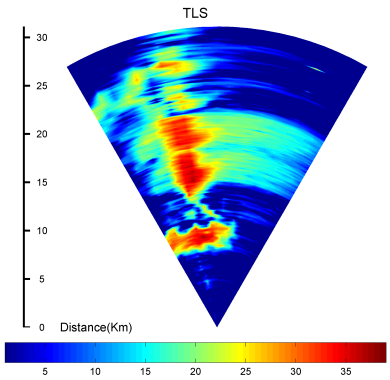

(e)

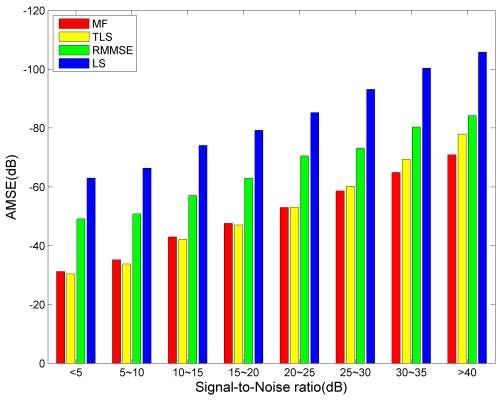

(f)

Figure 4.5: Estimation of weather reflectivity based on the simulated radar with parameters listed in Table. 4.4. The antenna sidelobe effect is not considered in this case. SNR ranges from -5 to 45 dB over the entire scan. (a) Ground truth (sidelobe-free SNR in dB referenced to -100 dBm receiver noise floor), (b) LS estimate result, (c) MF result, (d) RMMSE result - 3 iterations, (e) TLS result, (f) AMSE result

To numerically characterize sidelobe mitigation performance, the estimations are further compared to the ground truth in Fig. 4.5(a) cell-by-cell. The average mean-square-error (AMSE) for a particular SNR category is calculated through the following procedure: (1) Add 20 realizations of random fluctuation term v to receive signals (with sidelobe contamination); (2) For each iteration, use three different methods (MF, LS and RMMSE) to estimate, and calculate errors by comparing the results to the ground truth; (3) Average the errors of 20 time Monte-Carlo simulation, as the averaged error term ϵ for each radar cell; (4) Average the ϵ again among all the resolution cells belonging to the same SNR category; (5) Normalize the result from step (4) with unit signal amplitude (the result is denoted as $\bar{\varepsilon}$) and convert to dB scale, according to:

$$AMSE = 10 \log 10 \left[|\bar{\varepsilon}|^2 \right] \tag{4.13}$$

The simulation indicates that LS has the best overall performance. Both RMMSE and LS can sufficiently suppress the sidelobe despite of the slightly downgraded performance for RMMSE. TLS has good mitigation by visual inspection. MF fails to recover both the weather and hart targets as expected. Fig. 4.5(f) shows the statistics for the simulation. In terms of AMSE, MF and TLS are at the same level. LS outperforms RMMSE by about 10 dB.

4.2.4 Impact of Antenna Sidelobes

Simulations in Section 1.2.3 do not consider the effect of antenna sidelobes. In a radar system, the antenna effect on the system performance can be significant. Antenna response can bias the reflectivity, velocity and spectrum width estimates. The sidelobes introduced from both pulse compression waveform (Bucci and Urkowitz (1993); Mudukutore et al. (1998); Zhu et al. (2008)) and antenna radiation patterns (Doviak and Zrnic 1984) can lead to degraded, or "masked" target signatures. Sidelobes are generally known as the leakage of energy from the desired spatial focal point, thus

bringing in the interferences from neighboring resolution gates/cells. In airborne and spaceborne application, the antenna sidelobe is limited by the aperture size, which causes further degradation. To address the issue of both pulse compression and antenna sidelobe, we construct a joint signal model based on two-dimensional convolution. We assume the antenna effect only at the azimuth direction which is perpendicular to the radar line-of-sight. The antenna pattern is assumed to generated from a uniform linear array.

For a solitary point target, sidelobes are expected from both the range and azimuth direction. In Fig. 4.6, a point target is processed with MF and an antenna pattern of uniform linear array. Fig. 4.6 shows that in this simplest case, sidelobe will affect any target within 15 range gates and $\pm 10^{\circ}$ in azimuth (assuming -40 dB SNR). Furthermore, the sidelobe contamination is actually extended to a two-dimensional square-shape area instead of a cross-shape in range and azimuth.

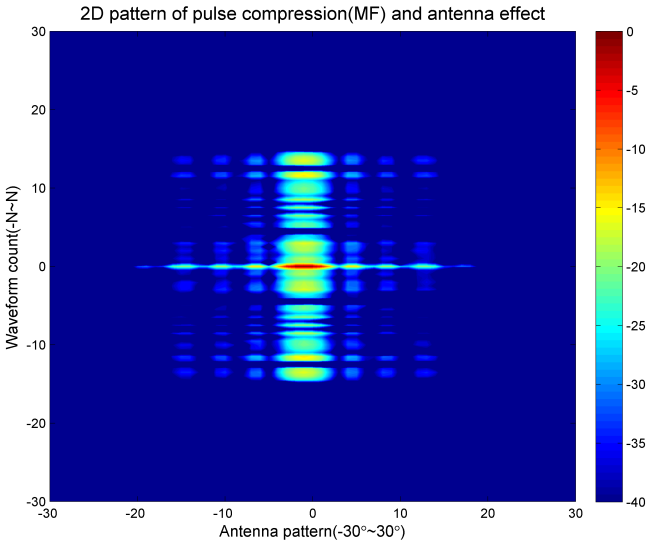

Figure 4.6: Joint pattern of antenna and pulse compression

A 2D simulation is generated to verify the performance of various algorithms in presence of antenna sidelobe effects. The procedure is similar to the one adopted in Eq. (4.11) and Eq. (4.12). To imitate pulse compression and beam sidelobe effects

while balancing computation load and accuracy, the array beam pattern and pulse compression waveforms are uniformly sampled. There are a total of M samples in beam pattern $\mathbf{a}$ and N sub-pulses in the transmit waveform $\mathbf{s}$. By adding the antenna effect, the formula can be updated as,

$$x(l,k) = \sum_{m=1}^{K_s} \lambda^{(m)} exp(-j\psi^{(m)}) \tag{4.14}$$

$$\beta(l',k',n) = a_{k'} \cdot x(l,k) \cdot exp(-j\phi_n) \tag{4.15}$$

In equation Eq. (4.14), $\beta(l',k',n)$ is the raw return signal at l'th range bin, k'th sampled beam pattern angular position and nth time step (sub-pulse). K_s is the number of scatterers in the volume; $a_{k'}$ is the antenna radiation pattern response at the k'th beam angular position, $k' = 1, 2, \cdots, M$; $\lambda^{(m)}$, $\psi^{(m)}$ are the amplitude and phase of the mth scatterer in the volume computed from Mie scattering model, ϕ_n is the phase of nth waveform sample, $n = 1, 2, \cdots, N$. Both $\lambda^{(m)}$ and $\psi^{(m)}$ are l, k dependent. At the next time step, the position of each scatterer is updated according to the wind field and turbulent kinetic energy. A total of N time steps are taken for each range bin, as in the case where N sub-pulses within one pulse arrive sequentially. After samples from all the angular beam positions and range bins are taken, the return signal is *superposed* from range bin to range bin and beam position to beam position, to form the oversampled return with sidelobe effects, as given in Eq. (4.16):

$$y(l) = \sum_{\forall k'} \sum_{\forall l'+n-1=l} \beta(l',k',n) + \nu \tag{4.16}$$

where $y(l)$ is the composite radar return signal (due to the pulse compression and antenna sidelobe effects) for the lth range bin ($l = 1, 2, \cdots, L$) at a particular azimuth scanning angle, $\forall$ is the mathematical "for all" symbol and ν represents additive white Gaussian noise. After superposing, the antenna steers to the next azimuth direction, and repeats the above procedures until a complete scan (scanning azimuth angle from 1 to K) is finished.

A simulation with the same weather ground profile as before is generated using the above technology. In addition to the parameters listed in Table. 4.4, the antenna pattern is based on a 10-element uniform linear array. The radar scanning angle is $-30^\circ \sim 30^\circ$. The antenna pattern is composed of 21 samples from $-15^\circ \sim 15^\circ$. The azimuth resolution is 3°. The simulation result is presented in Fig. 4.7. The antenna effect on the azimuth direction is quite significant (Fig. 4.7(b)$\sim$(e)). The hard targets spread the antenna sidelobe in azimuth in particular. It is obvious that the pulse compression processing on range domain can not resolve the antenna sidelobe issue. Thus, sidelobe mitigation algorithms should be developed for both range and azimuth dimensions.

4.2.4.1 Sequential 1D Processing

One possible solution for the 2D sidelobe mitigation problem is to perform sequential 1D processing. From Eq. (4.14) and Eq. (4.15), the antenna radiation pattern samples $a_{k'}$ is applied to each range profile as a weighting function. Impacts of both antenna and pulse compression sidelobes can be characterized by the convolution operation. Conceivably, RMMSE, LS and MF algorithms can be used to mitigate antenna sidelobes in a similar way as mitigating pulse compression sidelobes. Thus, the 1D sequential mitigation applies the adaptive pulse compression algorithm on range domain and then the azimuth direction. Since the processing in the two dimensions are treated independently, the order of range or azimuth processing does not matter. As is seen from Fig. 4.8, the antenna sidelobe effect has been removed for LS and RMMSE. The result of RMMSE is very promising. Fig. 4.8(e) indicates that the antenna sidelobe has been removed by RMMSE and the overall mitigation result is very comparable to the LS result in Fig. 4.8(b).

It is noted that sequential 1D processing is very computationally intensive. The inversion of $N \times N$ matrix has to be solved in each range gate for a specific azimuth

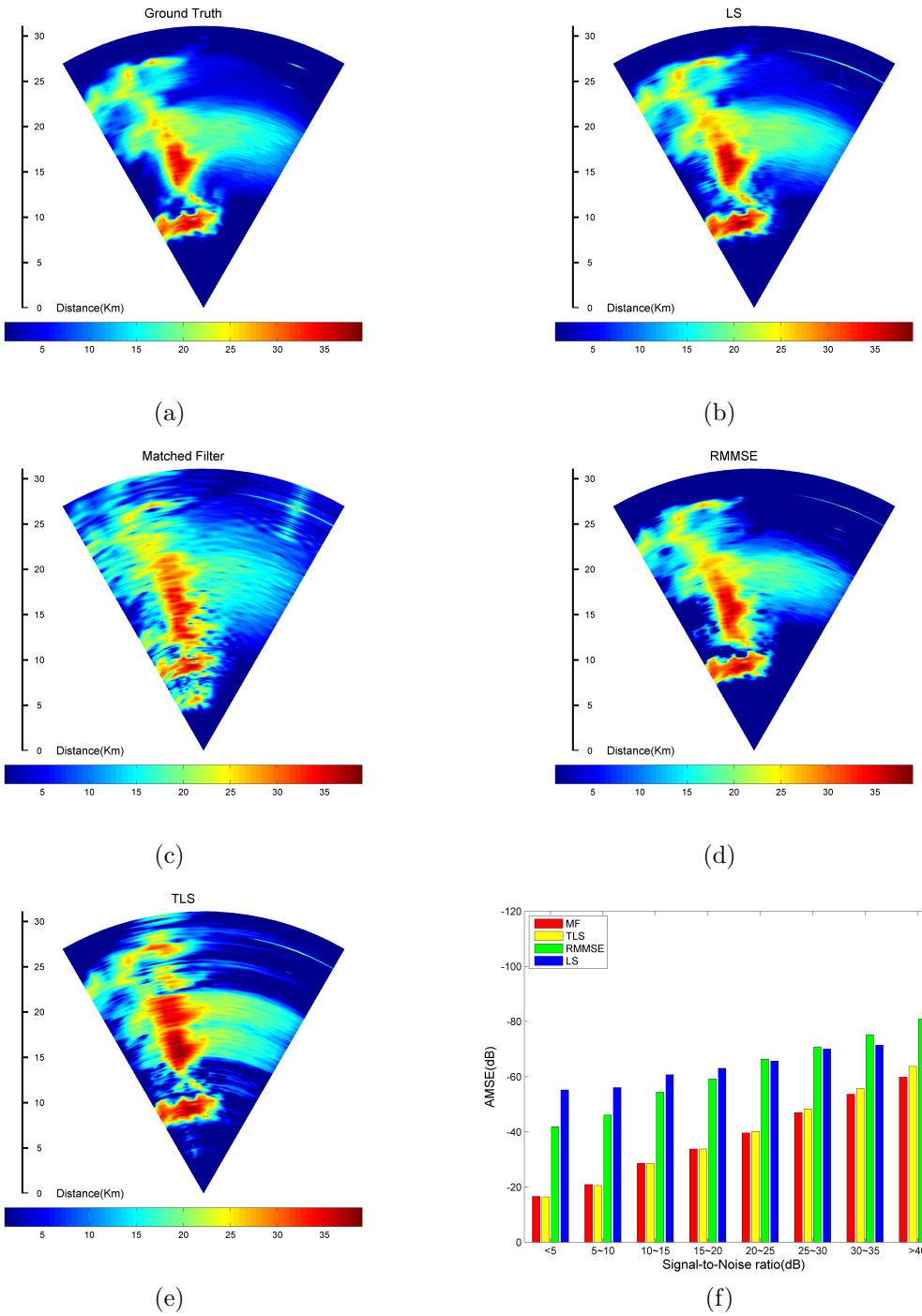

Figure 4.7: Estimation of weather reflectivity based on the simulated radar with parameters listed in Table. 4.4 and ULA antenna pattern. SNR ranges from -5 to 45 dB over the entire scan. (a) Ground truth (sidelobe-free SNR in dB referenced to -100 dBm receiver noise floor), (b) LS estimate result, (c) MF result, (d) RMMSE result - 3 iterations, (e) TLS result, (f) AMSE result

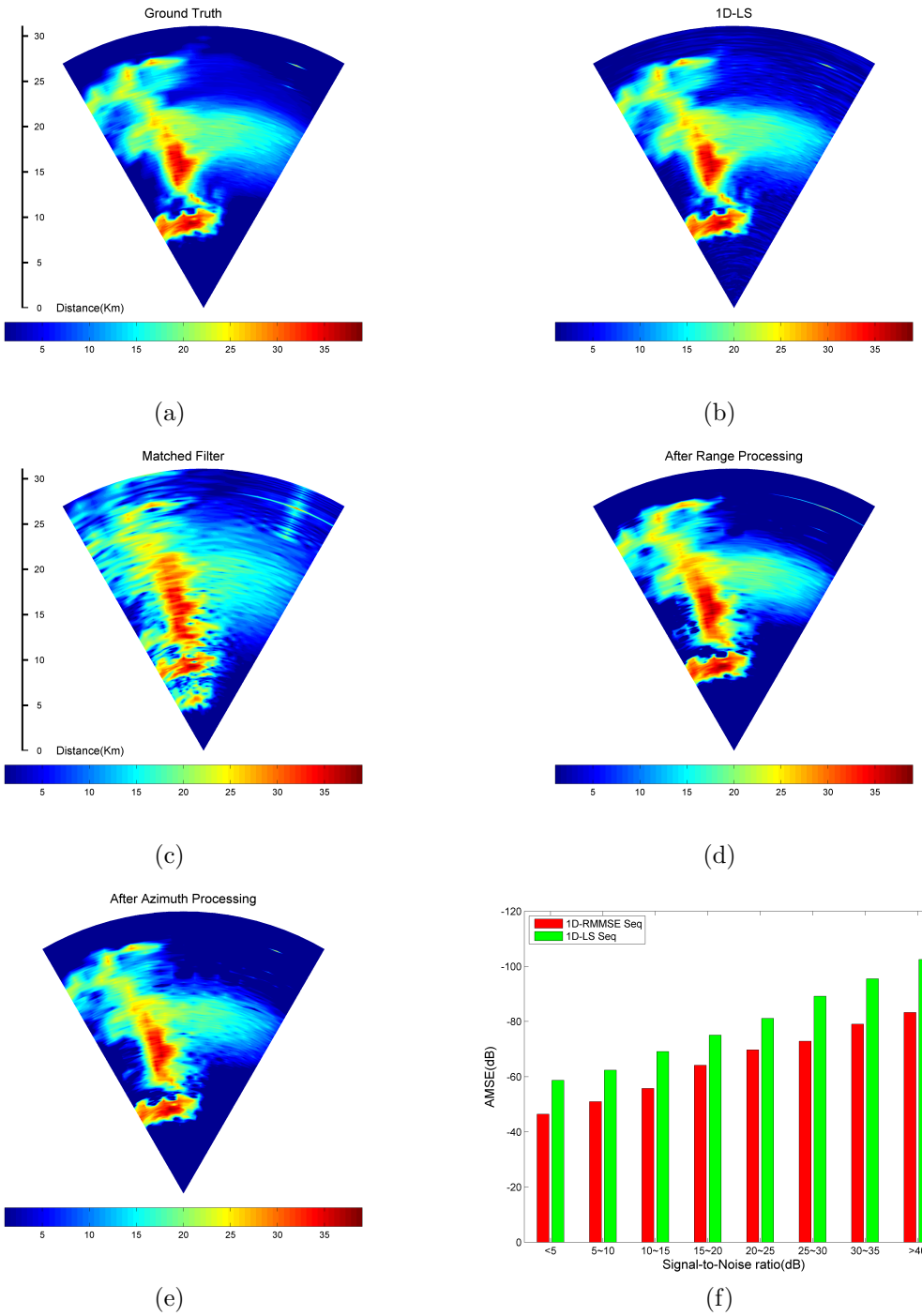

Figure 4.8: Estimation of weather reflectivity based on the simulated radar with parameters listed in Table. 4.4 and ULA antenna pattern. SNR ranges from -5 to 45 dB over the entire scan. (a) Ground truth (sidelobe-free SNR in dB referenced to -100 dBm receiver noise floor), (b) 1D LS estimate result, (c) 1D MF result, (d) Result after range RMMSE, (e) Result after azimuth RMMSE, (f) AMSE result

angle. Roughly $\mathcal{O}(N^3LK)$ computational operations are required. Therefore, the sequential algorithm is not recommended from the perspective of practical implementation.

4.3 Theory of 2D Sidelobe Mitigation Algorithms

4.3.1 Improved Radar Signal Model

A 2D signal model has to be developed in order to find a more efficient sidelobe mitigation algorithm. Instead of a 1D ground truth $x(n)$, consider a two-dimensional scatterer field $x(l,k)$. The index l represents the range resolution bin and the index k represents the azimuth angle. Assuming N samples of the time-waveforms are transmitted, denoted as $\mathbf{s} = [s_0\ s_1\ \cdots s_{N-1}]^T$. Also, assume M samples of the angular positions are illuminated by the antenna and the corresponding radiation pattern response is defined as $\mathbf{a} = [a_0\ a_1\ \cdots a_{M-1}]^T$. To address the typical forward-looking scenario and simplify the discussion, only the 1D azimuth direction antenna pattern is considered in this study. Due to the extended pulse width and antenna radiation pattern, the received radar echoes from the lth range bin and kth azimuth angle can be written as

$$y(l,k) = \Big[\sum_i \sum_j s_i\ a_j\ x(l-i+1, k-j+1)\Big] + v \tag{4.17}$$

with $1 \le l \le L+N-1, 1 \le k \le K+M-1$ and $\max(1, l+1-L) \le i \le \min(l, N), \max(1, k+1-K) \le j \le \min(k, M)$, L is the number of range bins and K is the number of azimuth scan angles. v is the combined receiver noise from thermal noise and oscillator sources, and is assumed as additive white Gaussian. This expression is essentially a two-dimensional discrete convolution among $\mathbf{s}, \mathbf{a}$ and the ground truth.

4.3.2 Derivation of the 2D-LS and RMMSE procedures

First, to simplify the matrix representation, the following expression is introduced to describe the ground truth and receiving sample matrices:

$$\mathbb{C}_x(l,k,N,M) = \Big[x(i,j)\Big]_{i=l,l+1,\cdots,l+N-1;\ j=k,k+1,\cdots,k+M-1} \tag{4.18}$$

In other words, $\mathbb{C}_x(l,k,N,M)$ is an $N \times M$ matrix with $x(i,j)$ as its elements. The element in the first row and the first column is $x(l,k)$.

As an example,

$$\mathbb{C}_x(1,1,2,3) = \begin{bmatrix} x(1,1) & x(1,2) & x(1,3) \\ x(2,1) & x(2,2) & x(2,3) \end{bmatrix} \tag{4.19}$$

In addition, it is convenient to define a generalized Toeplitz matrix (Golub and Loan 1996) that represents the convolution operation in Eq. (4.17), with

$$\mathbb{T}_{\mathbf{z}}(D) = \begin{bmatrix} z_1 & 0 & \cdots & \cdots & 0 \\ \vdots & z_1 & & & \vdots \\ z_P & \vdots & \ddots & & \vdots \\ 0 & z_P & & \ddots & 0 \\ \vdots & 0 & \ddots & & z_1 \\ \vdots & \vdots & & \ddots & \vdots \\ 0 & 0 & \cdots & 0 & z_P \end{bmatrix}_{(D+P-1)\times D} \Rightarrow \mathbb{T}_{\mathbf{s}}(3) = \begin{bmatrix} s_0 & 0 & 0 \\ \vdots & s_0 & 0 \\ s_{N-1} & \vdots & s_0 \\ 0 & s_{N-1} & \vdots \\ 0 & 0 & s_{N-1} \end{bmatrix}_{(3+N-1)\times 3} \tag{4.20}$$

where $\mathbf{z}$ is a P-element vector with $\mathbf{z} = [z_1, z_2, \cdots, z_P]^T$, and D is the number of columns in the Toeplitz matrix. The number of rows is always $D+P-1$. The $\mathbb{T}_{\mathbf{s}}(3)$ in equation Eq. (4.19) illustrates the concept of this notation.

Using the above definitions, Eq. (4.17) can be converted into matrix representation using

$$\bar{Y} = S \cdot X \cdot A^H + V \tag{4.21}$$

where $X = \mathbb{C}_x(1,1,L,K)$, $\bar{Y} = \mathbb{C}_y(1,1,L+N-1,K+M-1)$, $S = \mathbb{T}_{\mathbf{s}}(L)$, $A = \mathbb{T}_{\mathbf{a}}(K)$, and V is a Gaussian noise matrix.

2D-LS estimation, which supposes the optimum estimation of X in terms of mean square error, can be readily obtained and is shown in Eq. (4.22):

$$\hat{X}_{LS} = (S^H S)^{-1} S^H Y A (A^H A)^{-1} \tag{4.22}$$

In contrast, 2D-RMMSE estimation leads to a recursive and adaptive procedure operating on *a portion of the observation data* for each iteration. In this work, a point-wise version of MMSE cost function is defined as

$$\xi = \mathbf{E}\left[\|x(l,k) - \mathbf{w}^H \mathbf{Y} \mathbf{u}\|^2\right] \tag{4.23}$$

where $\mathbf{w}$ and $\mathbf{u}$ are the range $(N \times 1)$ and azimuth $(M \times 1)$ sidelobe suppression filters, respectively. $\mathbf{E}[\cdot]$ denotes the expectation operator. $\mathbf{Y}$ is an N by M block matrix given by

$$\mathbf{Y} = \mathbb{C}_y(l,k,N,M) \tag{4.24}$$

The 2D Matched filter (2D-MF) is usually used as the initial stage of RMMSE. It is obtained by setting $\mathbf{w} = \mathbf{s}$,$\mathbf{u} = \mathbf{a}$, such that the 2D-MF estimate of x(l,k) is

$$\hat{x}_{MF}(l,k) = \mathbf{s}^H \mathbf{Y} \mathbf{a} \tag{4.25}$$

To derive the 2D-RMMSE estimate of $x(l,k)$, Eq. (4.21) can be further elaborated as a block-wise expression according to Eq. (4.17):

$$\mathbf{Y} = \mathbf{S}^H \mathbf{X} \mathbf{A} + \mathbf{V} \tag{4.26}$$

where $\mathbf{X} = \mathbb{C}_x(l-N+1, k-M+1, 2N-1, 2M-1)$, $\mathbf{S} = \mathbb{T}_{\mathbf{s}}(N)$, $\mathbf{A} = \mathbb{T}_{\mathbf{a}}(M)$. $\mathbf{S}$ is a $(2N-1) \times N$ matrix and $\mathbf{A}$ is a $(2M-1) \times M$ matrix. $\mathbf{X}$ has a dimension of $(2N-1) \times (2M-1)$, and $\mathbf{V}$ is an N by M Gaussian noise matrix. Using Eq. (4.23), the optimal filter coefficients $\mathbf{w}$ and $\mathbf{u}$ can be obtained to minimize ξ. Taking the

partial derivatives of Eq. (4.23) with respect to $\mathbf{w}$ and $\mathbf{u}$, and setting the results to zero, after some manipulation, we obtain

$$\begin{cases} \mathbf{w} = \left(\mathbf{E}[\mathbf{Y}\mathbf{u}\mathbf{u}^H\mathbf{Y}^H]\right)^{-1} \cdot \mathbf{E}[\mathbf{Y}x^*(l,k)\mathbf{u}] \\ \\ \mathbf{u} = \left(\mathbf{E}[\mathbf{Y}^H\mathbf{w}\mathbf{w}^H\mathbf{Y}]\right)^{-1} \cdot \mathbf{E}[\mathbf{Y}^H x^*(l,k)\mathbf{w}] \end{cases} \tag{4.27}$$

Furthermore, combined with Eq. (4.26), Eq. (4.27) can be simplified with the assumption that the adjacent ground truth terms are uncorrelated, as

$$\mathbf{w} = \left(\mathbf{S}^H\Omega\mathbf{S}\right)^{-1} \cdot \mathbf{s} \cdot \mathbf{a}^H\mathbf{u} \cdot \rho(l,k) \tag{4.28}$$

where $\rho(l,k) = |x(l,k)|^2$ which is the power of the ground profile response, and $\Omega = \Lambda[\boldsymbol{\rho}^{1/2} \cdot \Lambda[\mathbf{A}\mathbf{u}\mathbf{u}^H\mathbf{A}^H] \cdot (\boldsymbol{\rho}^{1/2})^H]$, $\boldsymbol{\rho} = \mathbb{C}_\rho(l-N+1, k-M+1, 2N-2, 2M-2)$ is the element-wise square of $\mathbf{X}$. $\Lambda[\cdot]$ denotes the operation that preserves the diagonal elements of a square matrix and zeroes out the others.

4.3.3 Algorithm Implementation

After obtaining the filter coefficients $\mathbf{w}$ and $\mathbf{v}$, the MMSE estimation of $x(l,k)$ is computed with

$$\hat{x}(l,k) = \mathbf{w}^H\mathbf{Y}\mathbf{u} \tag{4.29}$$

Note that the filter coefficients $\mathbf{w}$ and $\mathbf{u}$ are calculated for each *specific* (l,k), i.e. each range bin l and azimuth angle k. Eq. (4.28) is an iterative expression. The current filter coefficients $\mathbf{w}$, $\mathbf{u}$ and the ground truth power $\rho(l,k)$ can be utilized to generate filter coefficients for the next iteration. Also, as a special form of RMMSE, Eq. (4.28) alternatively iterates between two dimensions (2D-RMMSE). The dimensions of the processing window for 2D-RMMSE are always $N \times M$. Fig. 4.9 depicts the detailed computation flow of 2D-RMMSE. Simulations have verified that for *uncorrelated point scatterers*, $2 \sim 4$ iterations are enough to produce a result comparable to the LS estimator.

Due to lack of prior knowledge about $\mathbf{w}$, $\mathbf{u}$ and the ground truth $x(l,k)$ at initialization, the matched filter coefficients $\mathbf{w}_0 = \mathbf{s}$ are used at the beginning of the 2D-RMMSE process. So, the initial estimation of the ground truth is essentially the matched filter output. The initial ground truth estimate can use the uniform (All-1s) matrix. Similarly, the initial filters $\mathbf{w}$ or $\mathbf{u}$ can be set to a normalized uniform vector. It is noted that the matrix dimension of Y is reduced by $2(N-1)$ rows and $2(M-1)$ columns from iteration to iteration. Therefore, for 2D-RMMSE implementation with I iterations, the sample matrix Y is zero-padded to a size of $[L+(2I-1)(N-1)] \times [K+(2I-1)(M-1)]$ at initiation.

4.4 Evaluation of 2D Sidelobe Mitigation Algorithms

4.4.1 2D-RMMSE Simulation

The 2D-RMMSE and 2D-LS algorithms are applied to the simulated weather targets. The key parameters are listed in Table. 4.5. For 2D-RMMSE, the number of iterations is set to 4, and $u_0 = a$ with $\boldsymbol{\rho}$ set to a uniform matrix initially. The 2D matched filter (2D-MF) is also applied here for comparison.

Fig. 4.10 presents the results after converting the computed receiving signal power to the signal-to-noise ratio (SNR) for an airborne radar scan. For this case, the return signal power ranges from -105$\sim$-55 dBm, the noise floor is set to -100 dBm, so the maximum SNR is 45 dB. It is obvious that 2D-MF (Fig. 4.10(c)) has the worst performance, as the weather signature is severely affected by the sidelobes. From visual inspection, 2D-LS seems to have less estimation errors than 2D-RMMSE around the regions with high reflectivity, compared with the ground truth in Fig. 4.10(a).

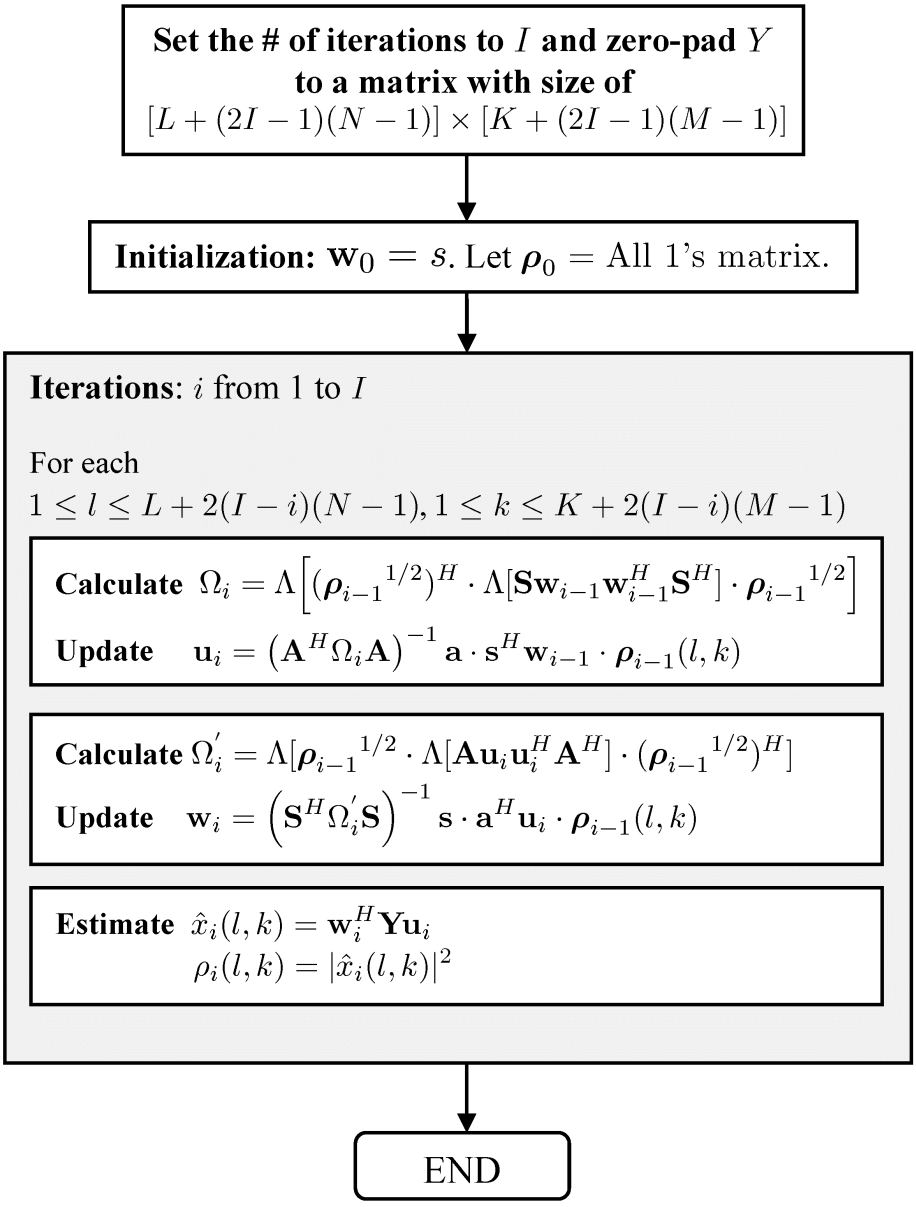

Figure 4.9: Illustration of 2D-RMMSE algorithm

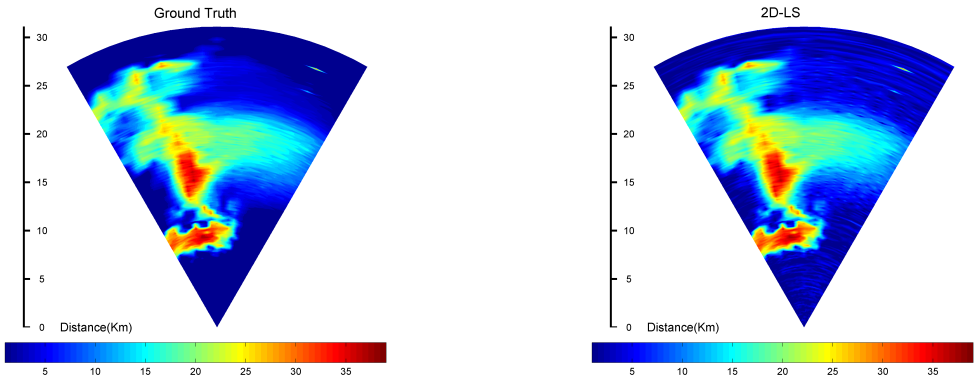

(a) (b)

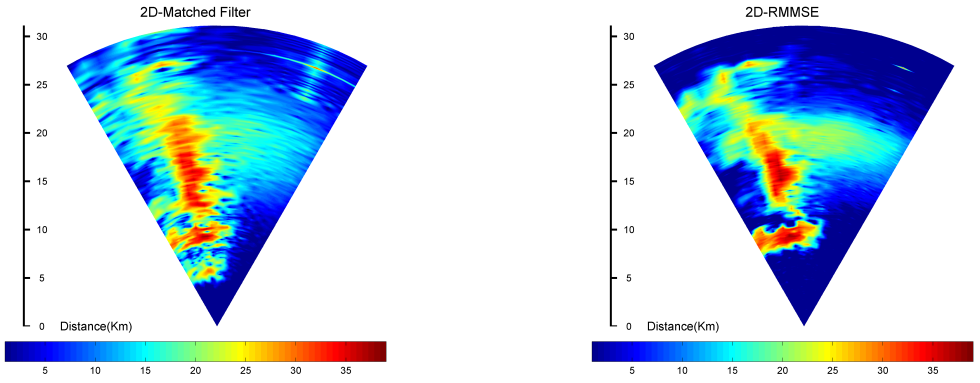

(c) (d)

Figure 4.10: Estimation of weather reflectivity based on the simulated radar with parameters listed in Table. 4.5. SNR ranges from -5 to 45 dB over the entire scan. (a) Ground truth (sidelobe-free SNR in dB referenced to -100 dBm receiver noise floor), (b) 2D-LS estimate result, (c) 2D-MF result, (d) 2D-RMMSE

Parameters	*Values*
Antenna pattern azimuth coverage	$-15^\circ \sim 15^\circ$
Max SNR of weather field	45 dB
Receiver noise level	-100 dBm
Scan coverage angle	$-30^\circ \sim 30^\circ$
Number of range bins	$L = 200$
Number of azimuth angles in the scan	$K = 21$
Azimuth resolution for plotting	3°

Table 4.5: Key parameters of simulated scenarios for weather sensing

Fig. 4.11(a) shows the SNR distribution (percentage of occurrence) of the simulated weather scenario in Fig. 4.10. There are 4200 weather cells ($L \times K$) in this simulation. The SNR from -5 dB to 45 dB is divided into 8 bins, as shown in Fig. 4.11(b). The AMSE corresponding to each SNR bin is calculated using Eq. (4.13). Fig. 4.11(b) shows the AMSE comparison of the three algorithms. As expected for most cases, AMSE values decrease as the SNR level increases. Both RMMSE and MF show about 10 dB variation of AMSE, while the AMSE of LS changes more than 20 dB. Theoretically, the estimation performance bound of 2D-LS is proportional to noise power, while the estimation performance of 2D-RMMSE is also related to the statistical correlations among the neighboring ground truth responses. Based on similar observations from many simulations, it is safe to conclude that 2D-RMMSE has better noise immunity than 2D-LS for low Signal-to-Noise Ratio (SNR) or Signal-to-Clutter Ratio (SCR) scenarios.

4.4.2 Computation Load Considerations

Table. 4.6 gives the computation load estimations of 2D-MF, 2D-LS and 2D-RMMSE. Compared with the 2D-LS algorithm, the 2D-RMMSE needs less memory, since only

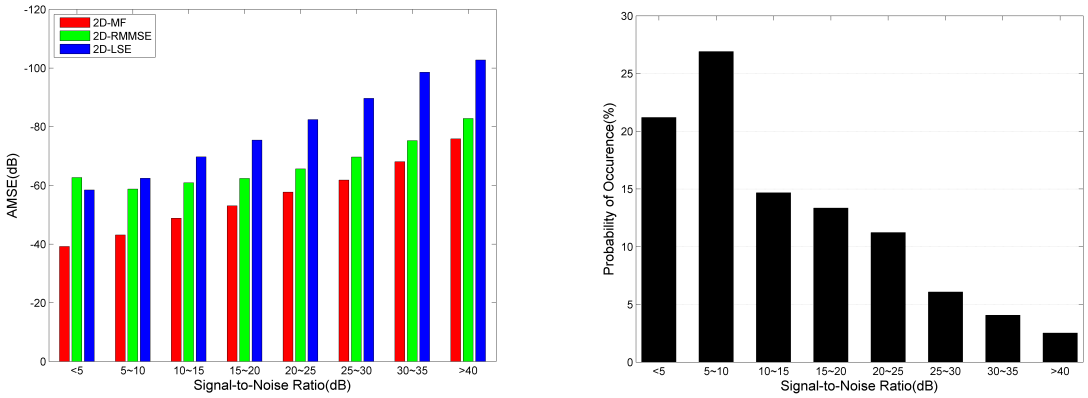

(a) (b)

Figure 4.11: AMSE of reflectivity estimation. (a) AMSE comparison of different sidelobe suppression techniques with 20 Monte-Carlo simulation runs (For 2D-RMMSE, the result of iteration #4 is used), (b) The SNR distribution of the simulated weather scenario with respect to -100 dBm noise level.

an $N \times M$ receiving matrix block $\mathbf{Y}$ is required to calculate $\hat{x}(l,k)$ at each specific resolution cell (l,k). For 2D-LS, the required data sample matrix size is $L \times K$(the entire scan).

	2D-MF	*2D-LS*	*2D-RMMSE*
Number of Operations	$\mathcal{O}(NMLK)$	$\mathcal{O}(L^3+K^3)^\dagger$	$\mathcal{O}(N^3LK+M^3LK)$
Memory Requirement	$N \times M$	$L \times K$	$N \times M$

Table 4.6: Computational requirement of sidelobe mitigation algorithms

† This would be $\mathcal{O}(LK^2+KL^2)$, provided that the 2D-LS filter coefficients are pre-calculated.

In term of computational complexity, 2D-LS is more appropriate for short-range, airborne hazard avoidance radar as L and K can be small but N and M may need to be sufficiently large to achieve required resolutions. RMMSE has a significant advantage for the scenarios of scanning over large spatial volume, long range (which is more common for ground-based weather radars and scientific radars), and using

small antenna aperture (i.e., cannot afford extra low sidelobe antennas). After the third iteration, the number of operations required to implement 2D-RMMSE will be $\mathcal{O}(N^3 + M^3)$ at each range bin and azimuth angle. In addition, a tradeoff may be made by RMMSE between computational efficiency and error performance by choosing appropriate M and N values. The primary computation burden of 2D-RMMSE results from matrix inversions. A possible way to speed-up the RMMSE computation is to exploit the Toeplitz structures of $\mathbf{A}$ and $\mathbf{S}$ in Eq. (4.28).

4.4.3 Comparison to 1D Sidelobe Mitigations

Fig. 4.12 presents the MSE comparison between 1D sequential and 2D mitigations, using MF, LS and RMMSE. The MSE difference between 1D and 2D processing is not significant for MF and LS. This is because the azimuth and range domain for MF and LS are independent during the implementation of algorithms. The 2D approaches for MF and LS essentially improve the computational efficiency without performance degradation. For RMMSE, however, the 2D algorithm not only reduces the computational load but also boost the MSE performance. This improvement along with the *waveform template tolerance* is believed to be the main contribution of the 2D-RMMSE algorithm.

4.5 The Application of Waveform-Independent Adaptive Pulse Compression to Practical Radars

4.5.1 Algorithm Implementation

Several issues arise when implementing the adaptive pulse compressions to practical radars: *a.* A waveform template $\mathbf{s}$ is required for accurate estimation. In practice, this

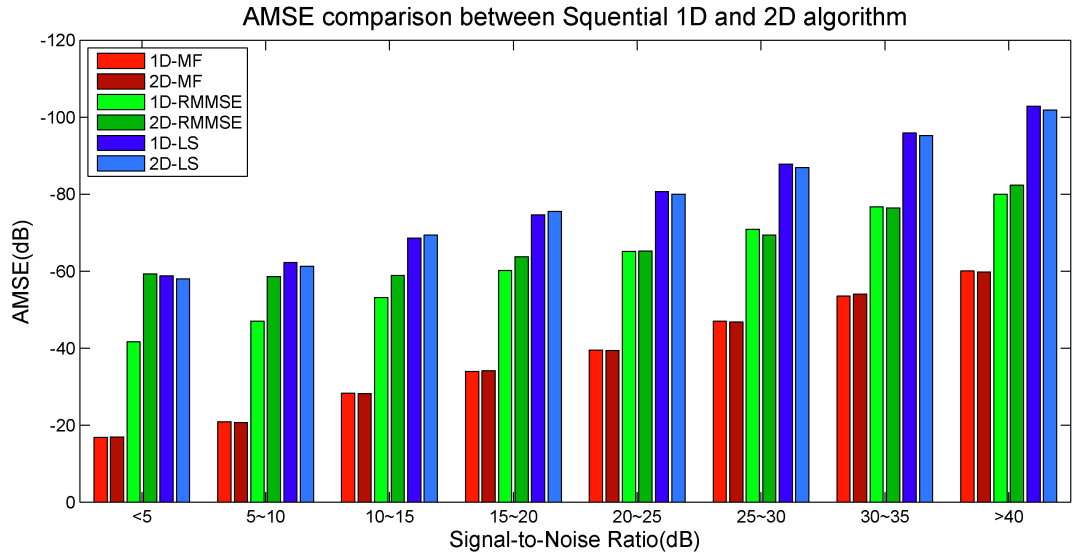

Figure 4.12: AMSE comparison between Sequential 1D and 2D algorithm

template is usually acquired by sampling the RF transmitting signal before antenna. *b.* The noise covariance matrix plays an important role in estimation accuracy of RMMSE and LS especially for the region of "noise floors". *c.* Downsampling data properly can also reduce the computational load and improve the performance of sidelobe mitigation, while too much downsampling will lose the precision of waveform matching with template.

4.5.1.1 Waveform Template

The waveform **s** is a prior knowledge for pulse compression. Theoretically, the original waveform generated by the *waveform generator* can be used as the template for pulse compression. However, the original waveform is contaminated with noise and distortion during the process of digital-to-analog conversion, modulation, RF upconversion, RF amplification, etc. So, the transmitted RF signal is not exactly the same as its baseband digital waveform any more. This could lead to the degraded sidelobe mitigation performance. To overcome the nonlinearity and noise on the waveform

template, many modern radars utilize the technique of sampling the RF transmitted signal. Instead of the original baseband waveform, the receiver uses this *contaminated* waveform as the template for pulse compression. Fig. 4.13 shows a typical X-band weather radar which uses the coupling technique to obtain the transmitted waveform.

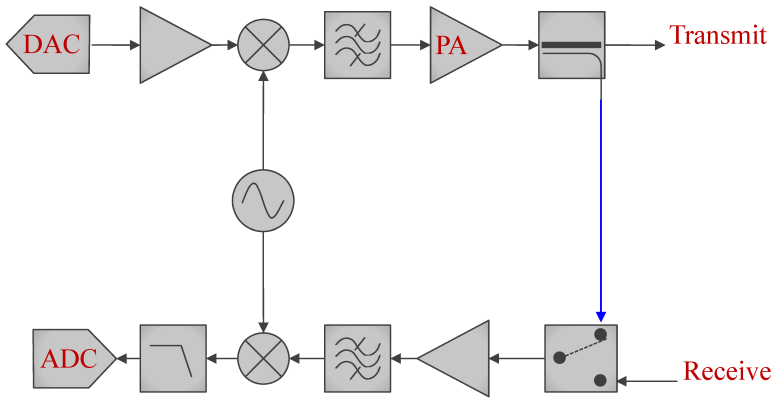

Figure 4.13: Typical Radar diagram using coupling technique to obtain transmitted waveform

There are two problems of this approach. First, additional hardware is needed to couple and loop back to the receiver, which also add significant requirements on the TR isolations. Second, the sampled transmitted waveform template still contains noise and other nonlinear effect during the RF-to-baseband conversion. These distortions are out-of-control and can significantly increase the sidelobe levels. To further investigate the sensitivity of RMMSE and LS algorithm to waveform template distortions, we develop a closed-form perturbation model for RMMSE and LS.

For LS algorithm, (Lewis et al. 2006) has developed an analytical expression for predicting the impact of model error. Assume the new model matrix $\bar{S}$ can be expressed as

$$\bar{S} = S + \epsilon E \tag{4.30}$$

where ϵ is the small perturbation constant, and E is the error matrix including all the error introduced by baseband-to-RF conversion. Then the new LS estimate of the ground truth can be derived by combining Eq. (4.3) and Eq. (4.30)

$$\hat{\bar{x}}_{LS} = (\bar{S}^T R^{-1} \bar{S})^{-1} \bar{S}^T R^{-1} y \approx \hat{x}_{LS} - \epsilon (S^T R^{-1} S)^{-1} S^T R^{-1} E \cdot \hat{x}_{LS} \tag{4.31}$$

For RMMSE, to simplify the derivation of the error model, an alternative version of Eq. (4.1) can be written as

$$\mathbf{y} = \mathbf{S} \cdot \mathbf{X} + \mathbf{v} \tag{4.32}$$

where

$$\mathbf{S} = \begin{bmatrix} 0 & \cdots & & \cdots & 0 & s_0 & \cdots & s_{N-1} \\ & \cdots & & 0 & s_0 & \cdots & s_{N-1} & 0 \\ \vdots & & 0 & & \cdots & & & \vdots \\ 0 & & \cdots & & 0 & & \vdots & \vdots \\ s_0 & \cdots & s_{N-1} & 0 & \cdots & & \cdots & 0 \end{bmatrix} \tag{4.33}$$

$$\mathbf{X} = [x(l-N+1)\ x(l-N+2)\ \cdots\ x(l)\ \cdots\ x(l+N-2)\ \cdots\ x(l+N-1)]^T \tag{4.34}$$

Also, assume the contaminated waveform template is

$$\bar{\mathbf{S}} = \mathbf{S} + \epsilon \mathbf{E} \tag{4.35}$$

Then the new RMMSE estimate of $\bar{x}(l)$ is defined as

$$\hat{\bar{x}}(l) = \mathbb{E}(\mathbf{y}\mathbf{y}^T)^{-1} \mathbb{E}(\mathbf{y} \cdot x(l)) \tag{4.36}$$

Substitute with Eq. (4.32) and Eq. (4.36), yields

$$\hat{\bar{x}}(l) = \mathbb{E}(\bar{\mathbf{S}}\mathbf{X}\mathbf{X}^T \bar{\mathbf{S}}^T)^{-1} \mathbb{E}(\bar{\mathbf{S}}\mathbf{X} \cdot x(l)) \tag{4.37}$$

$$= \left(\mathbf{S}\mathbf{X}_2\mathbf{S}^T\right)^{-1} \cdot \bar{s} \tag{4.38}$$

where

$$\mathbf{X}_2 = \begin{bmatrix} \rho(l-N+1) & \cdots & 0 & \cdots & 0 \\ \vdots & \ddots & \vdots & \ddots & \vdots \\ 0 & \cdots & \rho(l) & \cdots & 0 \\ \vdots & \ddots & \vdots & \ddots & \vdots \\ 0 & \cdots & 0 & \cdots & \rho(l+N-1) \end{bmatrix} \tag{4.39}$$

with $\rho(l) = ||x(l)||^2$ and $\bar{s} = s + \epsilon \cdot e$. After further simplification, the new RMMSE estimate is

$$\hat{\bar{x}}(l) = \hat{x}(l) + \epsilon \left[e^T \Lambda^{-1} + \mathbf{S}^T \Lambda^{-1} \Psi \Lambda^{-1} \right] \mathbf{y} \tag{4.40}$$

where $\Lambda = \mathbf{S}\mathbf{X}_2\mathbf{S}^T$ and $\Psi = -E\mathbf{X}_2\mathbf{S}^T - \mathbf{S}\mathbf{X}_2E^T$.

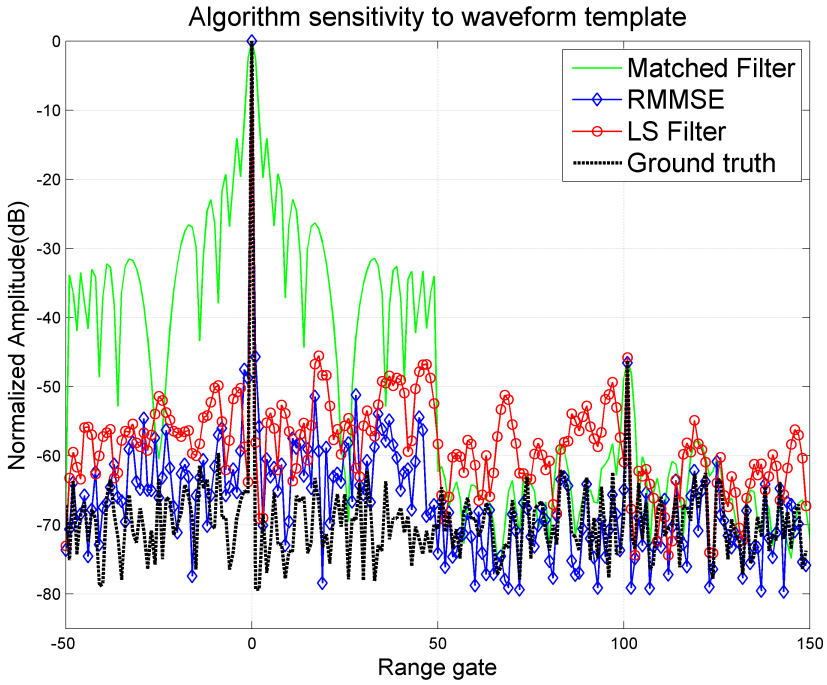

Figure 4.14: Algorithm sensitivity to waveform template inaccuracy. *The waveform used in this case is a Haming-windowed chirp signal.* $\epsilon = 1e^{-2}, E = randn$*-Matlab®. Two hard targets exist at Gate#1,#100 with SNR of 65 and 20dB separately.*

In order to investigate the impacts of waveveform template on different algorithms, a simulation is developed, in which the waveform template is contaminated only by noise for simplicity. Fig. 4.14 shows the simulation output. The result indicates that the RMMSE and MF both has a much better immunity to noise interference. For LS, erroneous estimation appears all over the field, even though LS has almost perfect performance of sidelobe reduction in the initial simulation. The waveform template simulation illustrates that LS is very sensitive to the waveform template error, which limits the algorithm for practical use. RMMSE and MF have certain waveform tempalte immunity, which makes them more attractive for implementations.

According to the waveform error model of Eq. (4.31) and Eq. (4.40), the estimation inaccuracy caused by random perturbation can be reduced by taking average of the estimates from multiple pulses, i.e. $\mathbb{E}\left[\hat{\hat{x}}\right] = \hat{x}$, since $\mathbb{E}[E] = 0$ and $\mathbb{E}[e] = 0$. It is equivalent to the non-coherent pulse integration. In practice, the pulse integration might be affected by the target radar cross-section fluctuation. This will be demonstrated via real radar data in next section.

4.5.1.2 Noise Covariance Estimate

Without appropriate estimation of the noise covariance, RMMSE algorithm may suffer from numerical instability. Accurate estimating of noise covariance is key to achieve good sidelobe reduction performance. In practical implementation, the noise consists of not only thermal noise but also some environmental interference. A common method to estimate noise covariance matrix is to select the radar data where there is no target or "clear weather", and then take the corresponding data samples $\mathbf{y}$ to get the estimate of R. Simulation and real implementation has proven the feasibility of this method.

4.5.1.3 Doppler Effect

As mentioned in Chapter 2, the Doppler effect does have some impact on pulse compression. Doppler shift introduced by moving targets generates mismatch between the original transmit waveform and the receive signal. Therefore, it is essentially a waveform template issue. (Blunt and Gerlach 2006) has shown that RMMSE has better Doppler immunity than LS and MF algorithms. Fig. 4.15 simulates the impact of Doppler effect on RMMSE. There are two point-targets located in Gate #50 and #57 with SNR of 65 dB and 25 dB, respectively. The simulated radar frequency is at S-band (3 GHz). The stronger target has a radial velocity of 60 m/s. The other target has zero Doppler speed. The RMMSE can still achieve -50 dB sidelobe level for the stronger target with such significant Doppler shift. In rare cases where the Doppler effect is overwhelming, Doppler filter bank (Shin et al. (2003); Wang and Akansu (2012)) can be adopted to further reduce the Doppler impact. It is also observed that the Doppler impact on sidelobe mitigation is not significant for RMMSE implementations on practical weather radar data, as is discussed in the Section 5.2.

4.5.1.4 Oversampling and Supper-resolution

In modern radar systems, with the advance of digital-to-analog conversion and DSP technique, commercial data acquisition and processing hardware such as FPGA is widely available. Oversampling is frequently performed in digital receivers. The sampling frequency can go up to tens time of the radar signal bandwidth. Some data processing techniques such as *noise whitening filter* (Wei and Rasmussen 1996) and *super-resolution* (Liu and Xiang 1999) rely on the oversampling of the data. RMMSE and LS are both inherently supper-resolution algorithms. The procedure to achieve supper-resolution is straightforward: Apply oversampling on both the received radar data samples $\mathbf{y}$ and waveform $\mathbf{s}$ to obtain oversampled version, $\tilde{\mathbf{y}}$ and waveform $\tilde{\mathbf{s}}$, and then perform RMMSE/LS to $\tilde{\mathbf{y}}$. Fig. 4.16 demonstrates the supper-resolution

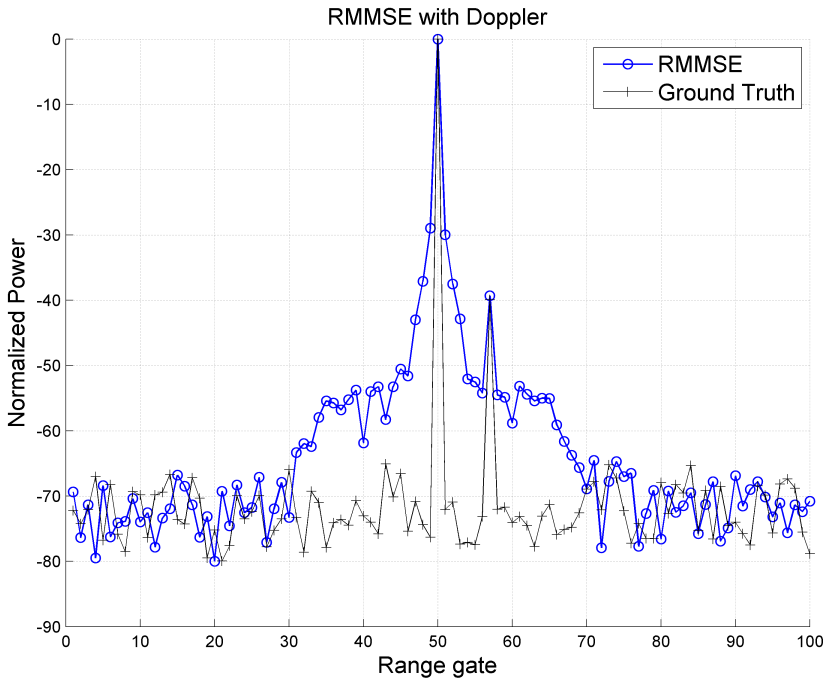

Figure 4.15: The impact of Doppler effect on RMMSE performance. The target at Gate #50 has a Doppler speed of 60 m/s. The waveform used is LKP3 with $N = 30$. Total pulse width $\tau = 30\ \mu s$. Wavelength $\lambda = 10\ cm$. 4 iterations are adopted for RMMSE.

capability of RMMSE and LS along with MF for comparison. MF has no supper-resolution capability since it fails to discern the targets. Both RMMSE and LS suffer from the increased sidelobe caused by oversampling. Extensive follow-on studies show that this sidelobe actually results from the increased noise floor.

From the above observation, if sidelobe is more concerned, the data sampling rate should match the original waveform bandwidth. For example, if the original waveform has 30 samples (such as a LFM signal with $B = 1\ MHz$ and $T = 30\ \mu s$), then the equivalent sampling rate at the receiver should be also around 1 MHz, so that the actual waveform samples match the receiver data samples.

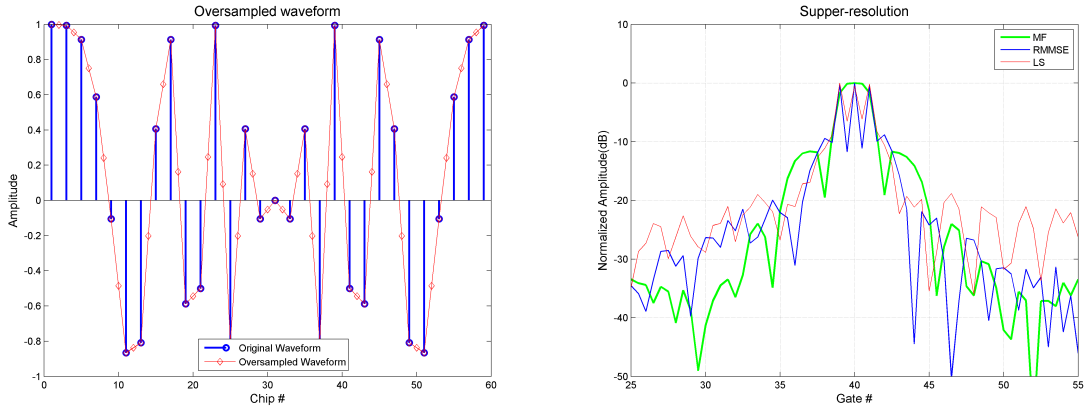

(a) (b)

Figure 4.16: Demonstration of supper-resolution. (a) The oversampled waveform, (b) Simulation of supper-resolution of RMMSE and LS. The waveform used in the simulation is $P3$ code with $N = 30$. 3 point targets are located in Gate# 39, 40 and 41 with equal SNRs

4.5.2 Algorithm Implementations on HIWRAP and PX1000 Radar Data

4.5.2.1 Radar parameters

High-Altitude Imaging Wind and Rain Airborne Profiler (HIWRAP) is a dual-frequency, dual-beam, conical scan, solid-state transmitter-based Doppler radar system (Li et al. 2008). It was designed for operation on the high-altitude (20 km) Global Hawk UAV (Brown et al. 2011).

HIWRAP was configured as fixed nadir pointing with one Ku-band beam and one Ka-band beam. Within each Ku or Ka-band channel, both 20 μs/1MHz LFM chirp and 2 μs conventional pulse are transmitted. Table. 4.7 lists the radar waveform parameters for HIWRAP system for the Ku band channel.

PX1000 is a dual-polarization X-band mobile radar developed by the Advanced Radar Research Center (ARRC) of the University of Oklahoma (OU). It is primarily used as a platform for waveform studies and various signal processing techniques,

Parameters	**Pulse1**	**Pulse2**
Pulse Type	LFM chirp	Short Pulse
Pulse Width (μs)	20	2
Bandwidth (MHz)	1	2
DDS Output (MHz)	114.5	126
Tx IF (MHz)	225.5	214
Tx RF (MHz)	13915.5	13904
RF LO (MHz)	13690	
PRF (Hz)	4516.12/3589.75	
Antenna Gain G_a(dB)	34.8	
Ant Beamwidth Along Track $\phi(^\circ)$	3.07	
Ant Beamwidth Cross Track	2.96	

Table 4.7: Radar parameters for HIWRAP

such as pulse compression, polarimetric signal processing, refractivity retrieval and supplementary validations for field campaigns. Table. 4.8 lists the PX1000 radar parameters.

Parameters	**Values**
Operating frequency	9550 MHz
Typical PRF	2000 Hz
Antenna gain	38.5 dBi
3-dB beamwidth	1.8 °
Peak power	100 W
Maximum pulse width	69 μs
ADC resolution	14 bit
Receive bandwidth	5MHz
Typical gate spacing	30m

Table 4.8: Radar parameters for PX-1000

4.5.2.2 Pulse Compression on HIWRAP

In each data profile, there is one calibration pulse at near range and one surface return at about 20 km range. Fig. 4.17 is the raw data profile for both short and long pulses respectively. For both scenarios, there are 600 samples for each pulse. The range resolution is about 75 meters for LFM and 150 meters for the short pulse. Only the Ku band channel data were used in the following experiments.

Fig. 4.18 shows the processing result of different algorithms. The strongest peak indicates the direct-coupled transmit signal, which is used for system calibration. The sidelobe of this peak is reduced to -66 dB by LS and -75 dB by RMMSE. The secondary peak at around 20 km corresponds to the surface return. This is due to the fact that the aircraft's altitude is 20 km. RMMSE can successfully suppress this

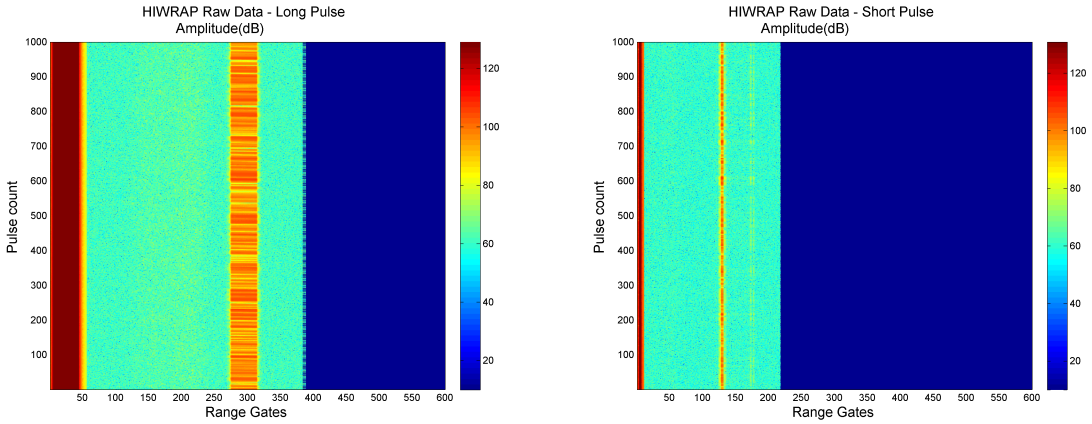

(a) (b)

Figure 4.17: HIWRAP Raw Data Display. (a) Received signal with long pulse (LFM), (b) Received signal with short pulse.

sidelobe to noise floor. However the sidelobe mitigation for MF and LS is limited. In addition, there is some weather signature from 7∼15 km. They are marked with a circled area in Fig. 4.18. They are very weak scatterers: only several dB above noise floor. The short pulse range profile is also plotted for comparison. Obviously, the short pulse has a high noise floor because of the limitation of SNR (limited by the peak power). LS is also suffering from the high estimation error in practice. Both RMMSE and MF can recover the weather signature. Overall, RMMSE has the best performance in this scenario.

The result in Fig. 4.18 is implemented by 50-pulse integration. As is proven by Eq. (4.31) and Eq. (4.36), Pulse integration greatly help to reduce the noise and distortions. Fig. 4.19 compares the case of pulse integration and without pulse integration. It can make a difference upto 10 dB in spite of the slightly degraded SNR in the surface return (1.5 dB).

One important observation from Fig. 4.18 is that LS seems to be comparable to RMMSE in terms of sidelobe. However, the template of LS algorithm has to be very accurate. Fig. 4.20 shows a scenario where the waveform template is slightly off, which is truncated from 60 to 55 chips. The LS fails to suppress the sidelobe,

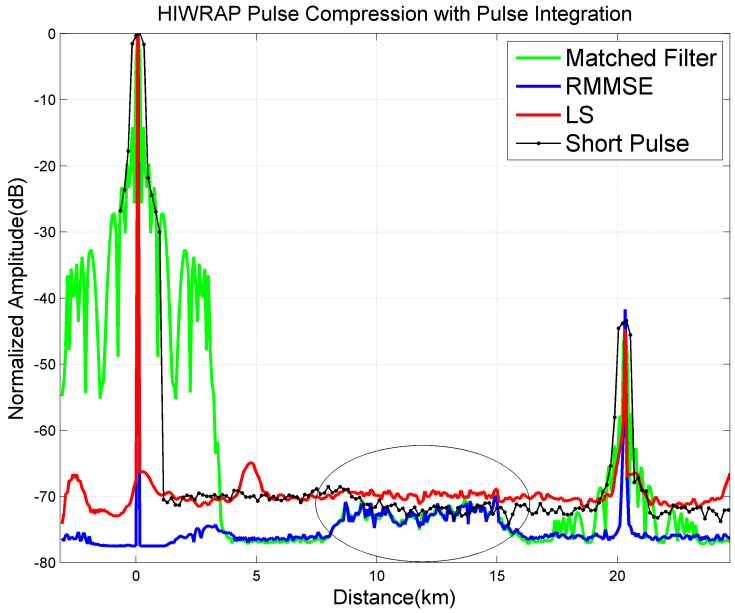

Figure 4.18: HIWRAP pulse compression result with 50-pulse integration

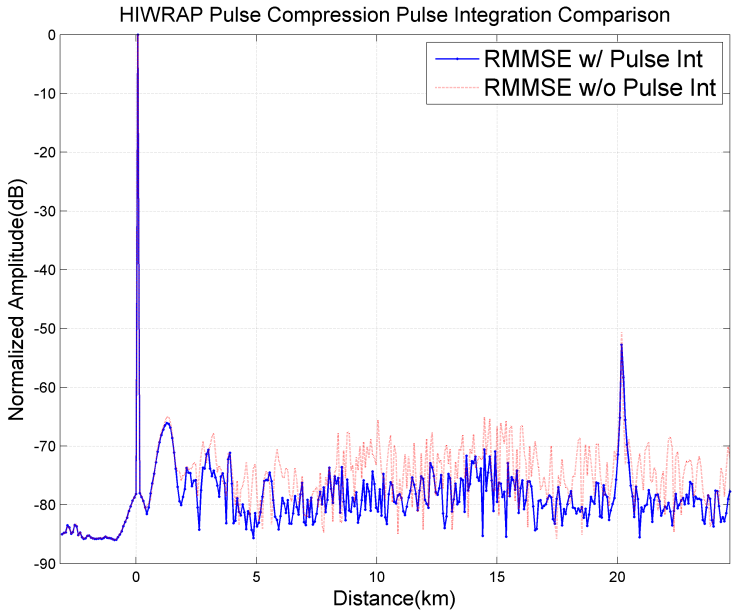

Figure 4.19: HIWRAP pulse compression result with 3-pulse integration and without pulse integration

whereas MF and RMMSE are still tolerant to this template inaccuracy. Even though RMMSE has larger estimate error than using the "good" template, it is not a concern since the errors are only located within the coupling range (<5 km), which has no meteorological activities.

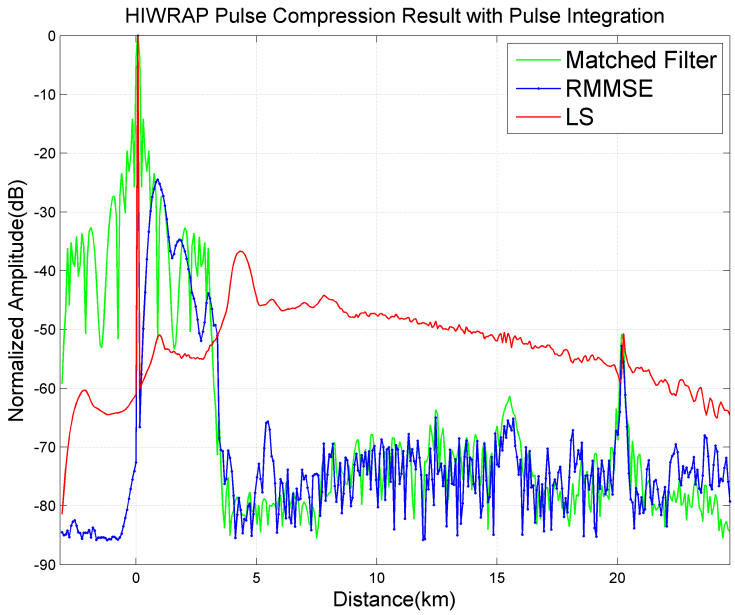

Figure 4.20: HIWRAP pulse compression result with erroneous template

Fig. 4.21 is the waveform template adopted for the best performance of RMMSE and LS. It is noticed that in practice the template is not exactly the same as the original LFM signal. Some samples are distorted as indicated in the circled areas. The template used is also extended compared with the original waveform. The additional "tail" samples help to reduce the noise floor and make LS less sensitive.

4.5.2.3 Pulse Compression on PX-1000

Several different types of waveforms have been implemented in PX1000 radar. These include 13-bit Barker code, P3/P4 code, windowed LFM and nonlinear FM. In addition, there are both hard and distributed targets existing in the radar observation

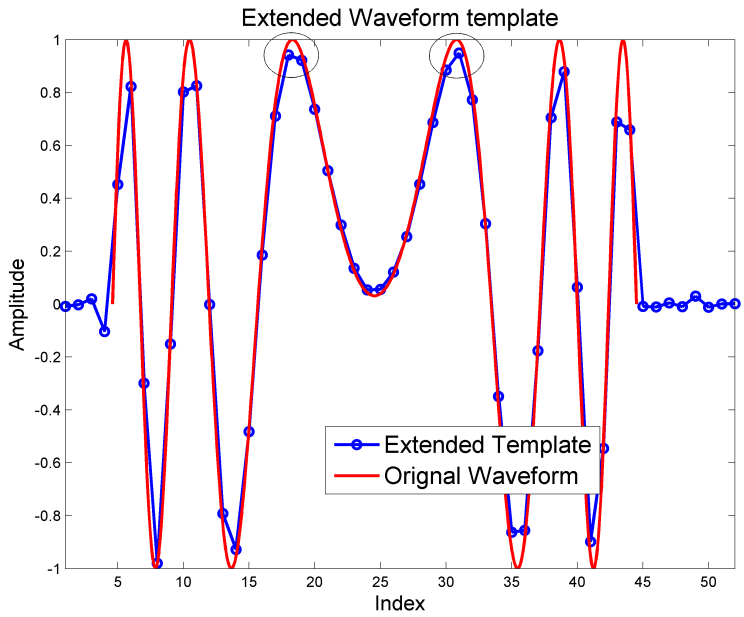

Figure 4.21: HIWRAP extended template and the original LFM signal. Bandwidth=1 MHz, Pulse width=20 μs, Sampling rate=2 MHz

field. The raw data are all oversampled by a factor of 5. So, for 70 μs pulse width, the number of the waveform samples is 350, which takes excessive computational power to process. A 2∼3 downsampling rate is adopted for more efficient data processing and better range resolution. As discussed in the previous section, RMMSE is a super-resolution algorithm, but to gain more resolution, certain trade off has to be made, such as SNR loss and sidelobe degradation. Extensive simulation has been made to determine the best sampling rate for RMMSE algorithm. The best result is obtained by setting the downsampling rate to 2, which corresponds to an actual oversampling rate of $5/2 = 2.5$. Unless otherwise specified, all the data processed by RMMSE are downsampled by 2.

The data of PX1000 radar can be generally divided into two types: hard targets and weather. We will present one hard-target scenario and two weather scenarios, where the details about waveforms and target features are listed in Table.4.9. The

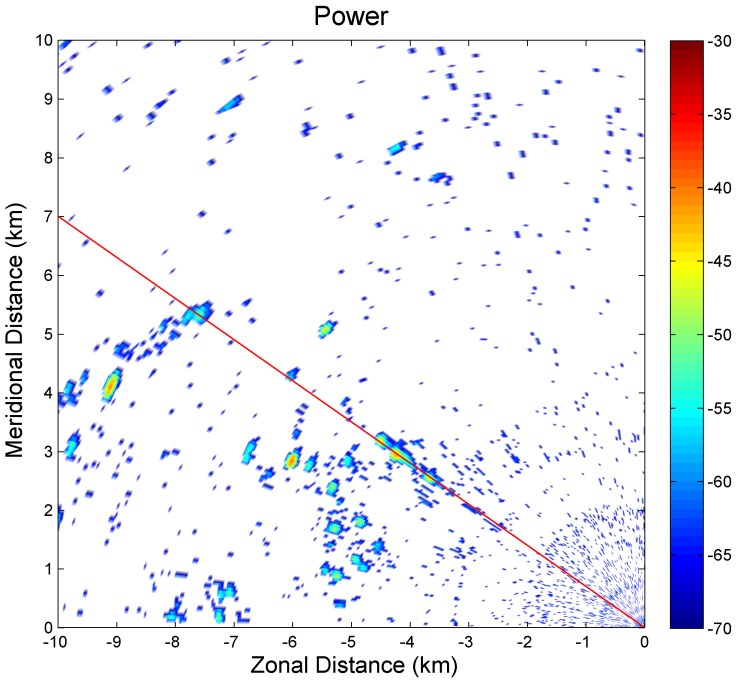

(a)

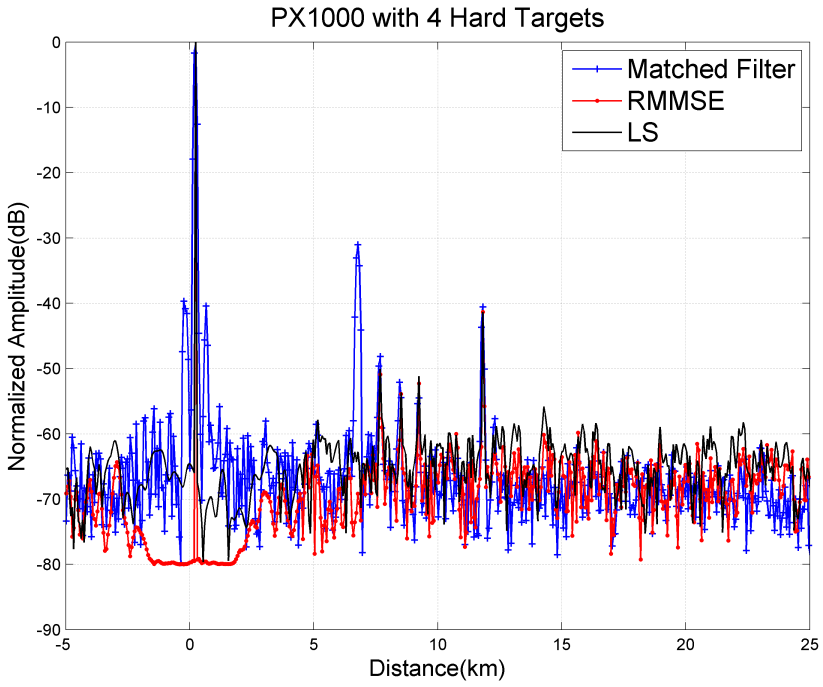

(b)

Figure 4.22: PX1000 data with hard targets presented. Processed by MF, RMMSE and LF for comparison. (a) PPI Scan generated by MF, (b) Pulse compression comparison

Scenario	Waveform	Target Feature	Figure
Hard target	Windowed LFM	Bulidings and towers	4.22
Weather	Windowed LFM	Squall line, >15 km	4.23
	Nonlinear FM	Scattered weather, 10∼15 km	4.24

Table 4.9: PX1000 experiment scenario description

hard targets include buildings, mobile communication tower, water tower, etc. The data processed by MF can be used as a baseline result. Fig. 4.22 presents a hard-target scenario, where Fig. 4.22(a) shows the PPI scan processed by MF. The red line indicates the LOS (line of sight). Clearly, there are 4 strong point targets. They are believed to be the buildings in the local area. Fig. 4.22(b) shows the results of different algorithms. For the hard-targets, there are three different processing results in similar range profiles. The differences are more significant at the direct-coupling response, which shows some artifacts at about 3 km. The sidelobe levels for MF are higher for the direct-coupling response while they are at similar levels for the interested targets, due to the low-sidelobe of the Kaiser-windowed LFM waveforms used in this experiment. The close-to-peak sidelobe of RMMSE can reach up to -80 dB. LS algorithm has slightly increased noise floor.

For weather observations, there are two scenarios available. The weather field of Case #1 is presented in Fig. 4.23(a). The waveform used is a windowed LFM signal. Squall line signature appears about 15 km from the radar. The PPI scan shows the result obtained with MF algorithm. To better compare the performance of different algorithms, a LOS cut is taken at 20°, as indicated in Fig. 4.23(a). Fig. 4.23(b) shows the comparison result. RMMSE has the best sidelobe mitigation and lowest noise floor, whereas LS suffers from additional uncertain sidelobe and noise problem. MF has good performance overall, but the close-to-peak sidelobe is limited to about -40 dB.

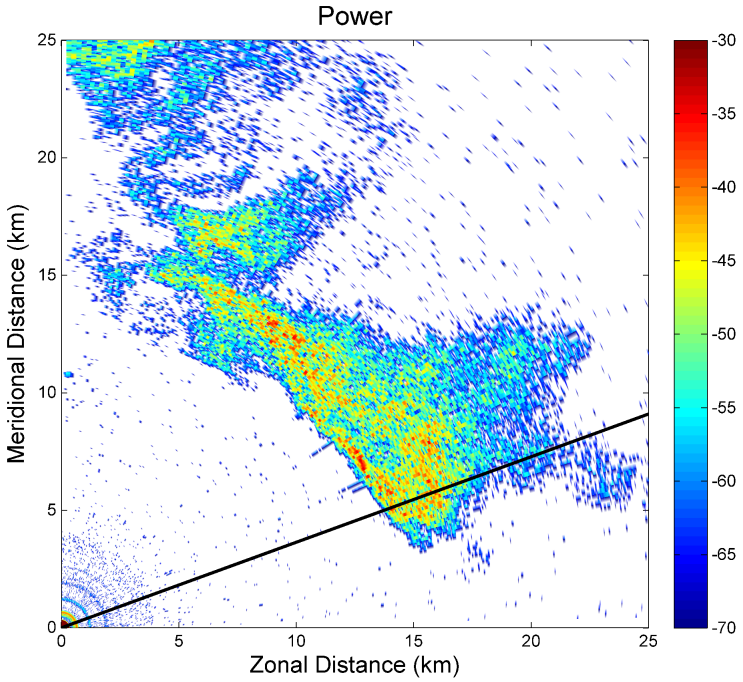

(a)

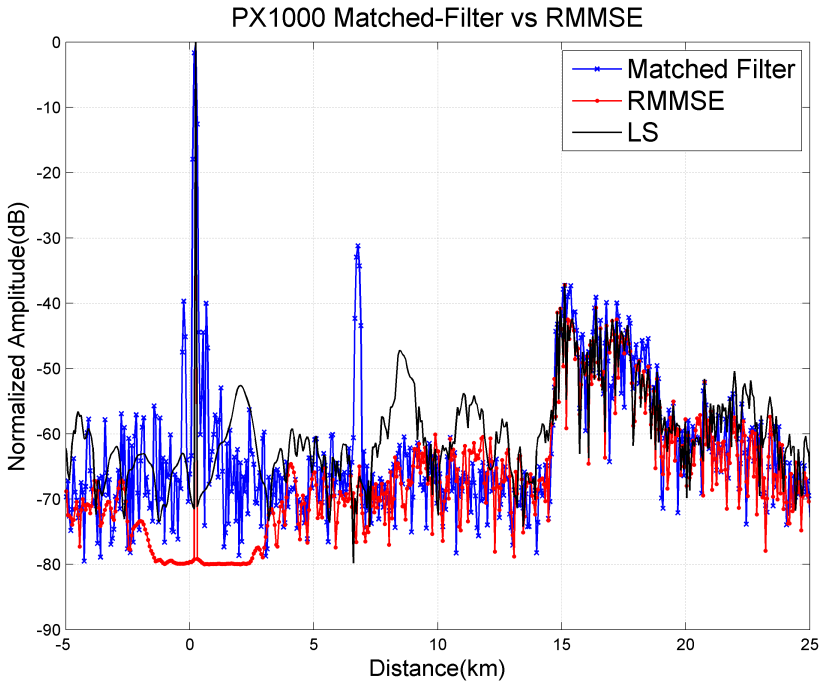

(b)

Figure 4.23: PX1000 data with weather targets presented - Case #1. Processed by MF, RMMSE and LF for comparison. (a) PPI Scan generated by MF, (b) Pulse compression comparison

Fig. 4.24(a) presents another weather scenario. The waveform used is a nonlinear FM signal. As expected, significant sidelobes appear within 10 km from the radar. Our interested LOS is 290°. Fig. 4.24(b) shows the comparison of algorithms. Apparently, RMMSE is the best in terms of sidelobe and noise floor level. MF suffers from the strong sidelobes resulting from the downsampling. The noise floor for LS is degraded significantly.

Fig. 4.25 presents the PPI scan results generated by RMMSE, MF and LS separately. Fig. 4.25(a) is the original pulse compression result by MF without any downsampling. This can be used as a general reference for performance evaluation. Fig. 4.25(b) is the RMMSE result. It removes the strong sidelobe in Fig. 4.25(a), while the weather signature is preserved. Fig. 4.25(c) has sidelobe defect caused by downsampling. Fig. 4.25(d) indicates LS suffers from the waveform template sensitivity issue.

In summary, we have studied several scenarios of practical observation data where weather/hard targets are presented, however, the above experiments are just demonstrative examples of applying adaptive PC algorithms to PX1000 data, we are expecting more cases to be studied and more data to be analyzed to achieve comprehensive analysis and performance evaluations of these processing techniques.

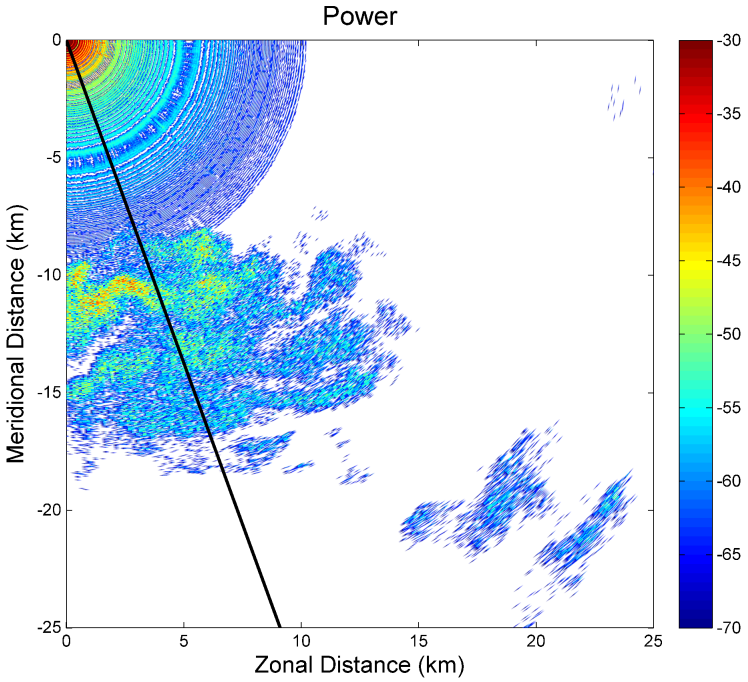

(a)

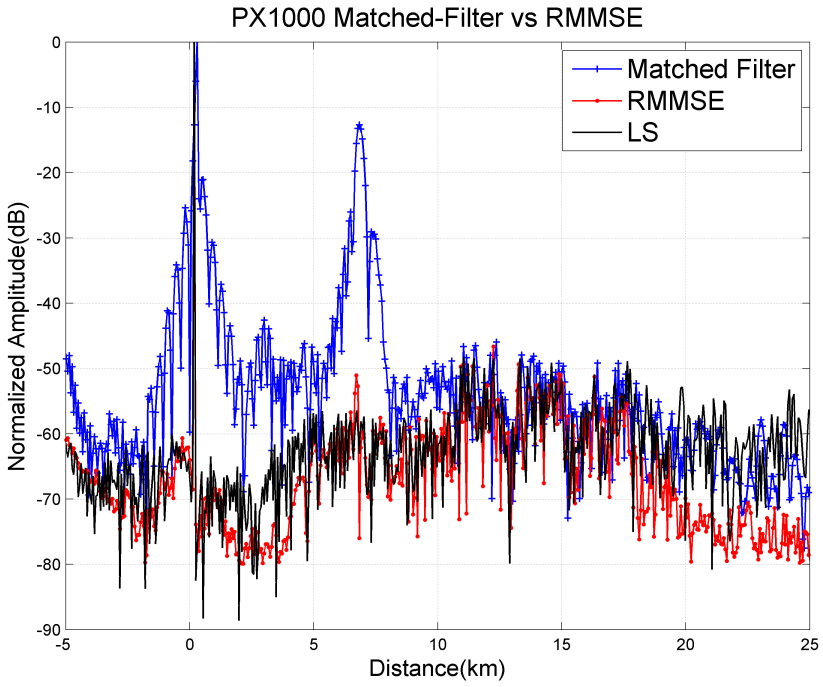

(b)

Figure 4.24: PX1000 data with weather targets presented - Case #2. Processed by MF, RMMSE and LF for comparison. (a) PPI Scan generated by MF, (b) Pulse compression comparison

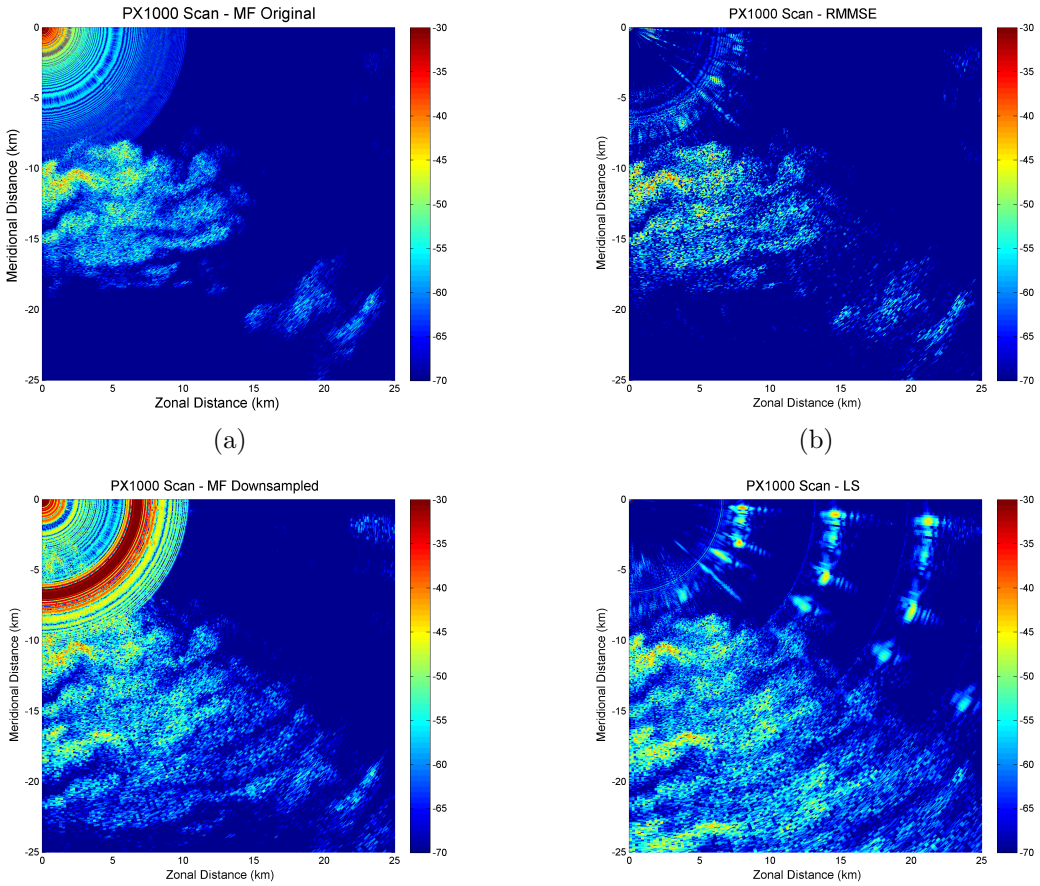

Figure 4.25: PX1000 PPI Scan Comparison. (a) PX1000 PPI Scan by MF , (b) PX1000 PPI Scan by RMMSE , (c) PX1000 PPI Scan by MF downsampled ,(d) PX1000 PPI Scan by LS

Chapter 5

Adaptive Joint Radar Transceiver Optimization

In the previous chapters, the adaptive pulse compression algorithm RMMSE is demonstrated to have better performance than traditional MF and LS algorithms. Although RMMSE is less sensitive to waveform template inaccuracy than other algorithms, it does show some degradation, due to the mismatched waveform template. Multiple factors contribute to the transmit signal distortion, such as PA saturation and drooping effect, AD/DA distortion, RF impedance mismatch, phase and amplitude imbalance, etc. Among all kinds of distortions, Power Amplifier(PA) non-linearity plays an important role. PA is the major source of signal distortion and spurious signal generation, harmonics and inter-modulation products (Schreurs and O'Droma 2009). Phase distortion and long-term memory effect of PA can further deteriorate the signal waveform (Ku and Kenney (2003);Ai et al. (2007)). Further, it accounts for the majority of power consumption in the RF chain. The linearization of PA is still an active research topic nowadays. Fig. 5.1 shows that the imperfection of waveform has great influence on sidelobe suppression performance in PX1000 radar (Kurdzo et al. 2013). The degradation of the range sidelobe is about 20 dB for this case.

Traditionally, PA can be linearized through the Digital Predistorter (Aschbacher et al. (2004); Ding et al. (2007)), which cascades with the signal generator before PA. However, DPD (Digital Pre-Distortion) requires significantly amount of computational power. In addition, the PA is not the only source of signal distortion. RF

receiver chain can introduce distortion too. In this chapter, a joint transmitter and receiver optimization scheme is proposed. It first captures and models the distortions of the entire transmit and receiver chain, then the constructed distortion model is utilized to recover the original (un-distorted) waveform in the receiver. The adaptive sidelobe mitigation algorithm RMMSE calculates the receiver output based on this recovered waveform. The iterative process of sidelobe mitigation is referred to as Joint Transmitter and Receiver Optimization (JTRO). A significant distinction between JTRO and the DPD is all the adaptive learning and estimation are done in the receiver.

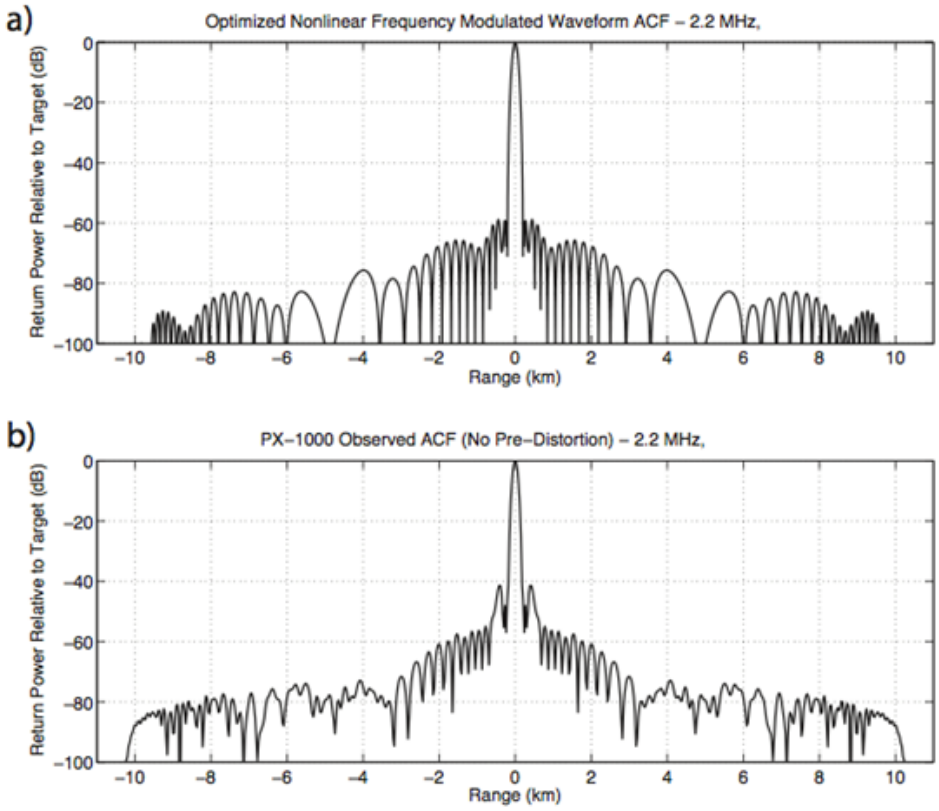

Figure 5.1: Degradation of sidelobe suppression performance caused by distortion.(a) Optimized sidelobe, (b) Distorted sidelobe. (Kurdzo et al. 2013)

5.1 Nonlinear Transceiver Models

There are a large variety of nonlinear models (Arce 2004). The application-based behavioral models are what we concern about. Such models can characterize the system non-linearity without knowing the detailed hardware-level structures. In general, AM-AM and AM-PM conversions are the basis for defining a behavioral model. AM-AM and AM-PM represent Amplitude-to-Amplitude and Amplitude-to-Phase, respectively. The concept of AM-AM and AM-PM has been used for many years because of its generally easier computational implementation, relative efficiency in system simulations and acceptable level of accuracy in many situations (Jeruchim et al. (2000); Schreurs and O'Droma (2009)). The system dominant distortion effects, such as inter-modulations and memory effect are mostly due to the PA non-linearity. It necessitates the understanding of the commonly-used PA models. A system-level behavioral model of an RF nonlinear PA can be described mathematically by a static nonlinear relation between the input and output signals, i.e. $x(t)$ and $y(t)$ by

$$y(t) = G \cdot x(t) \tag{5.1}$$

where G is the instantaneous gain of the nonlinear PA. If the signal is narrow-band (a valid assumption for most radar systems), then the RF input and output may be represented by its base-band equivalents $\tilde{x}(t)$ and $\tilde{y}(t)$ by

$$x(t) = Re[\tilde{x}(t)e^{j\omega_0 t}] \text{ and } \mathrm{y}(t) = Re[\tilde{y}(t)e^{j\omega_0 t}] \tag{5.2}$$

$\tilde{x}(t)$ and $\tilde{y}(t)$ are also referred to the complex-envelop input and output signals. ω_0 is the carrier radian frequency. The phaser form of the input signal $x(t)$ can be written as

$$x(t) = r(t) \cdot cos[\omega_0 t + \phi(t)] = Re[\tilde{x}(t)e^{j\omega_0 t}] \tag{5.3}$$

where $r(t)$ and $\phi(t)$ are the general envelop amplitude and phase components of the input signal respectively, and

$$\tilde{x}(t) = r(t) \cdot e^{j\phi(t)} \tag{5.4}$$

The PA output in Eq. (5.1) will include the desired signal plus harmonics and inter-modulations (IMPs). In practical radars, the out-of-band harmonics and inter-modulation are readily identified and removed by BPFs (band-pass filter). The goal of RF chain design is to transmit and receive, without further distortion, the part of $y(t)$ output signal that is located in the same band as the input $x(t)$ (Schreurs and O'Droma 2009). Thus, the output $y(t)$ can be expressed as

$$y(t) = g(r(t), \omega_0) \cdot cos[\omega_0 t + \phi(t) + \Phi(r(t), \omega_0)] \tag{5.5}$$

where the nonlinear envelop characteristics are $g(r(t), \omega_0)$ and $\Phi(r(t), \omega_0)$. g and Φ represent the AM-AM and AM-PM modulation conversion. If the signal is narrow-band (i.e. the signal bandwidth is much smaller than carrier radian frequency ω_0), then the dependent term ω_0 for g and Φ can be dropped. Fig. 5.2 shows the AM/AM and AM/PM conversion plots for a typical RF transmitter. The data are collected by a practical Ku-band radar.

5.1.1 Typical Nonlinear Behavioral Models

AM-AM and AM-PM model are used to characterize the nonlinear behavior of the system or device in general. Specific mathematical models have been developed used to assist the characterization and analysis of non-linearity.

- ***Volterra series***. In the pass-band, a nonlinear power amplifier with memory can be approximated by the Volterra series,

$$y_n(t) = \int_{-\infty}^{+\infty} \cdots \int_{-\infty}^{+\infty} \int_{-\infty}^{+\infty} h_n(\tau_1, \cdots, \tau_n) \prod_{p=1}^{n} x(t - \tau_p) d\tau_p \tag{5.6}$$

  where the impulse response $h_n(\tau_1, \cdots, \tau_n)$ is called nth-order Volterra kernel (Alper 1965). It represents a nonlinear system response with nonlinear memory effect. Volterra series is the most important tool for nonlinear system modeling and characterization (Fakhouri (1980); Ewen and Weiner (1980); Glentis et al. (1999)).

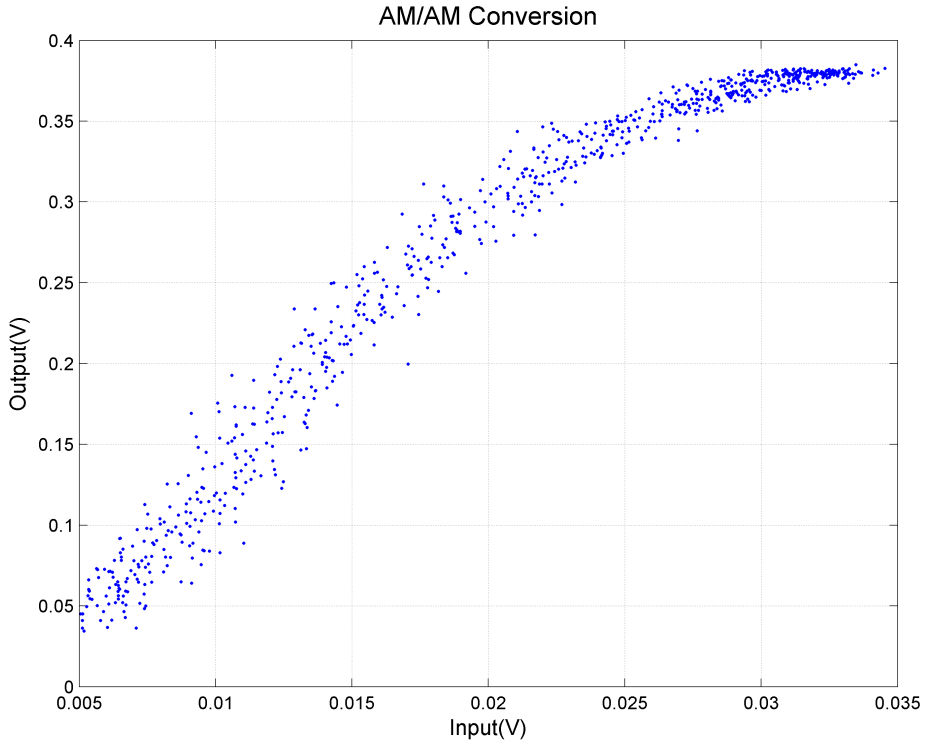

(a)

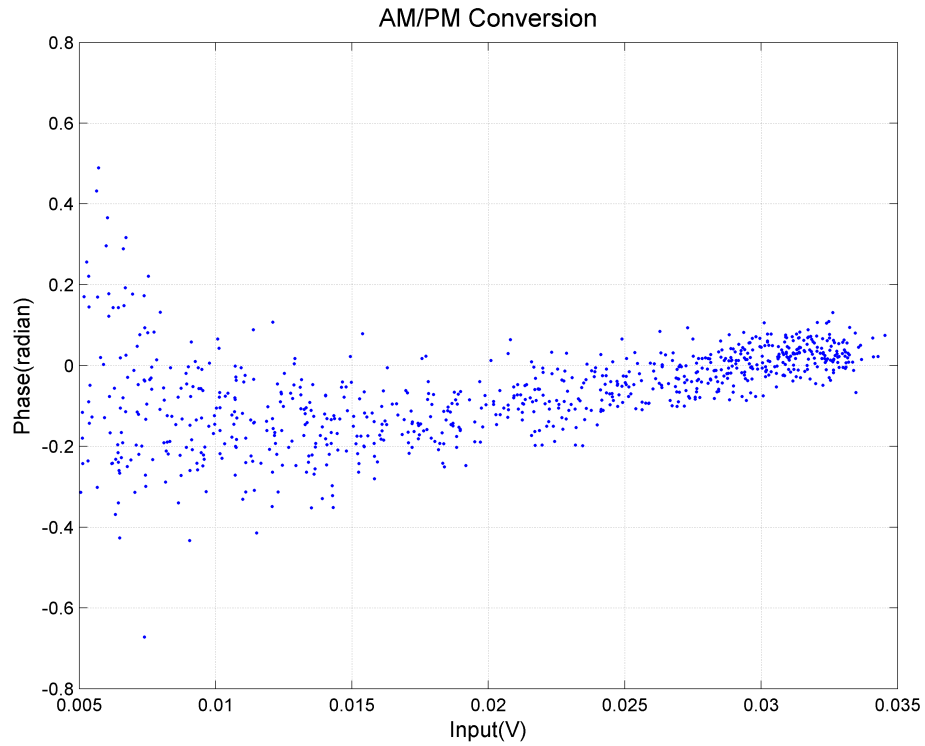

(b)

Figure 5.2: Nonlinear conversion curves. (a) AM-AM, (b) AM-PM

- ***Complex power series***. A general form for an Kth-order power series memoryless model representing the instantaneous RF output as a polynomial expansion of the instant RF input is expressed as (Gutierrez et al. (2000); Gard et al. (1999); Heutmaker et al. (1996))

$$y(t) = \sum_{\substack{k=1 \\ k\ odd}}^{K} b_k \cdot x(t)|x(t)|^{k-1} \tag{5.7}$$

  b_k are complex-valued coefficients. Only odd-order coefficients are considered in that the out-of-band harmonics and IMPs are ignored.

- ***Hammerstein-Wiener model***. The most frequently used configuration for nonlinear system with LTI (linear time-invariant) dynamic behavior is the finite nonlinear ARMA (auto-regressive moving-average) representation (Chrisikos et al. 1998). The system non-linearity is assumed to be static, which can be represented by a power series or polynomial model. The linear memory subsystem can be represented by the linear FIR (finite impulse response) filter. These types of nonlinear dynamic system configuration are also known as Hammerstein-Wiener model (Rugh (1981); Pan and Cheng (2011)). It can approximate most of the nonlinear behavior of PAs with good accuracy. Fig. 5.3 shows the model structure. The Hammerstein model is a memoryless nonlinearity followed by a LTI system. The Wiener model is a LTI system followed by a static nonlinear model. The Hammerstein model can be expressed by

$$z(n) = \sum_{\substack{k=1 \\ k\ odd}}^{K} b_k \cdot x(n)|x(n)|^{k-1} \tag{5.8}$$

$$y(n) = \sum_{l=0}^{L-1} c_l \cdot z(n-l) \tag{5.9}$$

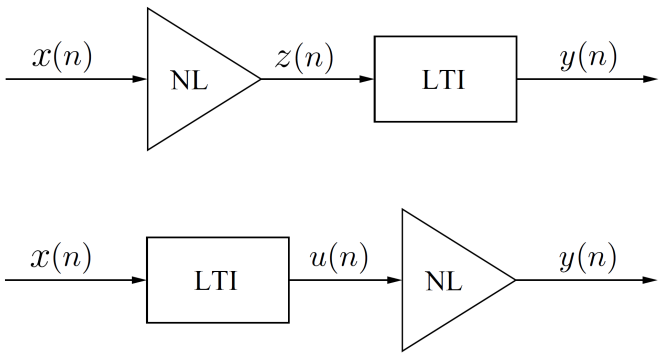

Figure 5.3: Two-box models: Hammerstein and Wiener models

where b_k are the coefficients for the memoryless non-linearity and c_l are the impulse response values of the LTI system. Substitution of Eq. (5.8) into Eq. (5.9) leads to

$$y(n) = \sum_{l=0}^{L-1} c_l \cdot \sum_{\substack{k=1 \\ k\ odd}}^{K} b_k \cdot x(n-l)|x(n-l)|^{k-1} \tag{5.10}$$

Eq. (5.10) will be adopted to analyze the impact of nonlinear distortion on the performance of LS algorithm later.

- ***Saleh model***. Saleh model (Saleh 1981) tries to approximate AM-AM and AM-PM envelop characteristics. This model has been applied to both TWT (traveling-wave tube) and SSPA (Solid-State PA). The polar Saleh model can be written as

$$P(r) = \frac{\alpha_p r}{1+\beta_p r^2} \quad , \quad Q(r) = \frac{\alpha_q r^3}{(1+\beta_q r^2)^2} \tag{5.11}$$

Fig. 5.4 demonstrates the Saleh modeling result of a high-power Ku-band PA module: 83050A. The measurement is done by an Agilent PNA E8364B. The frequency dependence of the response is also shown. Fig. 5.4(a) indicates that this PA has a small amplitude memory distortion effect. The phase memory effect appears when PA is driven into saturation mode according to Fig. 5.4(b).

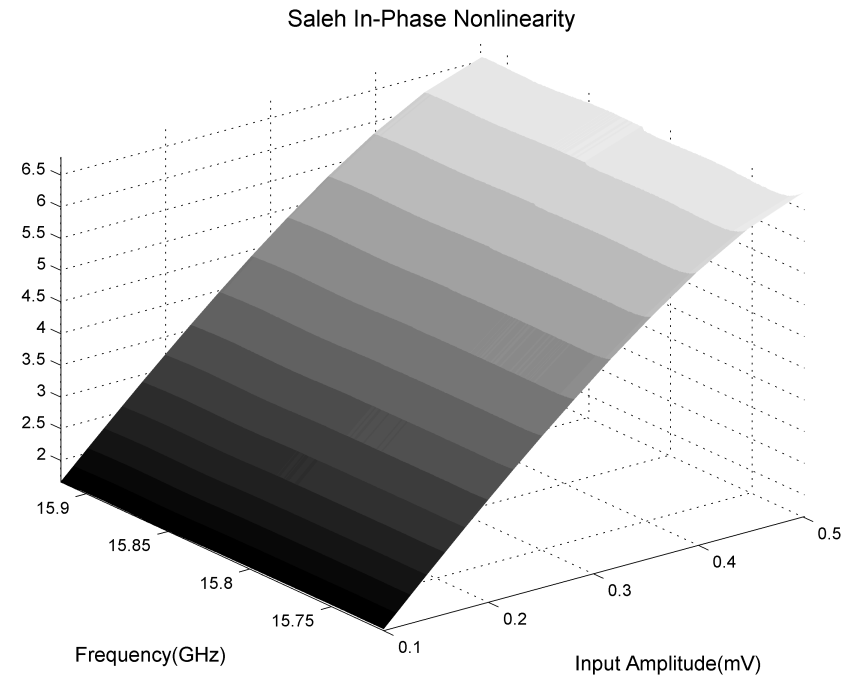

(a)

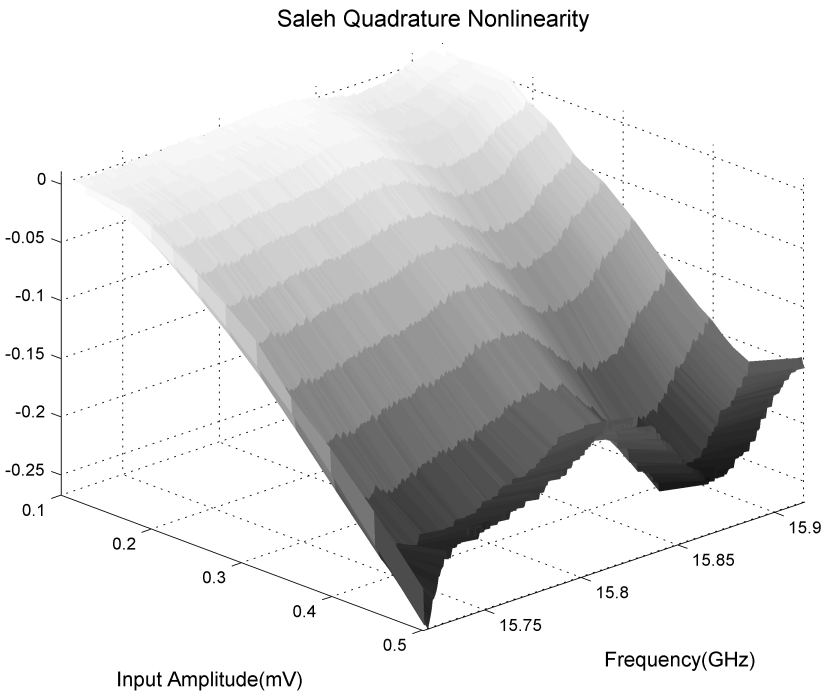

(b)

Figure 5.4: Measured Saleh models for Ku-band 83050A amplifier: (a) In-phase non-linearity, (b) Quadrature non-linearity

5.1.2 The Impact of Nonlinear Distortion

5.1.2.1 Impact on Matched-Filter Response

The nonlinear distortion has serious impacts on the sidelobe suppression performance of matched filters, especially for applications requiring good sensitivities. Fig. 5.5 demonstrates the nonlinear distortion impact on the sidelobe performance. A LFM waveform is firstly designed to meet the -70 dB range sidelobe requirement. Then the signal is fed into the nonlinear system with an AM-AM conversion as shown in Fig. 5.5(a). The input signal power is set to about 3 dB above P1dB compression point. This simulation configuration is close to a typical SSPA operation. Fig. 5.5(b) plots the matched-filter outputs for both the original waveform and the distorted one. From this simulation, we can see that a 4 dB gain compression in saturation region can degrade the sidelobe performance by upto 35 dB.

5.1.2.2 Impact of Nonlinear Distortion on Performance of LS Algorithm

RMMSE and LS are both MSE-type algorithms in a sense that they both attempt to minimize the MSE of certain cost function. Although LS is inferior to RMMSE in terms of practical performance of sidelobe suppression and noise immunity, LS is an important analytical tool, as it usually provides a performance baseline to be compared to other adaptive techniques, such as RMMSE. Therefore, by observing the impact of transceiver non-linearity on LS algorithm, we can obtain some clues of how such non-linearities affect the performance of other algorithms. Assume a memory polynomial model for the nonlinear distortion as

$$y[k] = \phi(\mathbf{x}) = \sum_{p=1}^{P} \sum_{q=0}^{Q} c_{p,q} \cdot x[k-q] \cdot |x[k-q]|^{p-1} \tag{5.12}$$

The original waveform for LS is $\mathbf{s} = [s_0, s_1, \cdots, s_{N-1}]^T$. The distorted waveform $\bar{\mathbf{s}} = [\bar{s}_0, \bar{s}_1, \cdots, \bar{s}_{N-1}]^T$ with

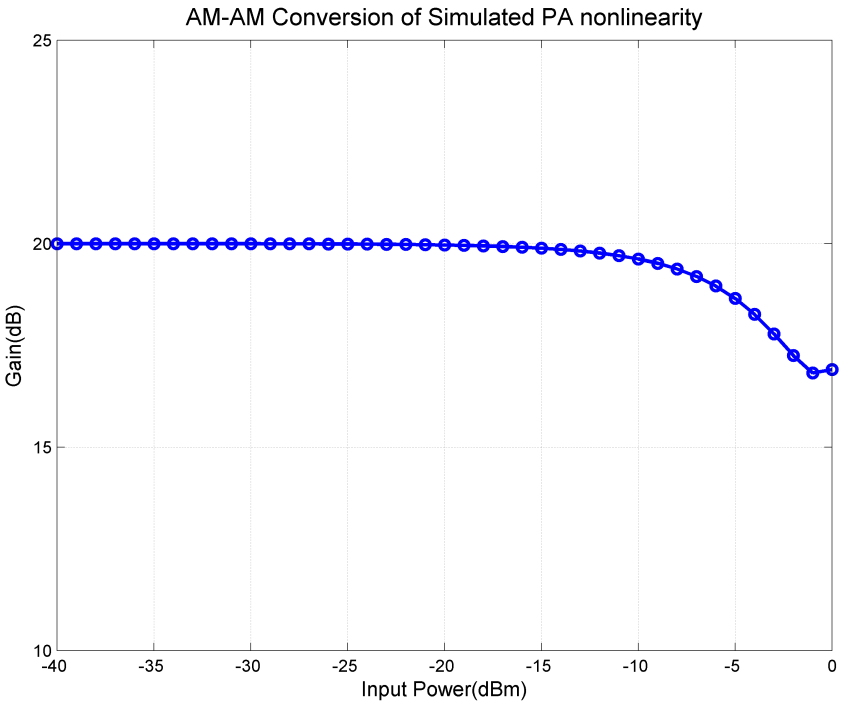

(a)

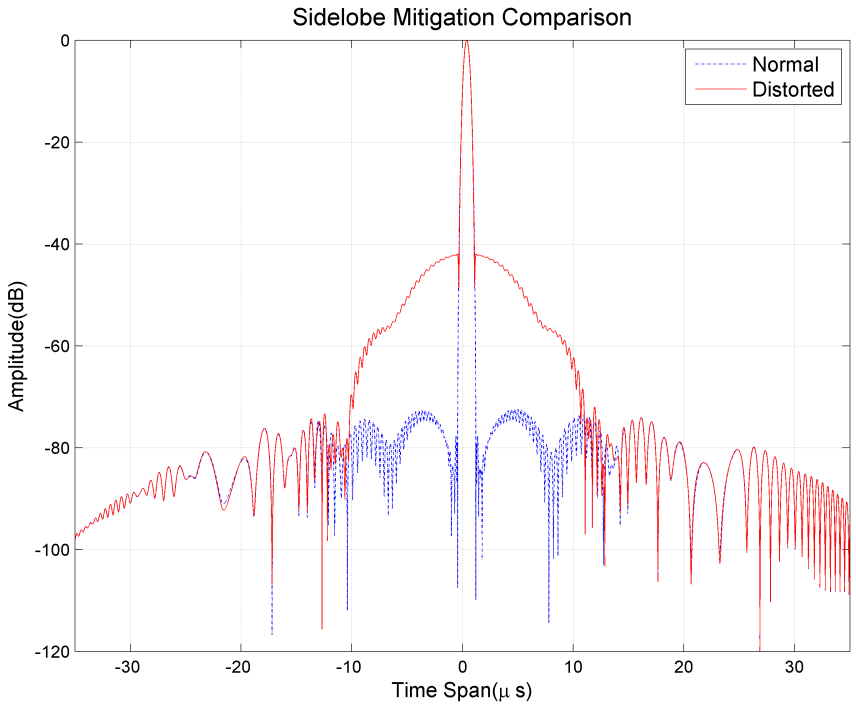

(b)

Figure 5.5: The Impact of Nonlinear Distortion. (a) AM-AM curve of the simulated PA non-linearity, (b) sidelobe mitigation comparison

$$\bar{s}_k = \phi(\mathbf{s}) = \sum_{p=1}^{P}\sum_{q=0}^{Q} c_{p,q} \cdot s_{k-q} \cdot |s_{k-q}|^{p-1} \Rightarrow \bar{\mathbf{s}} = \sum_{p=1}^{P}\sum_{q=0}^{Q} c_{p,q} \cdot \mathbf{s}_{-q} \cdot |\mathbf{s}_{-q}|^{\circ(p-1)} \quad (5.13)$$

where $(\cdot)^{\circ(p-1)}$ denotes the matrix element-wise power operation. $\mathbf{s}_{-q}$ is defined as

$$\mathbf{s}_{-\mathbf{q}} = [\underbrace{0, 0, \cdots, 0}_{q}, s_0, s_1, \cdots, s_{N-1-q}]^T \quad (5.14)$$

Further, take out the linear term:

$$\bar{\mathbf{s}} = \underbrace{c_{1,0} \cdot \mathbf{s}}_{\text{linear static}} + \underbrace{\sum_{q=1}^{Q} c_{1,q} \cdot \mathbf{s}_{-q} + \sum_{p=3}^{P}\sum_{q=0}^{Q} c_{p,q} \cdot \mathbf{s}_{-q} \cdot |\mathbf{s}_{-q}|^{\circ(p-1)}}_{\text{nonlinear dynamic}} \quad (5.15)$$

where $\mathbf{s}_{-q} \cdot |\mathbf{s}_{-q}|^{\circ(p-1)}$ is the nonlinear model basis functions. Eq. (5.15) is a powerful analytical equation. The similar nonlinear equations can be obtained by simply replacing $\mathbf{s}_{-q} \cdot |\mathbf{s}_{-q}|^{\circ(p-1)}$ in Eq. (5.15) with other nonlinear cores such as Volterra or Wiener series. Then the distorted waveform can be divided into two parts: linear and nonlinear terms with

$$\bar{\mathbf{s}} = g \cdot \mathbf{s} + \epsilon \cdot \mathbf{e} \quad (5.16)$$

in which $g = c_{1,0}$. ϵ is defined as a nonlinear coefficient vector related to $c_{p,q}$. $\mathbf{e}$ denotes the nonlinear basis vector related to $\mathbf{s}_{-q} \cdot |\mathbf{s}_{-q}|^{\circ(p-1)}$. It is noticed that the nonlinear coefficient vector ϵ is usually very small compared to the linear static gain g . When it comes to the LS algorithm, the Eq. (5.15) is further extended to a matrix form:

$$\bar{S} = g \cdot S + \epsilon \cdot E \quad (5.17)$$

with

$$S = \begin{bmatrix} s_0 & 0 & 0 \\ \vdots & s_0 & 0 \\ s_{N-1} & \vdots & s_0 \\ 0 & s_{N-1} & \vdots \\ 0 & 0 & s_{N-1} \end{bmatrix} = \begin{bmatrix} \mathbf{s} & 0 & \cdots & 0 \\ 0 & \mathbf{s} & \cdots & 0 \\ 0 & 0 & \ddots & \vdots \\ 0 & 0 & \cdots & \mathbf{s} \end{bmatrix} \text{ and } \bar{S} = \begin{bmatrix} \bar{\mathbf{s}} & 0 & \cdots & 0 \\ 0 & \bar{\mathbf{s}} & \cdots & 0 \\ 0 & 0 & \ddots & \vdots \\ 0 & 0 & \cdots & \bar{\mathbf{s}} \end{bmatrix}$$

Recall from Chapter 4, the received signal model is simply $Y = S \cdot X$ with X being defined as the ground truth impulse response matrix. The LS estimate of X is $\hat{X}_{LS} = (S^H S)^{-1} S^H Y$ (Lewis et al. 2006) without any signal distortion. When the distorted signal $\bar{\mathbf{s}}$ is considered, the received signal model becomes $\bar{Y} = \bar{S} \cdot X$. The corresponding LS estimate becomes $\hat{X}_{LS} = (\bar{S}^H \bar{S})^{-1} \bar{S}^H \bar{Y}$. Accurate estimate is obtained since the waveform $\bar{S}$ and the receive signal $\bar{Y}$ are matched. However, without knowing the distortion the actual LS estimate is expressed as $\hat{X}'_{LS} = (S^H S)^{-1} S^H \bar{Y}$. Estimate is biased due to the mismatch between S and $\bar{Y}$. After plugging in Eq. (5.17),

$$\hat{X}'_{LS} = [(\frac{\bar{S}}{g} - \frac{\epsilon}{g}E)^H (\frac{\bar{S}}{g} - \frac{\epsilon}{g}E)]^{-1} (\frac{\bar{S}}{g} - \frac{\epsilon}{g}E)^H \bar{Y} \tag{5.18}$$

With further manipulation and approximation (higher-order error terms are ignored),

$$\hat{X}'_{LS} \approx g\big[\hat{X}_{LS} - g\epsilon(\bar{S}^T\bar{S})^{-1}E^T \underbrace{(\bar{Y} - \bar{S} \cdot \hat{X}_{LS})}_{\text{distortion error}} + g\epsilon(\bar{S}^T\bar{S})^{-1}\bar{S}^T E \cdot \hat{X}_{LS}\big] \tag{5.19}$$

In Eq. (5.19), the distorted estimate $\hat{X}'_{LS}$ has a linear relationship with $\hat{X}_{LS}$. In addition, the second term is caused by distorted estimation. It is relatively small compared to the third term. Thus,

$$\hat{X}'_{LS} \approx g\big[\hat{X}_{LS} + \epsilon C \cdot \hat{X}_{LS}\big] \tag{5.20}$$

with $C = g(\bar{S}^T\bar{S})^{-1}\bar{S}^T E$ being a constant. This analytical model can be populated into another more complicated form. Incorporating Eq. (5.15) into Eq. (5.20),

$$\hat{X}'_{LS} = \underbrace{c_{1,0} \cdot \hat{X}_{LS}}_{\text{linear static}} - c_{1,0}(\bar{S}^T\bar{S})^{-1}\bar{S}^T \cdot \underbrace{\left[\sum_{q=1}^{Q} c_{1,q} \cdot S_{-q} + \sum_{p=3}^{P}\sum_{q=0}^{Q} c_{p,q} \cdot S_{-q} \cdot |S_{-q}|^{\circ(p-1)}\right]}_{\text{nonlinear dynamic}} \cdot \hat{X}_{LS} \tag{5.21}$$

where

$$S_{-q} = \begin{bmatrix} \bar{\mathbf{s}}_{-q} & 0 & \cdots & 0 \\ 0 & \bar{\mathbf{s}}_{-q} & \cdots & 0 \\ 0 & 0 & \ddots & \vdots \\ 0 & 0 & \cdots & \bar{\mathbf{s}}_{-q} \end{bmatrix} \text{ and } S_{-0} = \bar{S}$$

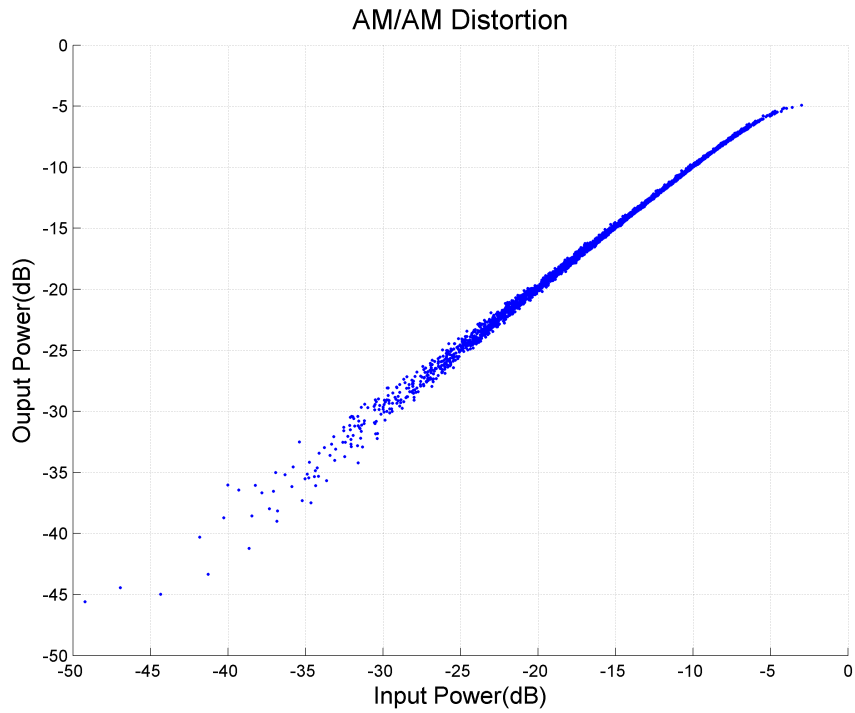

(a)

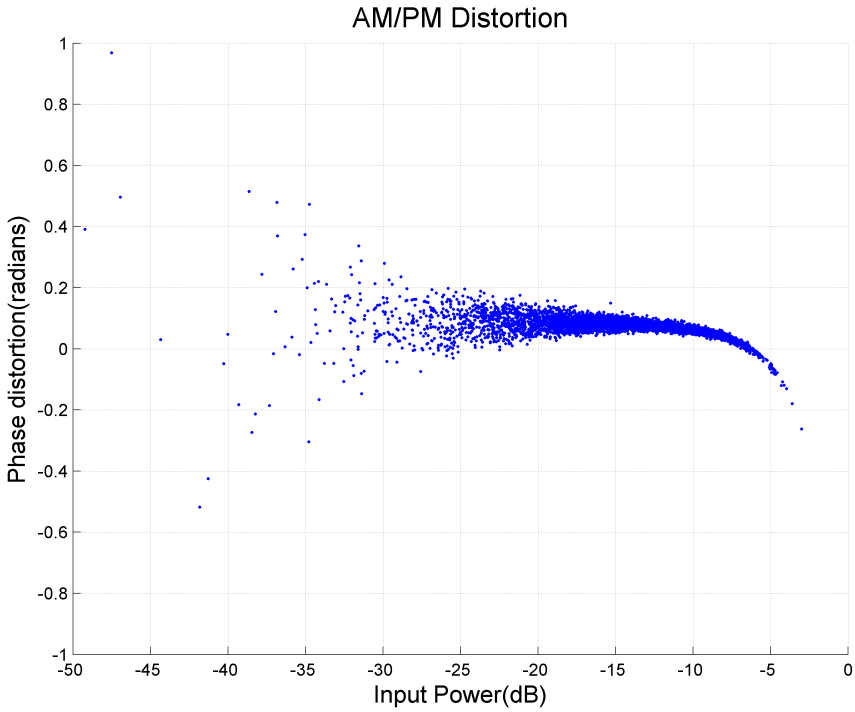

(b)

Figure 5.6: The simulated PA nonlinear distortion. (a) AM-AM, (b) AM-PM

A simulation is implemented to study the degradation of sidelobe level caused by nonlinear distortion. Three point targets with SNR = 100, 80 and 60 dB are setup without receiver noise (The noise level is set to -100 dB such that the noise impact can be ignored). The PA has AM/AM and AM/PM characteristics as shown in Fig. 5.6 (which is typical and used in previous literatures such as (Schreurs and O'Droma 2009)), and the estimation results by MF, LS and RMMSE are presented in Fig. 5.7. Because there is no noise presented in the simulation, the ground truth is the ideal impulse response (spike-shape). It is obvious that the presence of distortion greatly increases the noise-floor level for LS, which even overwhelms the weaker target. RMMSE is also suffering from the sidelobe introduced by nonlinear distortion, even though RMMSE result does not show sidelobe degradation far from the target region. The simulation also indicates that RMMSE has better immunity to nonlinear distortion than LS algorithms.

5.2 Kernel Adaptive Filter

A nonlinear adaptive filter called Kernel Adaptive Filter (KAF) is important to the receiver self-learning process. RF systems, especially PAs are complex dynamic systems that combine both memory effects and nonlinear phenomena. The traditional nonlinear model with linear memory effect such as Wiener-Hammerstein models can predict nonlinear effect efficiently. However, their capability of capturing memory effect is limited. The choice of the nonlinear behavior model is highly problem dependent, and there are local minima during training. The popular nonlinear models with nonlinear memory effect such as the time-delay neural network (TDNN) (Lavagetto 1997) and the Volterra series (Alper 1965) can model nonlinear system with strong memory and nonlinear effects. However, they are computationally intensive to implement in practice. The complexity of the Volterra series explodes exponentially as its modeling capacity increases. Also, the non-convex optimization nature of neural

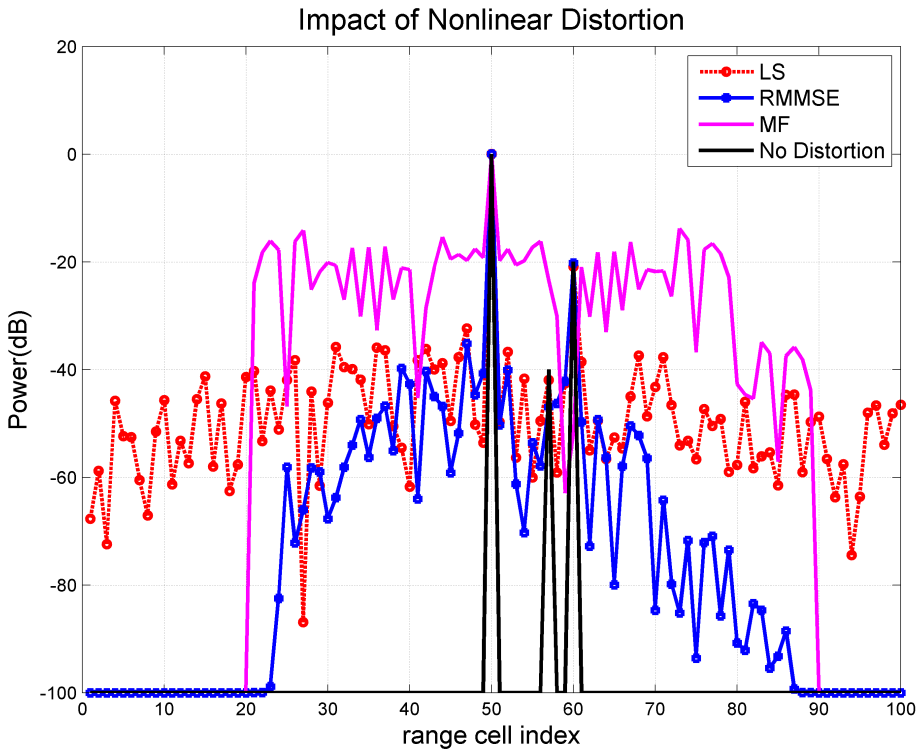

Figure 5.7: Nonlinear distortion impact on pulse compression algorithms

network hinders their widespread use in online applications. Trade-offs have to be made between computational efficiency and modeling accuracy.

Recently, the concept of Kernel Adaptive Filter is proposed by (Liu et al. 2009). The *Kernel method* is a powerful non-parametric modeling tool. It attempts to transform the input data into a high-dimensional feature space via a reproducing kernel such that the inner product operation in the feature space can be computed efficiently through the kernel mapping (Liu et al. 2010). It maintains the nonlinear modeling capability of kernel while improving the computational efficiency.

5.2.1 RKHS and KLMS

RKHS (reproducing kernel Hilbert space) is a *complete* inner product space, in which the *reproducing kernel space* is defined (Liu et al. 2010). The analytic power of RKHS

is expressed in an important theorem called the Mercer theorem (Burges 1998), which states that any reproducing kernel $\kappa(\mathbf{u}, \mathbf{u}')$ can be expanded in Eq. (5.22):

$$\kappa(\mathbf{u}, \mathbf{u}') = \sum_{i=1}^{\infty} \lambda_i \phi_i(\mathbf{u}) \phi_i(\mathbf{u}') \tag{5.22}$$

where λ_i and ϕ_i are the eigenvalues and eigenfunctions, respectively. By setting

$$\phi(\mathbf{u}) = [\sqrt{\lambda_1}\phi_1(\mathbf{u}),\ \sqrt{\lambda_2}\phi_2(\mathbf{u}),\ \cdots] \tag{5.23}$$

It is easy to obtain

$$\kappa(\mathbf{u}, \mathbf{u}') = \phi(\mathbf{u}) \cdot \phi(\mathbf{u}')^T \tag{5.24}$$

In the literature of non-parametric regression, it is known that the Gaussian kernel has the universal approximating capability and creates a RKHS. Another choice of kernel function is polynomial kernels. (Franz and Scholkopf 2006) shows that Volterra and Wiener series can be represented implicitly as elements of a RKHS by utilizing polynomial kernels. The Gaussian and Polynomial kernels are expressed in Eq. (5.25) and Eq. (5.26):

$$\kappa(\mathbf{u}, \mathbf{u}') = exp(-\frac{||\mathbf{u} - \mathbf{u}'||^{\mathbf{2}}}{h^2}) \tag{5.25}$$

$$\kappa(\mathbf{u}, \mathbf{u}') = (1 + \mathbf{u}'\mathbf{u})^p = \sum_{n=0}^{p} \binom{p}{n} (\mathbf{u}'\mathbf{u})^n \tag{5.26}$$

where h is defined as *kernel bandwidth*. p is the order of polynomials.

Least-mean-square(LMS) is a widely used stochastic gradient algorithm. The most important features of LMS are the simplicity and robustness, because LMS is model-independent and also free of matrix inversion operation. The LMS core can be summarized as:

$$e(i) = d(i) - \omega^T(i-1)\mathbf{u}(i) \tag{5.27}$$

$$\omega(i) = \omega(i-1) + \eta e(i)\mathbf{u}(i) \tag{5.28}$$

where $\mathbf{u}(i)$ is the input at ith iteration. $d(i)$ is the desired output. $\omega(i)$ is the weighting coefficient. η defines the learning step length. Replacing $\mathbf{u}(i)$ with high-dimensional feature space mapping function $\phi(\mathbf{u}(i))$, yields

$$e(i) = d(i) - \omega^T(i-1)\phi(i) \tag{5.29}$$

$$\omega(i) = \omega(i-1) + \eta e(i)\phi(i) \tag{5.30}$$

Also, the repeated application of the weight-update Eq. (5.30) through iterations yields:

$$\omega(i) = \eta \sum_{j=1}^{i} e(j)\phi(j) \tag{5.31}$$

Further, apply the "kernel trick" to Eq. (5.31), i.e. multiply both sides of Eq. (5.31) and substitute with Eq. (5.24)

$$\omega(i)^T\phi(\mathbf{u}') = \eta \sum_{j=1}^{i} e(j)\kappa(\mathbf{u}(j), \mathbf{u}') \tag{5.32}$$

Thus, the resulting KLMS core can be expressed as:

$$f_{i-1} = \eta \sum_{j=1}^{i} e(j)\kappa(\mathbf{u}(j), \cdot) \tag{5.33}$$

$$f_{i-1}(\mathbf{u}(i)) = \eta \sum_{j=1}^{i} e(j)\kappa(\mathbf{u}(j), \mathbf{u}(i)) \tag{5.34}$$

$$e(i) = d(i) - f_{i-1}(\mathbf{u}(i)) \tag{5.35}$$

$$f_i = f_{i-1} + \eta e(i)\kappa(\mathbf{u}(i), \cdot) \tag{5.36}$$

where f_i is denoted as the estimate of the input-output nonlinear mapping at time i. (Liu et al. 2008) provides the detailed derivation of KLMS algorithm. In short words, KLMS is the LMS in RKHS. The filtering is done by kernel evaluation. KLMS allocates a new kernel unit for the new training data with input $\mathbf{u}_i$ as the center and $\eta e(i)$ as the coefficient. The coefficients and the centers are stored in memory during training. Fig. 5.8 illustrated the KLMS algorithm flow, where $\mathbf{a} = \eta \cdot \mathbf{e}$, and $\mathbf{a} = [a_1, a_2, \cdots, a_i]^T$,$\mathbf{e} = [e(1), e(2), \cdots, e(i)]^T$.

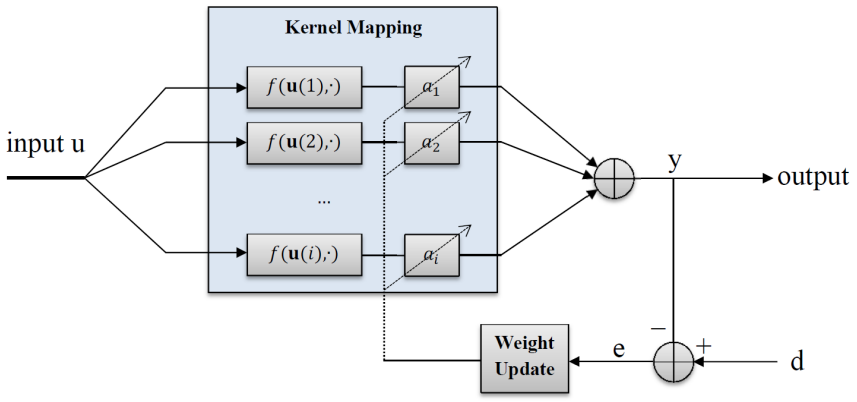

Figure 5.8: KLMS Signal Flow at ith iteration

KLMS has a similar structure as RBF(Radial Basis Function) in neural network (Huang et al. 2005). However, they actually work differently. Table. 5.1 summarizes the difference.

Network	**RBF**	**KLMS**
Weighting	Independent coefficients	Scaled prediction errors
Size	Stable	Growing†
Core	Mostly Gaussian functions	Mercer kernel

†: The size of KLMS grows with the number of training samples

Table 5.1: Comparison between RBF and KLMS network

5.2.2 KLMS Application to Nonlinear Distortion Modeling

We present an example in which KLMS is applied to nonlinear system modelling. The measurement data are taken from the input and output of a RF transmitter system, which includes a PA operating in saturation region. The KLMS is adopted to model the AM/AM and AM/PM conversion of the system. Fig. 5.9 shows the modeling

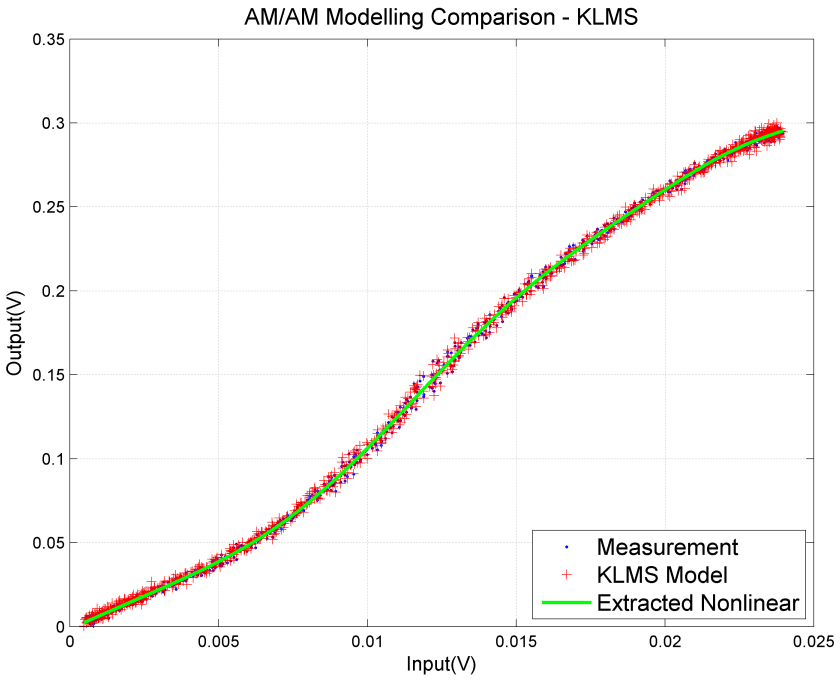

(a)

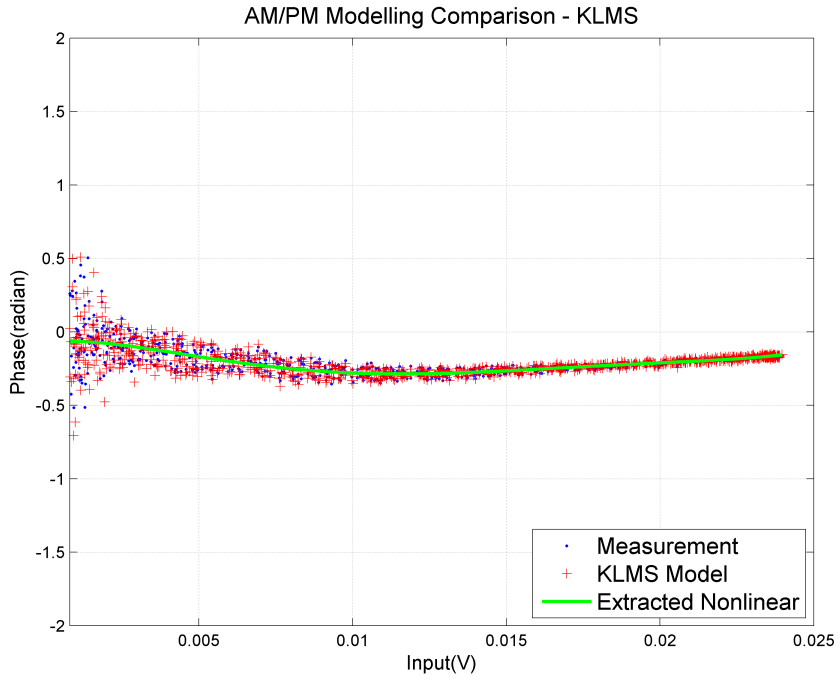

(b)

Figure 5.9: Application of KLMS in nonlinear modeling. (a) Measurement vs Model for AM-AM, (b) Measurement vs Model for AM-PM

results. Fig. 5.10 depicts the MSE (mean-square-error) along with the number of iterations. KLMS demonstrates good convergence in the modeling process.

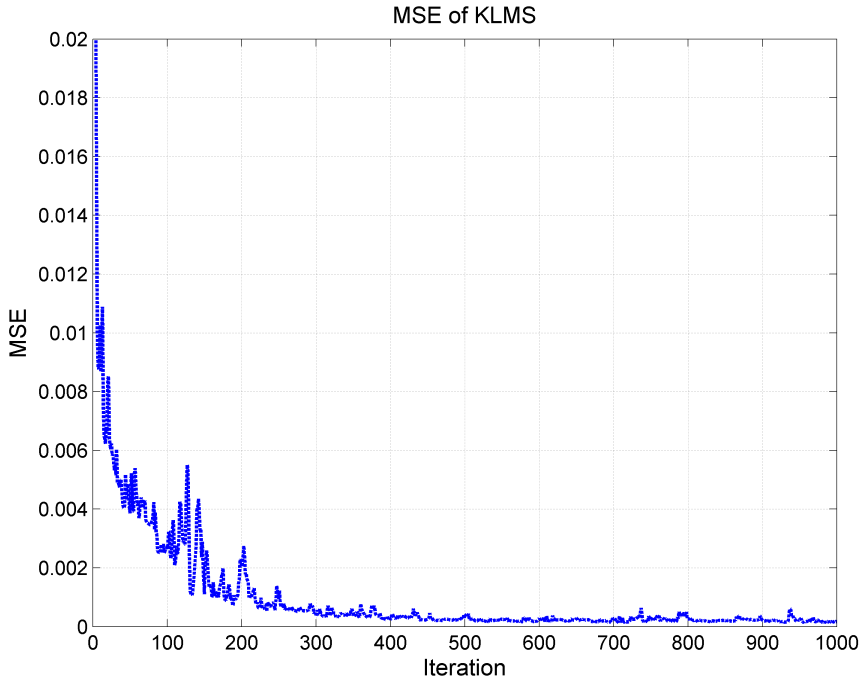

Figure 5.10: Convergence of KLMS modeling in Fig. 5.9

Furthermore, to evaluate the performance of KLMS in recovering the waveform under nonlinear distortion, another simulation with waveform input is conducted. The waveform adopted is a LK-P3 signal with N=60, and the nonlinear distortion is assumed to be the same as in Fig. 5.9.

First, the input waveform **s** is fed into the nonlinear model to get a distorted output **d**. Then **d** is utilized as the regulation for KLMS training. After N iterations, KLMS completes the training, and the network size grows to N. Last, the input **s** is again fed into the "trained" KLMS network and the predicted output waveform is obtained. KLMS network with waveform input is depicted in Fig. 5.11. The simulation result is shown in Fig. 5.12. Fig. 5.12(a) shows the input waveform without any distortion.

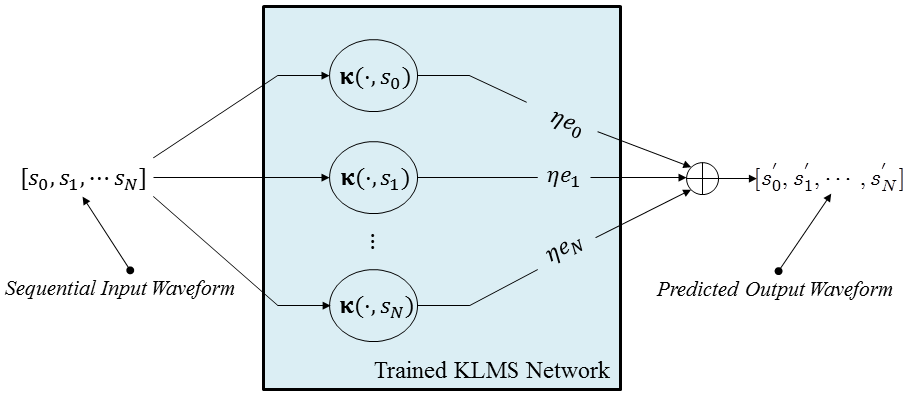

Figure 5.11: KLMS waveform training network

Fig. 5.12(b) is the comparison between the original distorted waveform and KLMS modeled waveform output. There is good correlation between the two output curves.

5.3 Hammerstein-LS Nonlinearity Modeling

Hammerstein model as discussed in Section 1 is a very efficient and accurate nonlinear estimation method. The coefficients for LTI and static nonlinear parts can be calculated iteratively by LS algorithm. (Ding et al. 2007) summarizes the procedure.

To test the performance of Hammerstein-LS algorithm and also the nonlinear response of the Ku band transceiver testbed platform, the measured input and output data of the verification platform are used to train the Hammerstein-LS model. The waveform used in the experiment is a Kaiser-windowed LFM signal with bandwidth $B = 2MHz$, Kaiser $\beta = 6$ and pulse width $T = 20\ \mu s$. Since the waveform itself contains both amplitude modulation (AM) and phase modulation (PM), the AM/AM and AM/PM curves of the system is easily obtained. Fig. 5.13(a) and (b) show AM/AM and AM/PM conversion curves derived from measurement and Hammerstein-LS model. Interestingly, the AM/AM is not consistent with the regular PA AM/AM curve. There is some sort of distortion even with low input power. This

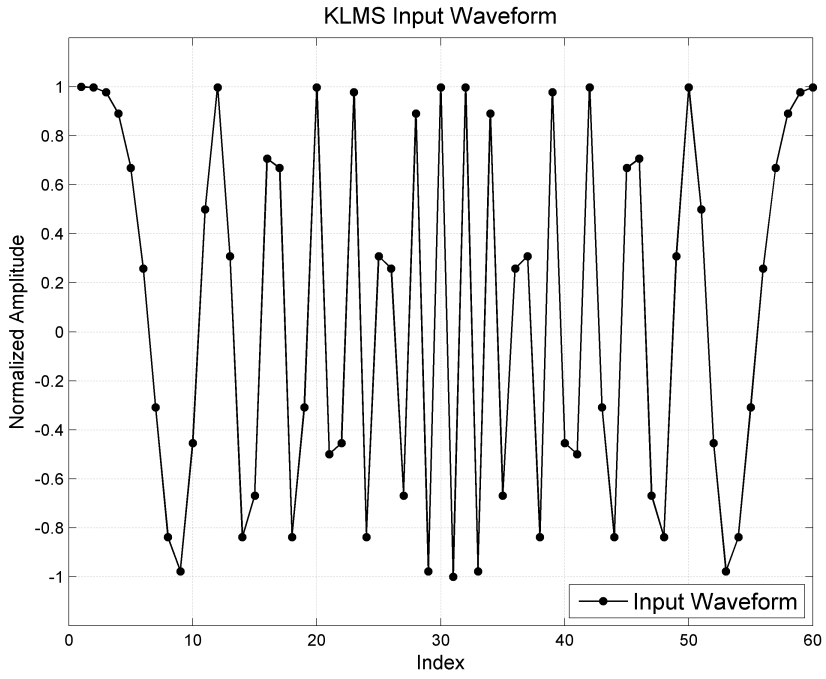

(a)

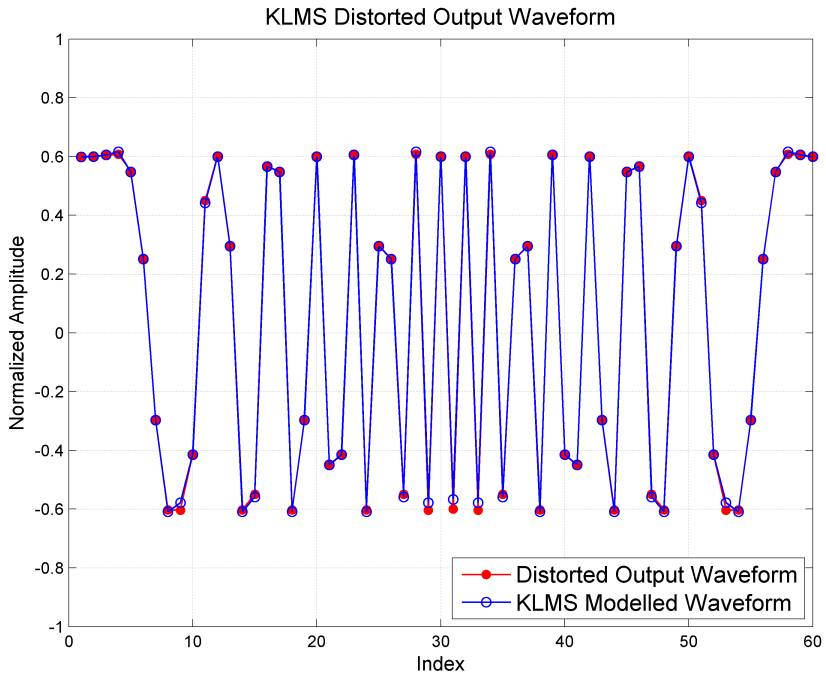

(b)

Figure 5.12: KLMS waveform distortion modeling. (a) Input waveform, (b) Desired output waveform and KLMS modeled result

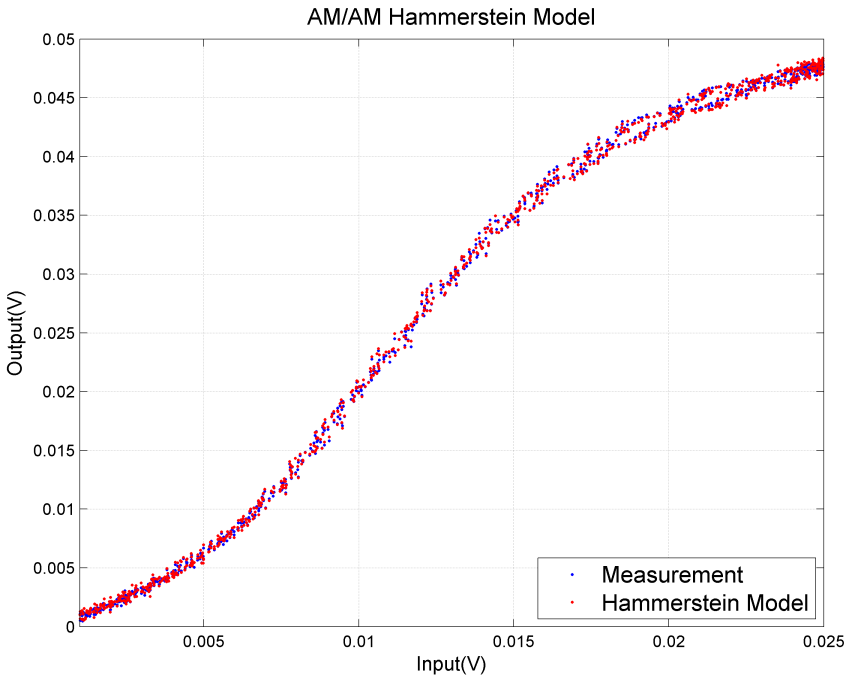

(a)

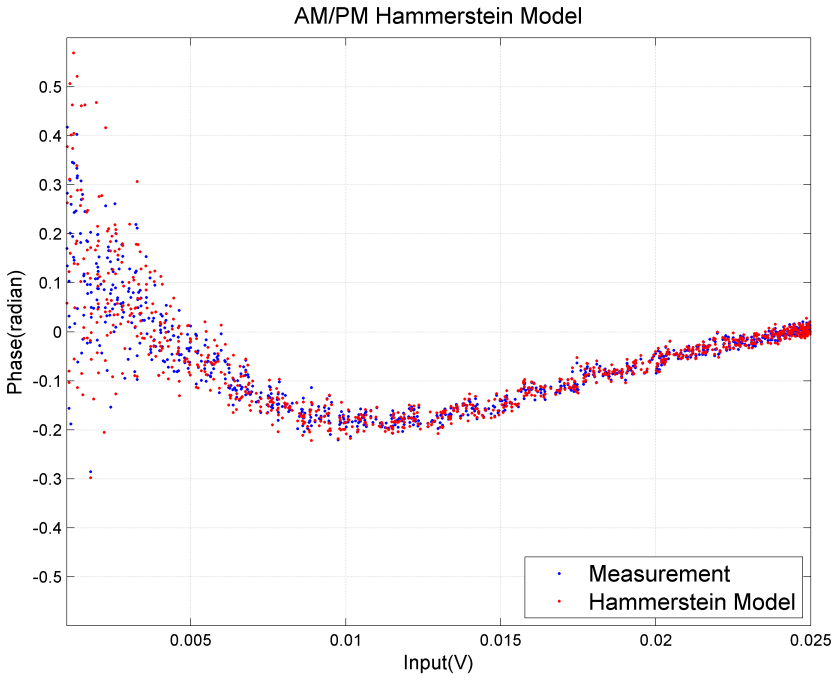

(b)

Figure 5.13: Hammerstein-LS algorithm in nonlinear modeling. (a) AM/AM, (b) AM/PM

is because the nonlinear distortion we try to model include the behavior of the entire transmit and receive chain. The distortion results from not only PA but also some other components such as LNA, mixer, band-pass filter, IQ-demodulator etc. Overall, Hammerstein-LS achieves a nonlinear model very close to the measurement results. Fig. 5.14 is the MSE convergence curve for the Hammerstein-LS training. Usually, 5 iterations are enough to achieve a decent training result. The Hammerstein model will be used as the nonlinear modeling method as shown in the "Adaptive Receiver" block of Fig. 5.18(b).

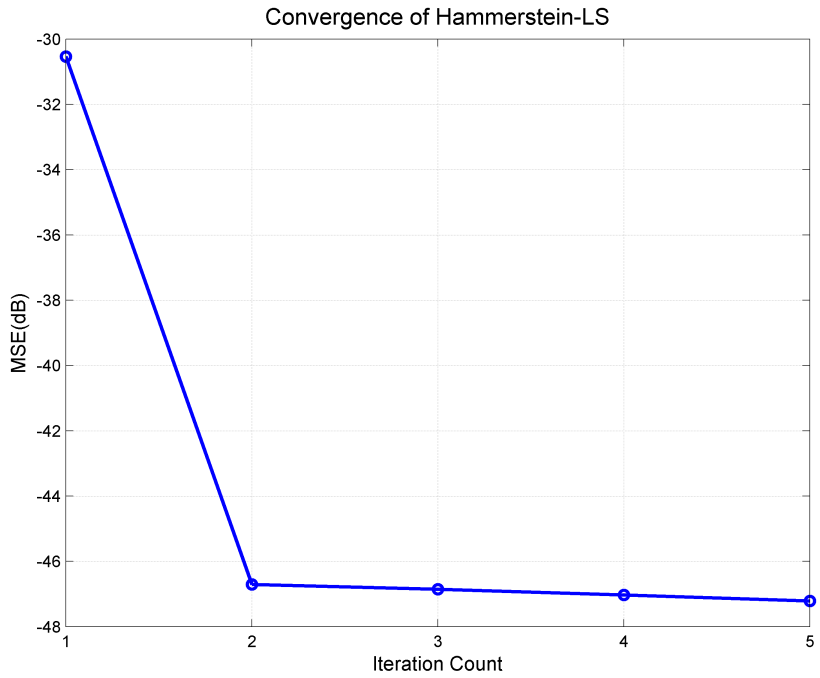

Figure 5.14: MSE Convergence of Hammerstein-LS

5.4 Ku-band Spaceborne Radar Transceiver Testbed

To characterize the performance of various algorithms for sidelobe and nonlinear distortion mitigation, a Ku-band Radar transceiver emulator is built based on COTS (Commercial Off-The-Shelf) components. Fig. 5.15 shows the overall system diagram. The RF section is composed of a two-stage superheterodyne transceiver. The transmit IF signal is up-converted by a 1st-LO at 3 GHz and a 2nd-LO at 10.6 GHz. The resultant RF signal after up-conversion is about 13.6 GHz, which is at Ku-band (12 $\sim$ 18GHz). A GaAs pHEMT PA with a maximum output power about 3 watts is adopted to introduce nonlinear distortion to the transmit signal. To save budget, only one filter (HMC891LP5E, tunable bandwidth and center frequency) is used in frequency conversion chains so the noise floor of the transceiver is a little high, which could limit the visible sidelobe suppression levels (discussed in section 5.5.3). The details about the RF section of the platform is shown in Fig. 5.16(a) and (b). The digital portion of the system consists of an arbitrary waveform generator (AWG), control PC and an FPGA-based baseband receiver. AWG has a sampling rate of 625MS/s with DDS output and 15-bit DAC resolution. It can generate the transmit signal directly at IF (70MHz).

5.5 Adaptive Joint Transceiver Optimization

5.5.1 Options for Transceiver Nonlinearity Mitigation

Traditionally, the nonlinear distortion in the transceiver system is handled by digital predistortion (DPD). DPD technique has been widely used in wireless communication system, where transmission formats such as CDMA (code-division multiple access)

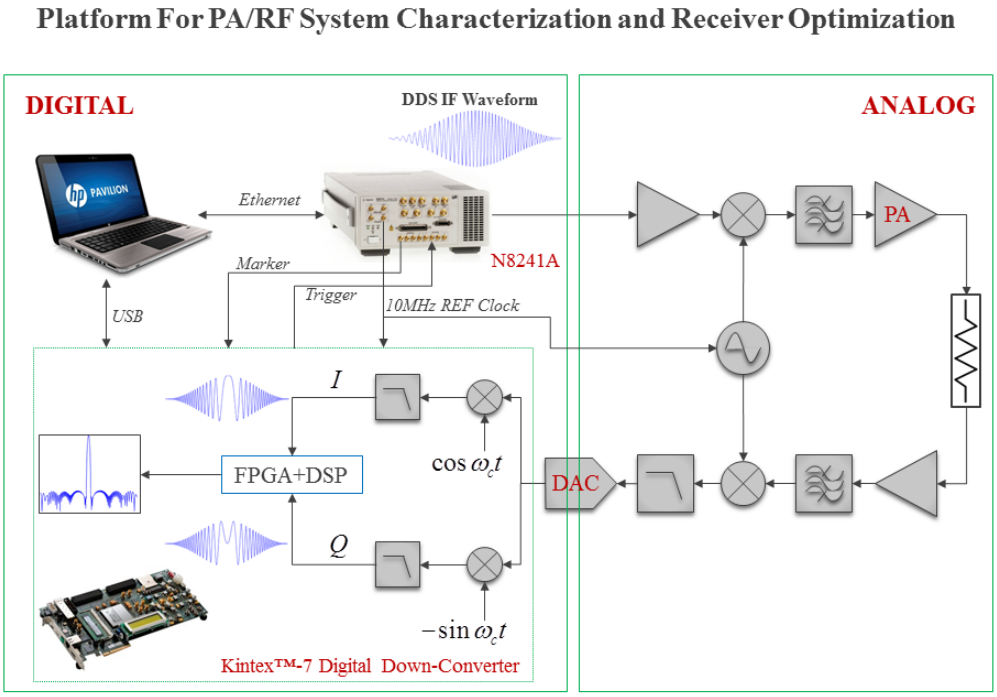

Figure 5.15: Ku-band spaceborne radar transceiver testbed

and OFDM (orthogonal frequency-division multiplexing) are vulnerable to PA nonlinearities (Xiao et al. (1998); O'Droma and Mgebrishvili (2005)). Numerous DPD algorithms have been developed, such as (Ai et al. (2007);Ding et al. (2007);Aschbacher et al. (2004)), just to name a few. Fig. 5.18(a) shows an RF transceiver system basd on predistortion. DPD is a technique used to improve the linearity of radio transmitter. By reducing the distortion created by the transmitter in their nonlinear regions, the transmitted waveform can be made more closer to the original and thus the sidelobe introduced by nonlinear effect can be reduced. DPD utilizes the error signal between the original and distorted waveform to regularize the coefficients in the predistorter. The trained coefficients can be stored as a look-up table (LUT). Then both amplitude and phase of the transmitted waveform can be adjusted according to the LUT. The drawbacks of this configuration are **a**. The transmitter

(a)

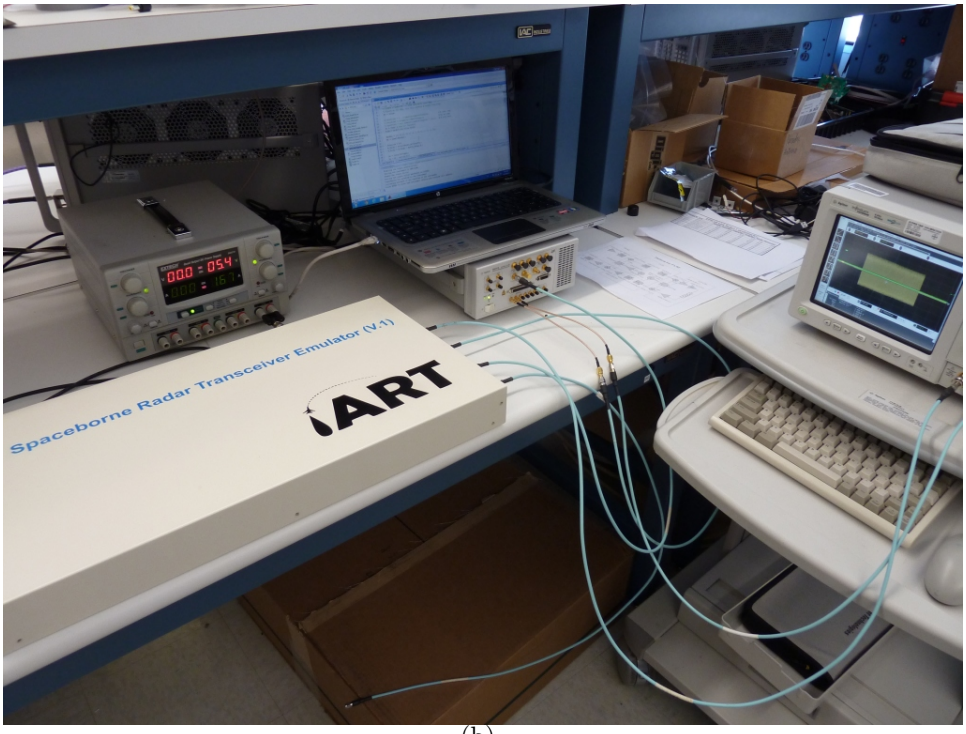

(b)

Figure 5.16: Ku-band Radar Experimental Platform. (a) Experimental transceiver box, (b) Demonstration of data acquisition

DPD is totally independent of the receiver. The sidelobe mitigation performance is highly dependent on the DPD; $\mathbf{b}$. DPD requires excessive computational power and its learning procedure is complicated. A dedicated feedback signal path is required to perform the PA model training.

Another option to suppress the nonlinearity is based on nonlinear channel equalization in communication systems, in which the channel is modeled as the combination of linear and nonlinear components. The optimal bit error rate can be achieved by mitigating the nonlinear distortion via kernel processing (kai Ruan and Zhang 2009). Compared to the idea of DPD, the nonlinearity mitigation is performed in the receiver instead of the transmitter. The major problem for this equalization-based method is that the "channel" is unknown for radar application. This will cause mitigation error in a general.

Both of the two methods discussed above require the inverse modeling of the nonlinear distortion. An alternative may is the forward modeling, in which the distorted waveform is updated and fed-forward to the receiver for pulse compression processing. This will minimize waveform template mismatch between transmitter and receiver.

Fig. 5.7 has already demonstrated the impact of nonlinear distortion on pulse compression sidelobe. To understand how the effects of nonlinear distortion in Fig. 5.7 can be suppressed, a simulation is performed to compare the three options discussed above, i.e. DPD-based, equalization-based and forward-modeling methods. The simulation procedure is simplified based on a 5th-order nonlinear polynomial model : $f(x) = x - 0.1x^3 - 0.05x^5$. All the nonlinear modeling of the three options are trained by Hammerstein-LS algorithm. After the nonlinearity is mitigated or modeled, the resultant waveform and receiving signal are further processed by LS and RMMSE. The target setting is the same as that in Fig. 5.7. The simulation results are presented in Fig. 5.17. Table. 5.2 summarizes the peak sidelobe levels of the 4 plots in Fig. 5.17. Overall, RMMSE has a better immunity to nonlinear distortion than

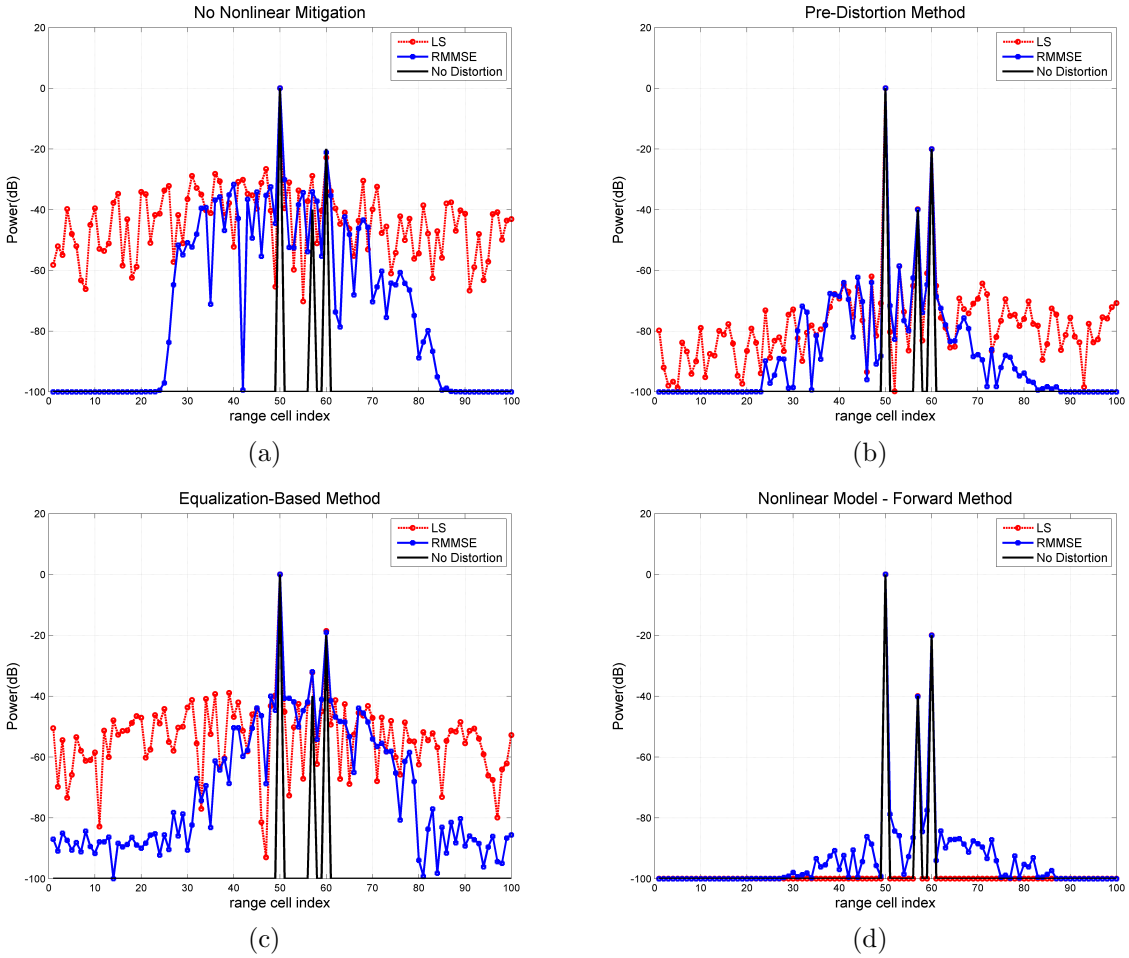

Figure 5.17: Sidelobe comparison after nonlinear mitigation (a) No nonlinear mitigation, (b) DPD-based nonlinear mitigation, (c) Equalization-based nonlinear mitigation, (d) Forward-modeling mitigation

LS, except in Fig. 5.17(d) where LS has no sidelobe at all. Both DPD-based and equalization-based methods suffer from the possible inaccuracy of inverse nonlinear modeling. For equalization-based method, inverse modeling of nonlinear distortion alone is not adequate for sidelobe mitigation in the present of multiple targets. In general, the target structure is not a prior knowledge for radar application, which makes equalization-based method less accurate. In the following sections, we focus on developing a joint optimization scheme based on forward-modeling method.

Fig. 5.17	Mitigation Method	RMMSE Peak Sidelobe
(a)	None	-30 dB
(b)	DPD-based	-58 dB
(c)	Equalization-based	-40 dB
(d)	Forward-modeling	-76 dB

Table 5.2: Sidelobe comparison for different nonlinear mitigation options.

5.5.2 Concept of Joint Transceiver Optimization

To overcome the hardware complexity and improve the overall transceiver linearity, we propose a novel Joint Transmitter and Receiver Optimization (JTRO) scheme based on the forward-method discussed in previous section for sidelobe mitigation and optimized ground truth estimation. Joint transmitter-receiver optimization method has been developed in communication systems with multiple access channels. (Luo et al. 2004) shows that the optimal MMSE transceivers can be obtained by appropriate subcarrier allocation. A general solution for the optimum linear transformation is derived jointly subject to the MMSE criterion in (Jang et al. 1998). It is shown that joint transmitter-receiver optimization outperforms significantly compared to either transmitter optimization or receiver-based techniques alone. In this Chapter, instead of trying to linearize the transmitter by predistorters, the *adaptive receiver* "learns"

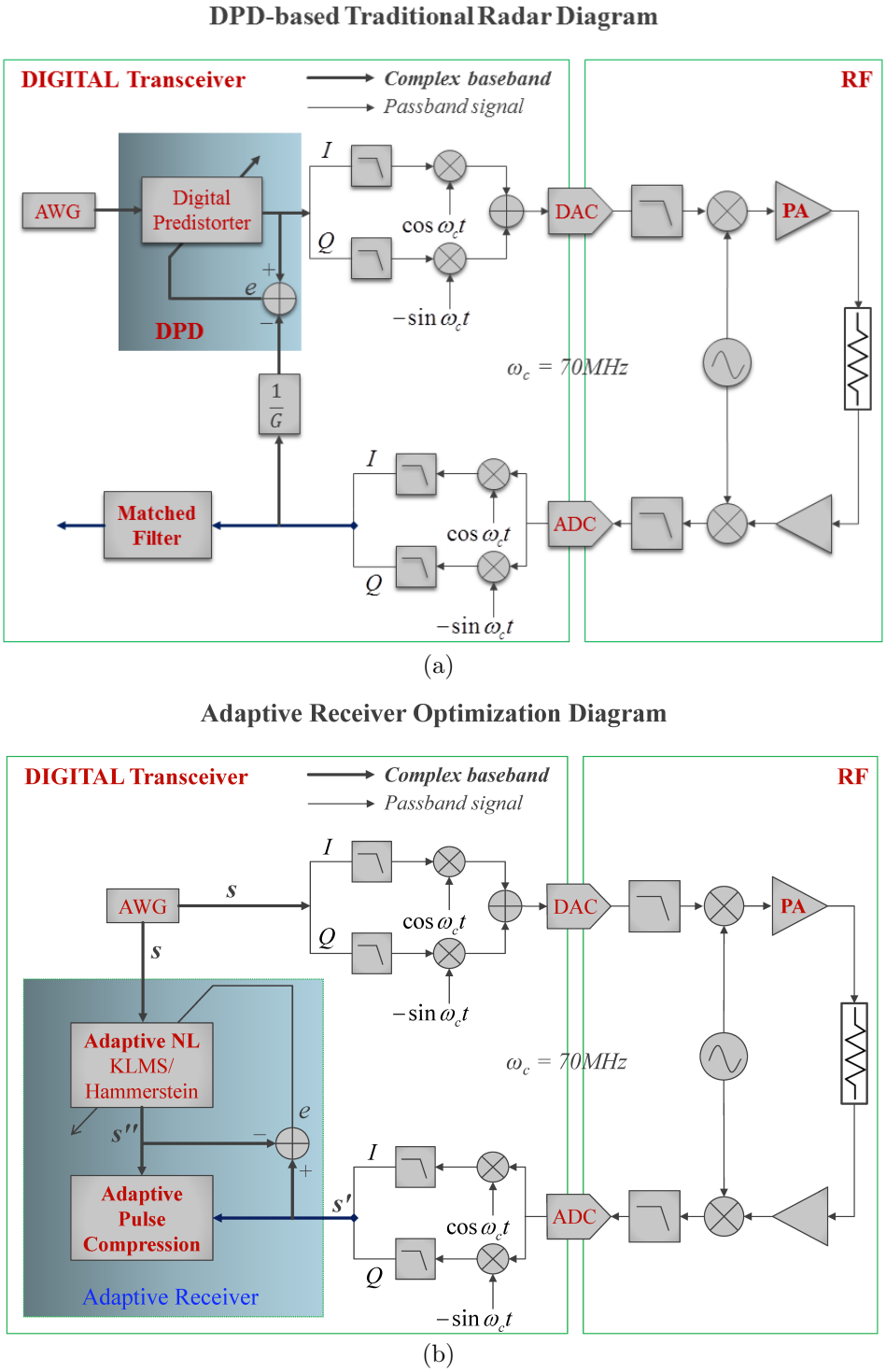

Figure 5.18: Simplified radar transmit/receive architecture. (a) Traditional DPD-based structure, (b) The JTRO scheme based on forward-method

the nonlinear distortion of the entire transmitter/receiver chain and suppresses the sidelobe caused by distortion using adaptive pulse compression. The self-learning and adaptive pulse compression are performed simultaneously in the radar receiver. The joint optimization concept is demonstrated in Fig. 5.18(b). Instead of using a predistorter to linearize the transmitted waveform, the original waveform is directly inserted into the digital receiver. The nonlinear behavior of the transceiver system is approximated by an adaptive nonlinear model. The nonlinear model output is used by RMMSE pulse compression algorithm to achieve optimal sidelobe suppression. The error between the original waveform $\mathbf{s}$ and the distorted waveform $\mathbf{s}'$ is used to accurately capture the nonlinear distortion of the system.

5.5.3 Algorithm Description

The details of the JTRO algorithm can be described as follows: First, the signal with distortion (s') is transmitted with respect to a known ground truth x. This x can be a calibration target or simply a direct coupling signal from transmitter to receiver. Then the RMMSE pulse compression receiver estimates the distorted transmit signal s' by using the known impulse response x. Next, the estimated s' is fed back to the nonlinear model to calculate the model coefficients. The nonlinear model used here is either Hammerstein-LS or KLMS. Last, the system switches into normal operation.

With known x in RMMSE, the signal s' can be estimated by the following methods:

Recall in RMMSE algorithm, there exists the following relationship between $\hat{x}$ and Y (mathematical model):

$$\hat{x} = \omega^H Y \tag{5.37}$$

And the RMMSE adaptive filter coefficient is (at l-th range gate):

$$\omega = \rho \cdot (C + R)^{-1} \cdot s' \tag{5.38}$$

where C is the covariance matrix of the receiving samples and R is the noise covariance matrix:

$$C = \begin{bmatrix} E[y^2(l)] & E[y(l)y(l-1)] & \cdots & E[y(l)y(l-N+1)] \\ E[y(l-1)y(l)] & E[y^2(l-1)] & \cdots & E[y(l-1)y(l-N+1)] \\ \vdots & \vdots & \ddots & \vdots \\ E[y(l-N+1)y(l)] & E[y(l-N+1)y(l-1)] & \cdots & E[y^2(l-N+1)] \end{bmatrix}$$

$$Y = Y(l) = [y(l)\ y(l-1)\ \cdots\ y(l+N-1)]^T$$

Combining Eq. (5.37) and Eq. (5.38) and by solving the under-determined LS problem (Lewis et al. 2006), s' can be derived as

$$s' = \rho^{-1} Y^H (C+R)^{-1} \left[Y^H (C+R)^{-2} Y \right]^{-1} \cdot x \tag{5.39}$$

Eq. (5.37)$\sim$(5.39) also indicate an iterative mechanism. First of all, as the number of receiving samples are usually much larger than that of the waveform s, there will be totally L different Ys. L is the number of range gates. Since x is a calibration target, it usually has a solitary impulse response. Even for multi-target scenario, the impulse response of x can be simply formulated as $x = c_0 s(n-n_0) + c_1 s(n-n_1) + c_2 s(n-n_2) + \cdots$.

The estimated s' from Eq. (5.39) can be re-inserted into Eq. (5.37) and Eq. (5.38) to estimate a new $\hat{x}$ (Eq. (5.37) and Eq. (5.38) actually constitute the core of RMMSE). Then $\hat{x}$ can substitute x as a new calibration target response, so that the whole calibration process reiterates until $||x - \hat{x}|| < \delta$, where δ defines an acceptable MSE error (e.g. 10^{-3}). Fig. 5.19 demonstrates the calibration process. After s' is obtained, the nonlinear distortion is characterized by KLMS or Hammerstein-LS models. The transceiver then switches to the normal operation as shown in Fig. 5.18(b).

5.5.4 Experiment Results

The JTRO validation experiment is conducted using the Ku-band transceiver platform. As mentioned before, the joint optimization algorithm is expected to be

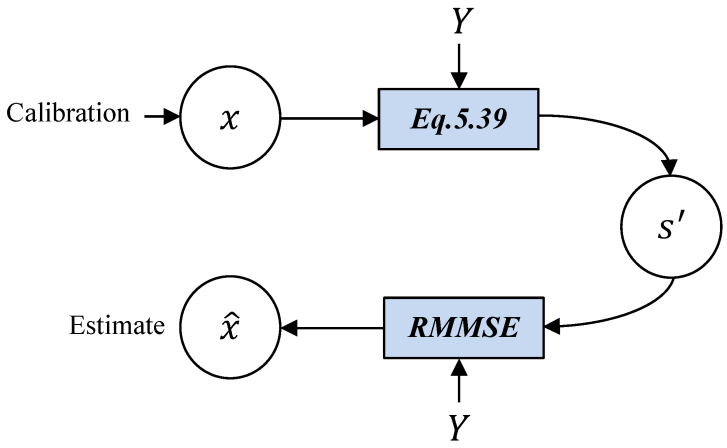

Figure 5.19: Demonstration of JTRO on estimating distorted waveform $\mathbf{s}'$

waveform-independent. In this experiment, a LFM signal with both amplitude and phase modulation is used (Kaiser window with $\alpha = 6$ is applied). Fig. 5.20(a) shows the transmit waveform, including both the inphase and quadrature components. This windowed waveform is mainly used in the experiment Case # 1. Two other scenarios are also considered. Case # 2 uses 13-bit Barker code waveform, and Case # 3 uses 30-bit LKP3 waveform. The reason to use Barker code and LKP3 in the Case 2 and 3 is that Barker code is the most popular binary pseudo-random code for radar waveforms and LKP3 is a special type of poly-phase coding waveform. Since there is no amplitude variation for Barker and LKP3 waveforms, the nonlinear distortion effect is expected to be less significant than LFM. Fig. 5.21(a) and Fig. 5.22(a) show the waveform samples for the Barker and LKP3 codes used in the experiment, respectively.

After tuning the gain of the pre-amplifier, the PA is setup to operate at an input power level of 3 dB above the P1dB (1dB compression point), resulting in strong nonlinear distortion during the transceiver operation. To simplify the experiment setup, the transmitted signal is "looped back" to the receiving chain via a 40 dB

directional coupler. Therefore, the "ground truth" in this case is equivalent to the impulse response of a solitary target (Dirac delta function ideally). Our expectation is to achieve a clean solitary peak (main-lobe) with a minimized range sidelobe level. After collecting the receiving samples, the joint optimization is applied to the data to perform waveform distortion extraction and RMMSE adaptive pulse compression. Two nonlinear models are adopted : Hammerstein-LS and KLMS. The experiment results of three scenarios are shown in Fig. 5.20(b), Fig. 5.21(b) and Fig. 5.22(b), respectively. It is evident that the nonlinear distortion not only has deteriorated the sidelobe level (up to -35 dB in Case# 1), but also widened the main lobe, especially in the proximity of main-lobe. Both nonlinear models with joint optimization can successfully mitigate the sidelobe caused by distortion. In particular, KLMS outperforms Hammerstein-LS in that KLMS can achieve a lower sidelobe. With a ideal solitary target used as a reference, Table. 5.3 lists the performance comparison in term of the MSE metric, which is defined as

$$MSE = ||\hat{x} - x||$$

where x is the impulse response of an idea point target and $\hat{x}$ is the estimated response.

Method	**w/distortion**	**KLMS**	**Hammerstein-LS**
MSE#1	+0.06 dB	-29.45 dB	-20.81 dB
MSE#2	-21.41 dB	-26.30 dB	-22.31 dB
MSE#3	-27.76 dB	-33.84 dB	-31.18 dB

Table 5.3: MSE comparisons of JTRO using KLMS and Hammerstein-LS training.

5.5.5 Discussions

As promising results from JTRO processing have been obtained in section 5.5.3, there are natural questions on what are the optimized sidelobe and noise levels can

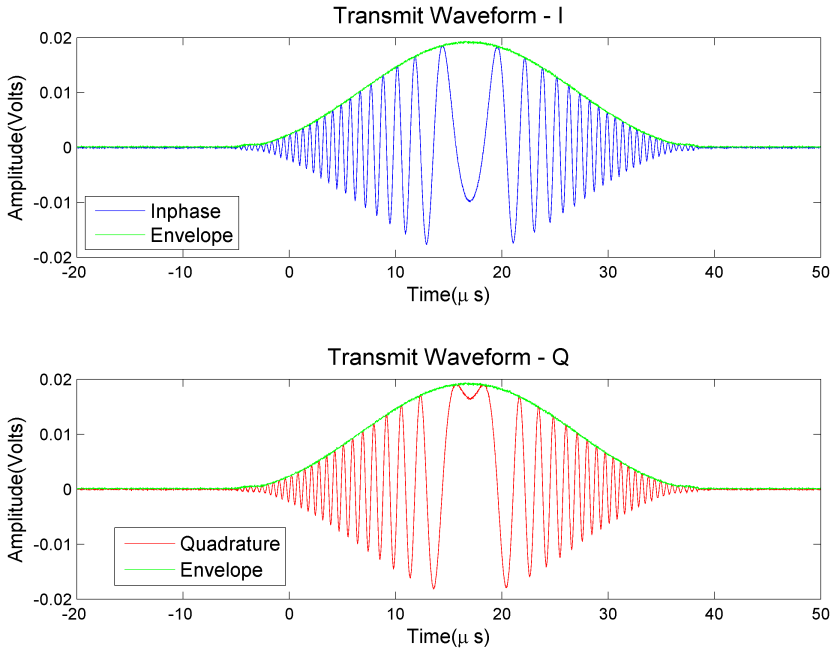

(a)

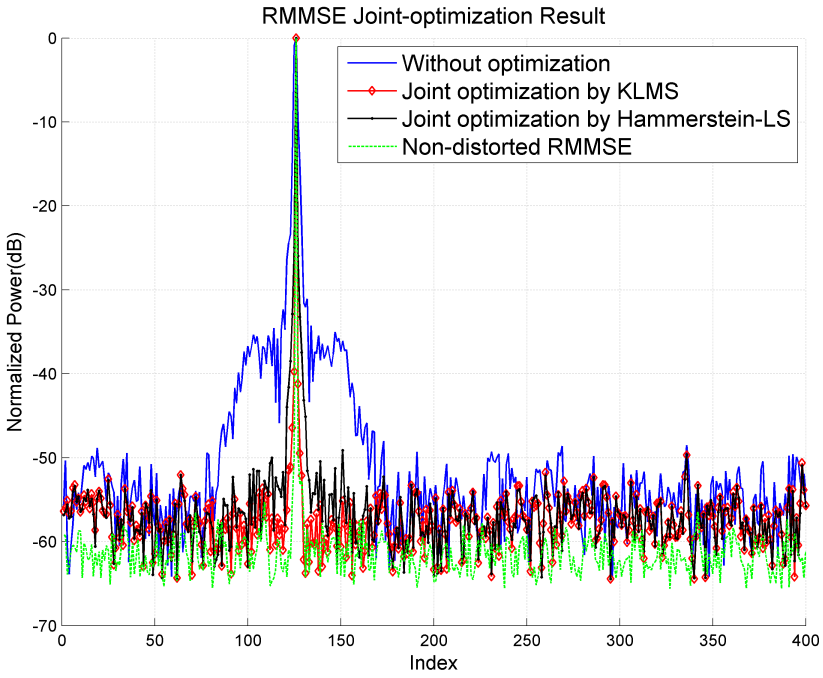

(b)

Figure 5.20: Joint optimization experiment Case # 1. (a) Windowed LFM waveform, (b) RMMSE JTRO comparison

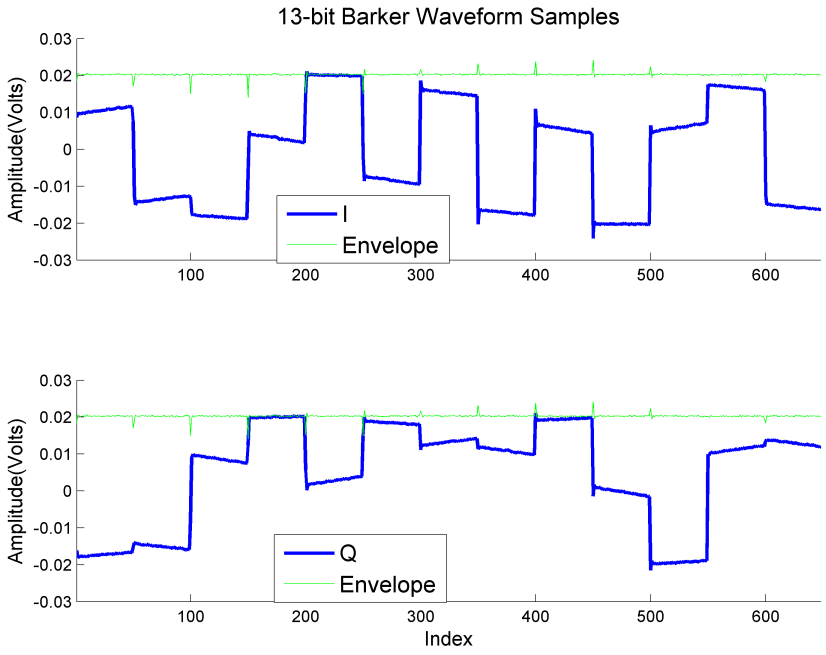

(a)

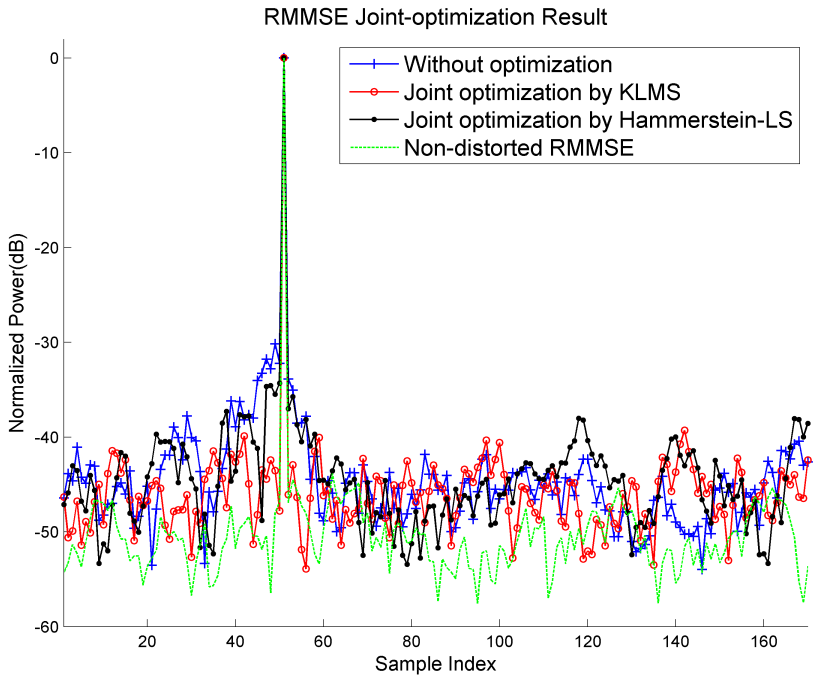

(b)

Figure 5.21: Joint optimization experiment Case # 2. (a) Barker-13 waveform, (b) RMMSE JTRO comparison

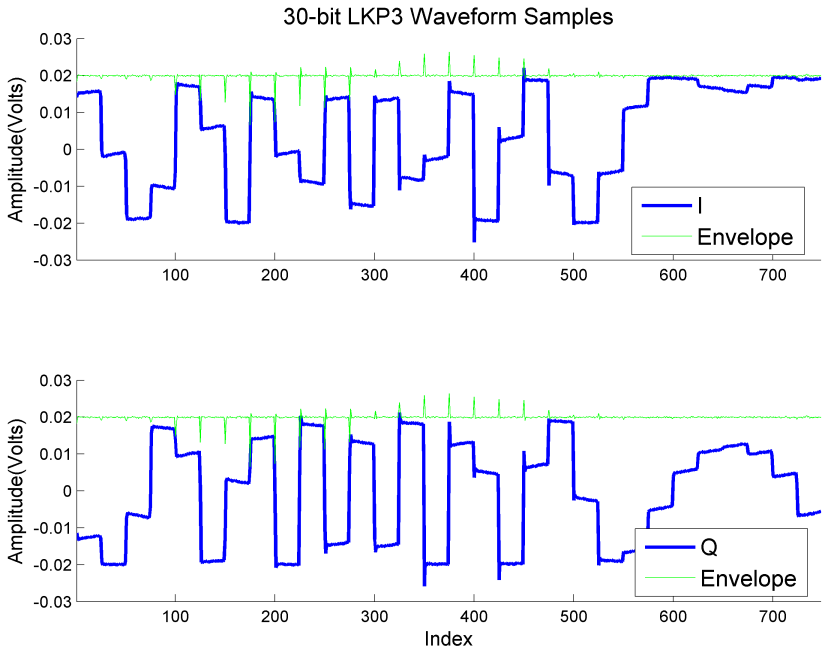

(a)

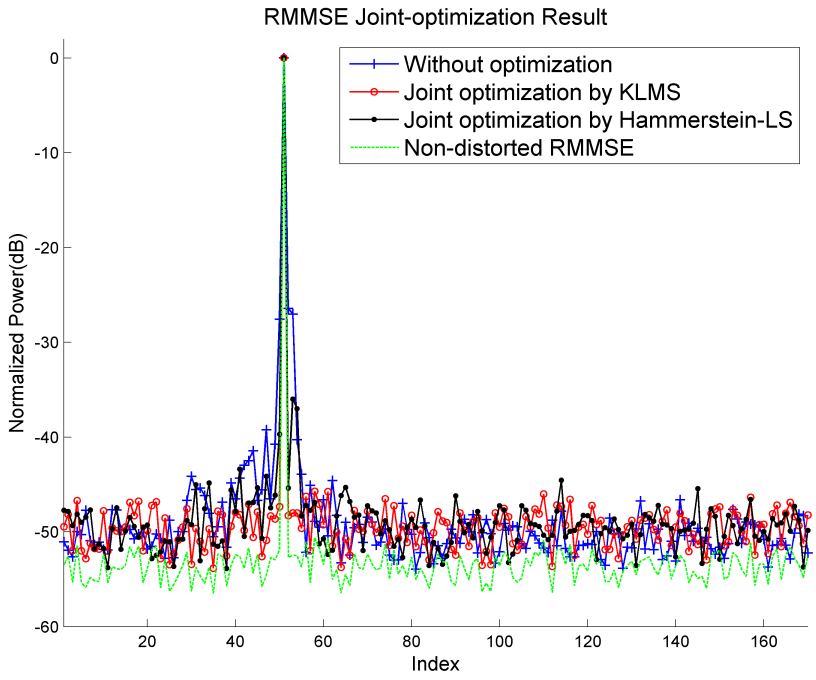

(b)

Figure 5.22: Joint optimization experiment Case # 3. (a) LKP3-30 waveform, (b) RMMSE JTRO comparison

be expected and how they can be achieved. First of all, it is the noise level of the transceiver system that determines the ultimate sidelobe mitigation level one can achieve. The JTRO processing can effectively remove the nonlinear distortion but will not breakthrough this hardware limitation. As pointed out before, our current JTRO testbed has a maximum SNR about 50 dB due to limitation of RF filtering. This is equivalent to an achievable PSL. Another factor that affects the sidelobe level is the pulse compression gain of the waveform. The compression gain is equal to the time-bandwidth (TB) product of the waveform. It is necessary to have a large TB product in order to achieve a very low sidelobe level. A waveform with low TB product is more easily affected by the noise interference. In our experiment, it is found that a TB product of at least 30 is necessary to achieve a good PSL (about 50 dB). The waveform in Case#1 and #3 has a TB product of 60 and 30, respectively. In Case #2, Barker code has a $TB = 13$, which suffers from the degraded sidelobe level about -40 dB.

In addition, several other aspects have to be pointed out for achieving good sidelobe mitigation and distortion suppression.

5.5.5.1 Level of Nonlinear Distortions

Depending on how severe of the nonlinear distortion, adjustment has to be made to the joint optimization mitigation algorithm. Fig. 5.20 is a scenario where the severe nonlinearity exists in the transmit chain (due to amplitude modulation). However, the same parameter setup will not apply to a moderate level of non-linearity case. Otherwise, the joint optimization will suffer from over-fitting and the convergence is not guaranteed. Fortunately, all those adjustment and parameter selection can be performed during system calibration, in which the waveform extraction, nonlinear modeling and RMMSE are conducted. The system will then proceed to the normal operation until the waveform is changed and calibration is needed again.

5.5.5.2 Selection of Model Paramaters

Another factor that affects the performance of joint-optimization is the selection of nonlinear model parameters. For Hammerstein-LS, based on simulation and processing of the measurement data, the recommended order for IIR, FIR and Polynomial is less than 11, 6 and 7 respectively. The corresponding coefficients for nonlinear model in Fig. 5.20(b) is listed in Table. 5.4

FIR(11)	*IIR(6+1)*	*Polynomial(7, odd)*
1.7677 - 0.0145i	-0.0439 + 0.0776i	0.02 - 0.02i
-0.8693 + 0.0185i	-0.0732 + 0.1957i	180.94 + 37.73i
0.8372 - 0.0198i	0.0356 + 0.1567i	-28.71 + 3.32i
-1.3757 - 0.0056i	-0.4784 - 0.1184i	-0.04 + 0.01i
0.8031 + 0.0466i	-0.5548 - 0.0496i	
-0.9381 + 0.0030i	-0.3940 - 0.2631i	
0.8715 - 0.0080i	-0.3611 + 0.1205i	
-0.4171 - 0.0397i		
0.5746 + 0.0133i		
-0.3295 - 0.0065i		
-0.0569 + 0.0113i		

Table 5.4: Hammerstein-LS coefficients in JTRO

For KLMS, one of the concerns is the selection of kernel functions. For example, the convergence of the polynomial kernel cannot be guaranteed due to the fact that polynomial kernel is not bell-shaped and cannot be considered as a weight function (Liu et al. 2010). In contrast, Gaussian kernel has a universal approximating capability and numerically stable. For Gaussian kernel, one of most important parameters is *kernel bandwidth*. The larger the kernel bandwidth, the better the nonlinear curve is concentrated, and the worse the degree of nonlinearity, vise versa. Simulation and

experiments suggest a kernel bandwidth from 1∼3 for the optimized performance. During the iterations process of KLMS, another important factor is the step size η. It is similar to that of LMS algorithm. A smaller η corresponds to a faster convergence speed but worse modeling accuracy. An $\eta \approx 0.8$ is found to obtain the best trade-off between convergence speed and accuracy. Table. 5.5 lists the KLMS coefficients in Case# 3.

Kernel Map	Weight	Kernel Map	Weight	Kernel Map	Weight	Kernel Map	Weight
$\kappa(s'_0, \cdot)$	1.0000	$\kappa(s'_8, \cdot)$	-0.1223	$\kappa(s'_{16}, \cdot)$	-0.0072	$\kappa(s'_{24}, \cdot)$	-0.0047
$\kappa(s'_1, \cdot)$	-0.1989	$\kappa(s'_9, \cdot)$	-0.0104	$\kappa(s'_{17}, \cdot)$	0.0084	$\kappa(s'_{25}, \cdot)$	-0.0114
$\kappa(s'_2, \cdot)$	-0.0177	$\kappa(s'_{10}, \cdot)$	-0.0033	$\kappa(s'_{18}, \cdot)$	-0.0056	$\kappa(s'_{26}, \cdot)$	-0.0071
$\kappa(s'_3, \cdot)$	0.1332	$\kappa(s'_{11}, \cdot)$	-0.0273	$\kappa(s'_{19}, \cdot)$	-0.0308	$\kappa(s'_{27}, \cdot)$	-0.0059
$\kappa(s'_4, \cdot)$	-0.1451	$\kappa(s'_{12}, \cdot)$	-0.0134	$\kappa(s'_{20}, \cdot)$	-0.0017	$\kappa(s'_{28}, \cdot)$	-0.0042
$\kappa(s'_5, \cdot)$	-0.5860	$\kappa(s'_{13}, \cdot)$	0.0789	$\kappa(s'_{21}, \cdot)$	0.0064	$\kappa(s'_{29}, \cdot)$	0.0054
$\kappa(s'_6, \cdot)$	-0.1071	$\kappa(s'_{14}, \cdot)$	0.0111	$\kappa(s'_{22}, \cdot)$	-0.0121		
$\kappa(s'_7, \cdot)$	0.1256	$\kappa(s'_{15}, \cdot)$	0.0121	$\kappa(s'_{23}, \cdot)$	0.0148		

Table 5.5: KLMS coefficients in Case# 3 (Only AM/AM coefficients are showed).

5.5.5.3 Impact of SNR

It has been pointed out in RMMSE implementation that the sidelobes can be suppressed as low as the level of the noise floor. For the case of a solitary target, the sidelobe level from the outputs of RMMSE processing in term of PSL is equivalent to the SNR. Even though the nonlinear distortions are mitigated by JTRO, the noise power still sets a lower bound for achievable PSL. In Fig. 5.20(b), the SNR is about 55 dB and about -55 dB sidelobe level is achieved. Fig. 5.23 shows two signals with different SNRs. The signal has a 70 MHz carrier frequency. The signal in Fig. 5.23(a)

is less noisy than that of Fig. 5.23(b). Fig. 5.23(c) is the comparison the joint optimization result based on these two input waveforms. It is clear that SNR has to be sufficiently high to avoid being a bottleneck of sidelobe mitigation performance.

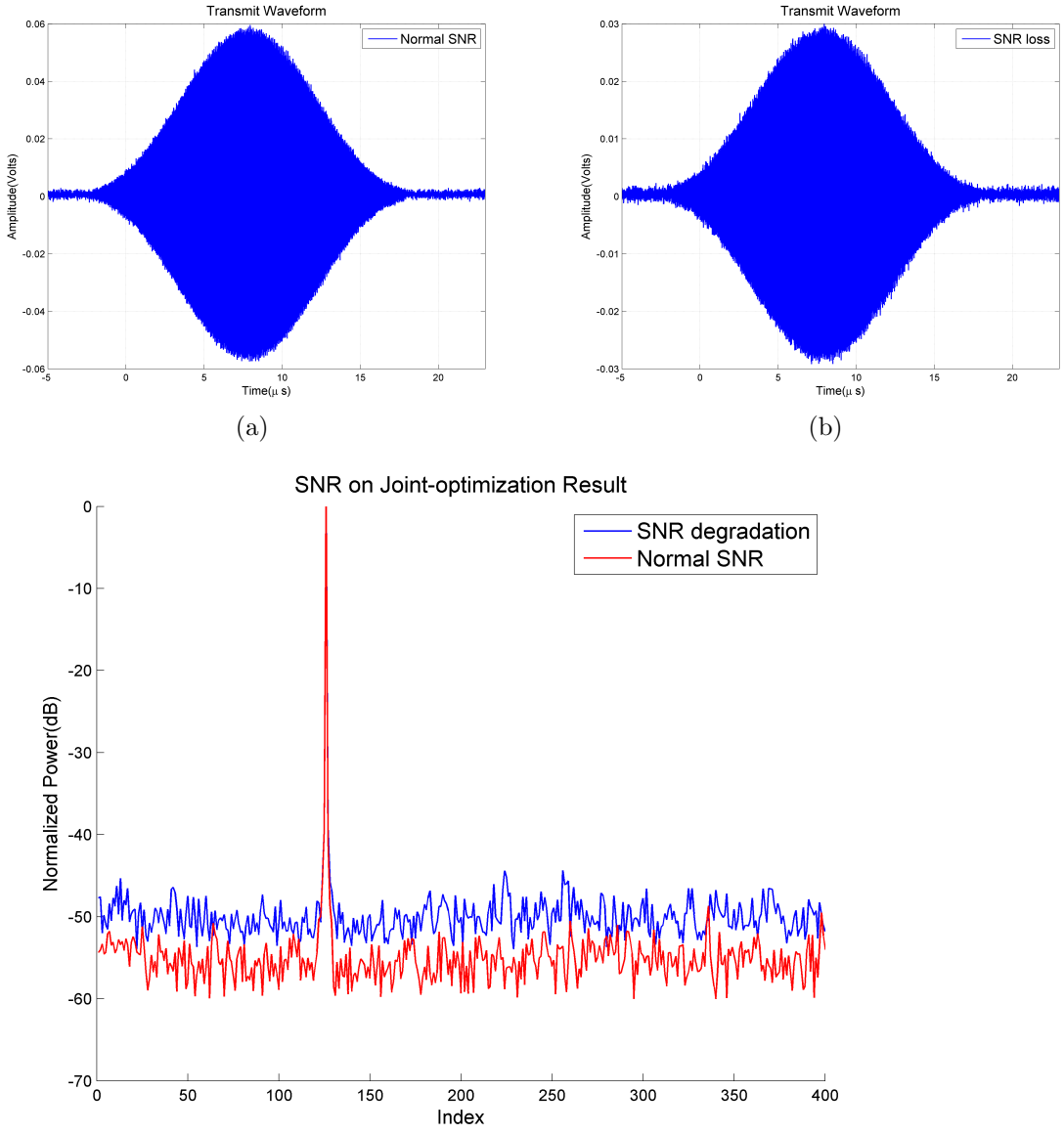

Figure 5.23: Hammerstein-LS algorithm in nonlinear modeling. (a) Signal with good SNR, (b) Signal with degraded SNR, (c) Comparison of joint optimization

Chapter 6

Conclusion

This dissertation describes the application of pulse compression in solid-state radars for both hard and distributed targets. Multi-functional waveform characterization and optimization are studied with application in ADS-B radar PPM/PM waveform design. Field experiment results are presented. Techniques to mitigate the sidelobe effects from both pulse compression process and antenna pattern are discussed. A 2D-RMMSE and 2D-LS algorithms are derived and verified with simulations based on realistic weather and target observation scenarios. Several implementation cases for the adaptive RMMSE algorithm are analyzed. Experiment results on practical radars are presented. To achieve better performance of target parameter estimation, a joint transmit and receive optimization scheme is proposed to suppress the nonlinear distortion in the radar transmit/receive chain. Joint optimization results on an experimental testbed for different scenarios are presented.

6.1 Contributions

The dissertation is organized as follows:

- Developed both statistical and deterministic models for a multi-functional PPM/random binary PM radar waveform. A practical controlled-searching and

mismatched filtering algorithm was formulated for waveform optimization, and a prototype radar sensor was developed for proof-of-concept experiments.

- Investigated the implementation of RMMSE algorithm to practical radars. Applied adaptive pulse compression algorithms to practical radar data. Developed pulse compression algorithms 2D-RMMSE and 2D-LS to mitigate both range sidelobe and antenna sidelobe effects. Verified the algorithm performance using realistic numerical weather simulation.

- Formulated the impact of nonlinear distortion on the sidelobe mitigation. Applied the KLMS to nonlinear modeling.

- Designed a JTRO technique to suppress sidelobe effect, in which both the adaptive pulse compression and nonlinear modeling are integrated. Designed a Ku-band spaceborne radar testbed and implemented JTRO algorithm.

6.2 Future Works

This dissertation can be extended with the following directions:

- Implement phase coding mismatched filtering technique to practical radars. As presented in Chapter 3, the range profiles obtained from mismatched filtering do not display significant improvement in terms of the target peak to sidelobe ratios, due to the fact that the outdoor environment is much more complicated than the RF chamber. The optimal mismatched filtering can be improved by incorporating the clutter and interference knowledge.

- Apply 2D-RMMSE and JTRO algorithms to practical radar data. Similar to waveform template issue in RMMSE implementation, the antenna pattern sensitivity of 2D-RMMSE has to be addressed. Dimension reduction technique for 2D-RMMSE is also required to further reduce the computational cost. For

JTRO, to achieve a better sidelobe mitigation, the noise floor the Ku-band testbed has to be further reduced. Hardware improvement has to be explored and more data are to be acquired and analyzed. In addition, JTRO is demonstrated to be able to handle a solitary target in Chapter 5, however, the performance of JTRO in more complicated target scenarios has not been fully evaluated.

- Real-time implementation of adaptive pulse compression on FGPA or DSP hardware. Although RMMSE has been applied to practical radar data processing, the real-time implementation has not been reported yet. This remains challenging because RMMSE requires matrix inversion operation, which is essential for FPGA implementation. Popular techniques used for matrix inversion includes QR, Cholesky and LU decompositions. The choice of a computing platform includes ASIC, DSPs and FPGAs.

Bibliography

Ackroyd, M. H. and F. Ghani, 1973: Optimum mismatched filters for sidelobe suppression. *Aerospace and Electronic Systems, IEEE Transactions on*, **(2)**, 214–218.

Ai, B., C. Yang, Z.and Pan, S. Tang, and T. Zhang, 2007: Analysis on lut based predistortion method for hpa with memory. *Broadcasting, IEEE Transactions on*, **53 (1)**, 127–131.

Alberts, T., P. Chilson, B. Cheong, R. Palmer, , and M. Xue, 2008: High resolution weather radar through pulse compression. *Symposium on Recent Developments in Atmospheric Applications of Radar and Lidar*.

Alberts, T. A., P. B. Chilson, and B. L. Cheong, 2007: Evaluation of binary phase coded pulse compression schemes using a time-series weather radar simulator. *33rd Conference on radar Meteorology*, 359–384.

Alper, P., 1965: A consideration of the discrete volterra series. *Automatic Control, IEEE Transactions on*, **10 (3)**, 322–327.

Arce, G. R., 2004: *Nonlinear Signal Processing - A Statistical Approach*. John Wiley & Sons, Inc, Hoboken, New Jersey, 484 pp.

Aschbacher, E., M. Steinmair, and M. Rupp, 2004: Iterative linearization methods suited for digital pre-distortion of power amplifiers. *Computing Processing (Hardware/Software) ; Signal Processing Analysis*, Vol. 2, 2198–2202.

Baden, J. and M. Cohen, 1990: Optimal peak sidelobe filters for biphase pulse compression. *Radar Conference, 1990., Record of the IEEE 1990 International*, IEEE, 249–252.

Baojun, Z., S. Caicheng, and H. Yueqiu, 2000: Neural network match filter of chirp pulse compression. *5th International Conference on Signal Processing Proceedings*, Vol. 3, 1872–1875.

Bharadwaj, N. and V. Chandrasekar, 2012: Wideband waveform design principles for solid-state weather radars. *Journal of Atmospheric and Oceanic Technology*, **29 (1)**, 14–31.

Blunt, S. D. and K. Gerlach, 2006: Adaptive pulse compression via mmse estimation. *IEEE Trans. on Aerospace and Electronic Systems*, **42 (2)**, 572–584.

Brown, S. T., B. H. Lambrigtsen, R. F. Denning, T. C. Gaier, P. P. Kangaslahti, B. H. Lim, J. M. Tanabe, and A. B. Tanner, 2011: The high-altitude mmic sounding radiometer for the global hawk unmanned aerial vehicle: Instrument description and performance. *Geoscience and Remote Sensing, IEEE Transactions on*, **49 (9)**, 3291–3301.

Bucci, N. J. and H. Urkowitz, 1993: Testing of doppler tolerant range sidelobe suppression in pulse compression meteorological radar. *Proceedings of IEEE Radar Conference*, 206–211.

Burges, C., 1998: A tutorial on support vector machines for pattern recognition. *Data Mining and Knowledge Discovery*, **2 (2)**, 121–167.

Cager, R., D. LaFlame, and L. Parode, 1978: Orbiter ku-band integrated radar and communications subsystem. *Communications, IEEE Transactions on*, **26 (11)**, 1604–1619.

Cheong, B. L., R. Kelley, R. D. Palmer, Y. Zhang, M. Yeary, and T.-Y. Yu, 2012: Px-1000: A solid-state polarimetric x-band weather radar and time-frequency multiplexed waveform for blind range mitigation. *IEEE Transactions on Instrumentation and Measurement, accepted*.

Cheong, B. L., R. D. Palmer, and M. Xue, 2008: A time series weather radar simulator based on high-resolution atmospheric models. *Journal of Atmospheric and Oceanic Technology*, **25 (2)**, 230–243.

Chrisikos, G., C. Clark, A. Moulthrop, M. Muha, and C. Silva, 1998: A nonlinear arma model for simulating power amplifiers. *Microwave Symposium Digest, 1998 IEEE MTT-S International*, Vol. 2, 733–736.

Cole, J., Elbert L., P. A. DeCesare, M. J. Martineau, R. S. Baker, and S. M. Buswell, 1998: Asr-12: a next generation solid state air traffic control radar. *Radar Conference, 1998*, 9–14.

Collins, T. and P. R. Atkins, 1999: Nonlinear frequency modulation chirps for active sonar. *IEE Proceedings - Radar, Sonar and Navigation*, **146 (6)**, 312–316.

Daniels, R. C. and V. Gregers-Hansen, 2005: Code inverse filtering for complete sidelobe removal in binary phase coded pulse compression systems. *International Radar Conference*, 256–261.

Davis, R. M., R. L. Fante, and R. P. Perry, 2007: Phase-coded waveforms for radar. *Aerospace and Electronic Systems, IEEE Transactions on*, **43 (1)**, 401–408.

de Witte, E. and H. D. Griffiths, 2004: Design of low-sidelobe pulse compression waveforms. *Electronics Letters*, **40 (22)**, 1448–1450.

Deng, H., 2004: Effective clean algorithms for performance-enhanced detection of binary coding radar signals. *Signal Processing, IEEE Transactions on*, **52 (1)**, 72–78.

Di Benedett, M. G., 2006: *UWB communication systems: a comprehensive overview*, Vol. 5. Hindawi Publishing Corporation.

Ding, L., G. Zhou, D. Morgan, Z. Ma, J. Kenney, J. Kim, and C. Giardina, 2007: A robust digital baseband predistorter constructed using memory polynomials. *Communications, IEEE Transactions on*, **52 (1)**, 159–165.

Doviak, R. and D. Zrnic, 1984: *Doppler Radar and Weather Observations*. Dover Publications, Inc, New York, 562pp.

Durnea, T. N., 2007: An investigation of spectral properties of ppm signals used in uwb systems. *Signals, Circuits and Systems, 2007. ISSCS 2007. International Symposium on*, IEEE, Vol. 2, 1–4.

Ewen, E. and D. Weiner, 1980: Identification of weakly nonlinear systems using input and output measurements. *Circuits and Systems, IEEE Transactions on*, **127 (6)**, 1255–1261.

Fakhouri, S., 1980: Identification of the volterra kernels of nonlinear systems. *Control Theory and Applications, IEE Proceedings D*, **127 (6)**, 296–304.

Felhauer, T., 1994: Design and analysis of new p(n,k) polyphase pulse compression codes. *IEEE Transactions on Aerospace and Electronic Systems*, **30 (3)**, 865–874.

Fischman, M., A. Berkun, W. Chun, E. Im, and R. Andraka, 2005: An onboard processor and adaptive scanning controller for the second-generation precipitation radar. *Geoscience and Remote Sensing, IEEE Transactions on*, **43 (4)**, 802–812.

Frank, R., 1963: Polyphase codes with good nonperiodic correlation properties. *Information Theory, IEEE Transactions on*, **9 (1)**, 43–45.

Franz, M. and B. Scholkopf, 2006: A unifying view of wiener and volterra theory and polynomial kernel regression. *Neural Computation*, **18 (12)**, 3097 – 3118.

Galati, G. and G. Pavan, 2011: On the signal design for multifunction/multi-parameter radar. *Microwaves, Radar and Remote Sensing Symposium*.

Galati, G., G. Pavan, and S. Scopelliti, 2010: Mpar: Waveform design for the weather function. *European Radar Conference*, 152–155.

Gard, K., H. Gutierrez, and M. Steer, 1999: Characterization of spectral regrowth in microwave amplifiers based on the nonlinear transformation of a complex gaussian process. *Microwave Theory and Techniques, IEEE Transactions on*, **47 (7)**, 1059–1069.

Gill, G. S., 1996: Simultaneous pulse compression and doppler processing with step frequency waveform. *Electronics Letters*, **32 (23)**, 2178–2179.

Glentis, G., P. Koukoulas, and N. Kalouptsidis, 1999: Efficient algorithms for volterra system identification. *Signal Processing, IEEE Transactions on*, **47 (11)**, 3042–3057.

Golomb, S. W. and G. Gong, 2005: *Signal design for good correlation: for wireless communication, cryptography, and radar*. Cambridge University Press.

Golub, G. H. and C. F. V. Loan, 1996: *Matrix Computations, 3rd Edition*. The Johns Hopkins University Press, Baltimore and London, 722pp.

Griep, K. R., J. A. Ritcey, and J. J. Burlingame, 1995: Poly-phase codes and optimal filters for multiple user ranging. *Aerospace and Electronic Systems, IEEE Transactions on*, **31 (2)**, 752–767.

Griffiths, H. and L. Vinagre, 1994: Design of low-sidelobe pulse compression waveforms. *Electronics Letters*, **30 (12)**, 1004–1005.

Griffiths, H. D., 1993: Ultra-low range sidelobe pulse compression for satellite-borne rain radar. *IEEE National Radar Conference*, 28–33.

Gutierrez, H., K. Gard, and M. Steer, 2000: Nonlinear gain compression in microwave amplifiers using generalized power-series analysis and transformation of input statistics. *Microwave Theory and Techniques, IEEE Transactions on*, **48 (10)**, 1774–1777.

Heimmer, J., 2008: Multi-mission phased array radar (mpar) national radar r&d project. *Proceedings of Systems, Applications and Technology Conference*, 1–2.

Herd, J. S., et al., 2010: Multifunction phased array radar (mpar) for aircraft and weather surveillance. *IEEE Radar Conference, 2010*, 945–948.

Heutmaker, M. S., E. Wu, and J. R. Welch, 1996: Envelope distortion models with memory improve the prediction of spectral regrowth for some rf amplifiers. *ARFTG Conference Digest-Fall, 48th*, Vol. 30, 10–15.

Hommel, H. and H.-P. P. Feldle, 2005: Current status of airborne active phased array (aesa) radar systems and future trends. *IEEE MTT-S International Microwave Symposium Digest, 2005*.

Huang, G.-B., P. Saratchandran, and N. Sundararajan, 2005: A generalized growing and pruning rbf (ggap-rbf) neural network for function approximation. *Neural Networks, IEEE Transactions on*, **16 (1)**, 57–67.

Hussain, M. G. M., 2007: Waveform design and modulation schemes for impulse communications and radar. *International Waveform Diversity and Design Conference, 2007*, 260–264.

Jang, W. M., B. Vojcic, and R. Pickholtz, 1998: Joint transmitter-receiver optimization in synchronous multiuser communications over multipath channels. *Signal Processing, IEEE Transactions on*, **46 (2)**, 269–278.

Jeruchim, M., P. Balaban, and K. Shanmugan, 2000: *Simulation of Communication Systems, 2nd Edition*. Kluwer academic, New York, 937 pp.

Johnston, J. and A. Fairhead, 1986: Waveform design and doppler sensitivity analysis for nonlinear fm chirp pulses. *Communications, Radar and Signal Processing*, **133 (2)**, 163–175.

kai Ruan, X. and Z.-Y. Zhang, 2009: Blind nonlinear channel equalization using kernel processing. *2nd International Congress on Image and Signal Processing*, 1–5.

Keeler, J. J. and C. A. Hwang, 1995: Pulse compression for weather radar. *International Radar Conference, 1995*, 529–535.

Ku, H. and J. Kenney, 2003: Behavioral modeling of nonlinear rf power amplifiers considering memory effects. *Microwave Theory and Techniques, IEEE Transactions on*, **51 (12)**, 2495–2504.

Kurdzo, J., B. L. Cheong, R. D. Palmer, G. Zhang, and J. B. Meier, 2013: An optimized pulse compression waveform for high-sensitivity weather radar observations. *29th Conference on Environmental Information Processing Technologies*.

Lavagetto, F., 1997: Time-delay neural networks for estimating lip movements from speech analysis: a useful tool in audio-video synchronization. *Circuits and Systems for Video Technology, IEEE Transactions on*, **7 (2)**, 786–800.

Levanon, N., 2005: Cross-correlation of long binary signals with longer mismatched filters. *Radar, Sonar and Navigation, IEE Proceedings-*, IET, Vol. 152, 377–382.

Levanon, N. and E. Mozeson, 2004: *Radar signals*. Wiley-Interscience.

Lewis, B. and F. Kretschmer, 1981: A new class of polyphase pulse compression codes and techniques. *Aerospace and Electronic Systems, IEEE Transactions on*, **(3)**, 364–372.

Lewis, J. M., S.Lakshmivarahan, and S. Dhall, 2006: *Dynamic Data Assimilation*. Cambridge University Press, 680 pp.

Li, L., G. M. Heymsfield, J. R. Carswell, D. H. Schaubert, J. P. Creticos, and M. Vega, 2008: High-altitude imaging wind and rain airborne radar (hiwrap). *Geoscience and Remote Sensing Symposium,IGARSS 2008*, Vol. 3, 354–357.

Liu, S. and J. Xiang, 1999: Novel method for super-resolution in radar range domain. *Radar, Sonar and Navigation, IEE Proceedings*, Vol. 146, 40–44.

Liu, W., I. Park, and J. Principe, 2009: An information theoretic approach of designing sparse kernel adaptive filters. *Neural Networks, IEEE Transactions on*, **20 (12)**, 1950–1961.

Liu, W., P. Pokharel, and J. Principe, 2008: The kernel least-mean-square algorithm. *Signal Processing, IEEE Transactions on*, **56 (2)**, 543 – 554.

Liu, W., J. C. Pr'incipe, and S. Haykin, 2010: *Kernel adaptive filtering - A Comprehensive Introduction*. John Wiley & Sons, Inc, Hoboken, New Jersey, 236 pp.

Luo, Z.-Q., T. Davidson, G. Giannakis, and K. M. Wong, 2004: Transceiver optimization for block-based multiple access through isi channels. *Signal Processing, IEEE Transactions on*, **52 (4)**, 1037–1052.

MacWilliams, J. J. and N. J. A. Sloane, 1976: Pseudo-random sequences and arrays. *Proceedings of the IEEE*, **64 (12)**, 1715–1729.

McManus, J. J., S. J. Frasier, and J. R. Carswell, 2008: Implementation of pulse compression on an airborne scatterometer. *IEEE International Geoscience and Remote Sensing Symposium*, 1418–1421.

Mudukutore, A. S., V. Chandrasekar, and J. J. Keeler, 1998: Pulse compression for weather radars. *IEEE Transactions on Geoscience and Remote Sensing*, **36 (1)**, 125–142.

O'Droma, N. and N. Mgebrishvili, 2005: Signal modeling classes for linearized ofdm sspa behavioral analysis. *Communications Letters, IEEE*, **9 (2)**, 127–129.

Ohora, F. and J. Bech, 2005: Operational use of pulse compression in weather radar. *32nd Conference on Radar Meteorology*.

Pan, J. and C.-H. Cheng, 2011: Wienerhammerstein model based electrical equalizer for optical communication systems. *Lightwave Technology, Journal of*, **29 (16)**, 2454–2459.

Pillai, U., K. Y. Li, I. Selesnick, and B. Himed, 2011: *Waveform Diversity, theory & application*. McGraw-Hill, New York, 306.

RTCA, 2003: Minimum operational performance standards for 1090 mhz extended squitter automatic dependent surveillance - broadcast (ads-b) and traffic information service - broadcast (tis-b). *RTCA*.

Rugh, W. J., 1981: *Nonlinear System Theory, the Volterra/Wiener Approach*. Johns Hopkins University Press, New York, 400 pp.

Salazar, J. L., R. Medina, and E. J. Knapp, 2008: Phase-tilt array antenna for dense distributed radar networks for weather sensing. *Proceedings of IGARSS 2008*, 318–321.

Saleh, A., 1981: Frequency-independent and frequency-dependent nonlinear models of twt amplifiers. *Communications, IEEE Transactions on*, **29 (11)**, 1715–1720.

Schreurs, D. and M. O'Droma, 2009: *RF Power Amplifier Behaviorial Modeling*. Cambridge University Press, New York, 289 pp, 14-15 pp.

Shin, H.-I., Y.-J. Ryoo, and J.-P. Lee, 2003: An implementation and analysis of programmable doppler filter bank using adsp21060s. *Seventh International Symposium on Signal Processing and Its Applications*, Vol. 1, 329–332.

Skolnik, M. I., 2002: *Introduction to Radar Systems, 3rd.* McGraw-Hill, New York, 772pp.

Skolnik, M. I., 2008: *Radar Handbook, 3rd.* McGraw-Hill, New York, 1352.

Surender, S. C. and R. M. Narayanan, 2006: Covert netted wireless noise radar sensor: Ofdma-based communication architecture. *Military Communications Conference, 2006. MILCOM 2006. IEEE*, IEEE, 1–7.

Tan, A. and K. Godfrey, 2001: The generation of binary and near-binary pseudo-random signals: an overview. *Instrumentation and Measurement Technology Conference, 2001. IMTC 2001. Proceedings of the 18th IEEE*, IEEE, Vol. 2, 766–771.

Tanner, A. B., S. L. Durden, R. F. Denning, E. Im, F.-K. K. Li, W. B. Ricketts, and W. J. Wilson, 1994: Pulse compression with very low sidelobes in an airborne rain mapping radar. *IEEE Transactions on Geoscience and Remote Sensing*, **32 (1)**, 211–213.

Taylor, J., John W. and G. Brunins, 1985: Design of a new airport surveillance radar (asr-9). *Proceedings of the IEEE*, Vol. 73, 284–289.

Taylor, J. D., 1995: *Introduction to ultra-wideband radar systems.* CRC Press.

Thompson, S. C. and J. P. Stralka, 2009: Constant envelope ofdm for power-efficient radar and data communications. *International Waveform Diversity and Design Conference, 2009*, 291–295.

Titlebaum, E. and N. DeClaris, 1966: Linear transformations of the ambiguity function. *Information Theory, IEEE Transactions on*, **12 (2)**, 120–125.

Vincent, N., J. Richard, N. Suinot, M. Yarwood, and C. Mavrocordatos, 1996: Pulse compression with -65 db sidelobe level for a spaceborne meteorological radar. *Geoscience and Remote Sensing Symposium*, Vol. 1, 490–492.

Wada, M., J. Horikomi, and F. Mizutani, 2009: Development of solid-state weather radar. *Proceedings of IEEE Radar Conference*, 1–4.

Wang, Y. and A. N. Akansu, 2012: Generalized dft based partial matched filter bank for doppler estimation. *46th Annual Conference on Information Sciences and Systems*, 1–6.

Wei, L. and L. K. Rasmussen, 1996: A near ideal noise whitening filter for an asynchronous time-varying cdma system. *Communications, IEEE Transactions on*, **44 (10)**, 1355–1361.

Win, M. Z., 1998: On the power spectral density of digital pulse streams generated by m-ary cyclostationary sequences in the presence of stationary timing jitter. *Communications, IEEE Transactions on*, **46 (9)**, 1135–1145.

Xiao, H., Q. Wu, and F. Li, 1998: A spectrum approach to the design of rf power amplifier for cdma signals. *Statistical Signal and Array Processing, 1998, Proceedings*, 13–135.

Xu, L., 2012: Compressive sensing in radar sensor networks using pulse compression waveforms. *2012 IEEE International Conference on Communications*, 794–798.

Xue, M., K. K. Droegemeier, and V. Wong, 2000: The advanced regional prediction system (arps): A multi-scale nonhydrostatic atmospheric simulation and prediction model. part i: Model dynamics and verification. *Meteorology and atmospheric physics*, **75**, 161–193.

Xue, M., K. K. Droegemeier, and V. Wong, 2001: The advanced regional prediction system (arps): A multi-scale nonhydrostatic atmospheric simulation and prediction model. part ii: Model physics and applications. *Meteorology and atmospheric physics*, **76**, 143–165.

Xue, M., K. K. Droegemeier, and V. Wong, 2003: The advanced regional prediction system (arps), storm-scale numerical weather prediction and data assimilation. *Meteorology and atmospheric physics*, **82**, 139–170.

Yang, J., 2007: A new doppler-tolerant polyphase pulse compression codes based on hyperbolic frequency modulation. *IEEE Radar Conference, 2007*, 265–270.

Zhang, Y., 2008: Development of a polarimetric space-time radar for airborne weather hazard monitoring. *13th Conference on Aviation, Range and Aerospace Meteorology*.

Zhang, Y., Y. Pan, S. Wang, Q. Zhao, D. S. Zrnic, and R. J. Doviak, 2011: Reconfigurable and scalable array element design for polarimetric multifunctional par. *IEEE Radar Conference, 2011*, 175–179.

Zhang, Y., J. Qiao, et al., 2008: Ads-b radar system. Google Patents, uS Patent 7,414,567, uS Patent 7,414,567.

Zhu, D., X. Dong, and W. Lin, 2008: Pulse compression with very low sidelobes in a spaceborne weather radar. *Geoscience and Remote Sensing Symposium, 2008. IGARSS 2008. IEEE International*, IEEE, Vol. 5, V–252.

Appendix A - List Of Symbols

$\mathbf{a}$	Antenna radiation pattern in form of azimuth response vector
a_n	Phase modulated code symbol
$\mathbf{A}$	Toeplitz matrix of the antenna pattern response
$c_{p,q}$	Nonlinear coefficient corresponds to q-th polynomial and p-th delay
ϵ_n	Pulse position modulated code symbol
f_i	The input-output nonlinear mapping at ith step of KLMS
η	Reflectivity
$g(r(t), \omega_0)$	Instantaneous AM/AM conversion at ω_0
k	Boltzmann's constant
K	Number of azimuth angles in one scan
K_ω	Dielectric factor of water
$\kappa(\mathbf{u}, \mathbf{u}^{'})$	Reproducing kernel with inputs $\mathbf{u}$ and $\mathbf{u}^{'}$
λ_i	ith eigenvalue for the reproducing kernel $\kappa(\cdot, \cdot)$
L	Number of range bins for each azimuth direction
M	Number of antenna pattern response angular samples
N	Number of transmitted waveform samples
ξ	Doppler shift in Ambiguity function

λ	Radar wavelength
τ	Pulse width
$r(t)$	The envelope amplitude component of PA input signal
s	Transmit waveform
$\bar{\mathbf{s}}$	Distorted transmit waveform
S	Transmit waveform matrix
$\bar{S}$	Distorted transmit waveform matrix
$\mathbf{S}$	Toeplitz matrix of the transmitted waveform
$S_u(f)$	The PSD of the signal $u(t)$
σ_u	The spectral width factor of $u(t)$
$\tilde{x}$	The baseband equivalent of x
X_{LS}	Least-Square estimate of X
$x(l,k)$	Ground truth (radar "impulse response signal without sidelobe interference) at the lth range bin and kth azimuth angle
$\rho(l,k)$	Power distribution of ground truth $\rho(l,k) = \|x(l,k)\|^2$
V	$(L+N-1)\times(K+M-1)$ Gaussian noise matrix
X	Complete ground truth impulse response matrix with size $L \times K$
X'_{LS}	Distorted Least-Square estimate of X
X^*	Complex conjugation of X
X^T	Transpose of X
X^H	Conjugate transpose (Hermitian) of X
$y(l,k)$	The received radar echoes from the lth range bin and kth azimuth angle

ϕ_i	ith eigenfunction for the reproducing kernel $\kappa(\cdot, \cdot)$
$\phi(t)$	The envelope phase component of PA input signal
$\Phi(r(t), \omega_0)$	Instantaneous AM/PM conversion at ω_0
χ	Ambiguity function

Appendix B - List Of Acronyms and Abbreviations

AF	Ambiguity Function
AMSE	Average Mean-Square-Error
AM/AM	Amplitude-to-Amplitude
AM/PM	Amplitude-to-Phase
ARPS	Advanced Regional Prediction System
ARRC	Advanced Radar Research Center
AWG	Arbitrary Waveform Generator
COTS	Commercial Off-The-Shelf
DPD	Digital Pre-Distortion
DSO	Digital Storage Oscilloscope
ECS	Extended Code Sequence
FIR	Finite Impulse Response
GaAs	Gallium Arsenide
HIWRAP	High-Altitude Imaging Wind and Rain Airborne Profiler
HPA	High-Power Amplifier
IF	Intermediate Frequency
IMP	Inter-Modulation Products
IQ	Inphase and Quadrature
ISL	Integrated Sidelobe Level
JTRO	Joint Transmitter and Receiver Optimization
KAF	Kernel Adaptive Filter

KLMS	Kernel Least-Mean-Square
LFSR	Linear Feedback Shift Register
LKP3	Lewis-Kretschmer P3
LOS	Line-Of-Sight
LRS	Linear Recursive Sequence
LS	Least-Square
MF	Matched Filter
MLB	Maximum Length Binary
MLS	Maximum Length Sequence
MMSE	Minimum Mean-Square Error
MPAR	Multifunction Phased Array Radar
NMSE	Normalized Mean-Square-Error
NLFM	NonLinear Frequency Modulation
OU	University of Oklahoma
PC	Phased-Coding
PM	Phase Modulation
PN	Pseudo-Noise
PPM	Pulse Position Modulation
PRT	Pulse Repetition Time
PSD	Power Spectrum Density
PSL	Peak Sidelobe Level
PX1000	Polarimetric X-band 1000
P1dB	1dB Compression
RMMSE	Re-iterative Minimum Mean-Square Error
RKHS	Reproducing Kernel Hilbert Space
SIR	Signal-to-Interference Ratio
SNR	Signal-to-Noise Ratio

SSPA	Solid-State Power Amplifier
TB	Time-Bandwidth product
TCAS	Traffic Collision Alerting System
TLS	Truncated Least-Square
TRMM	Tropical Rainfall Measuring Mission
Tx/Rx	Transmit/Receive
TWT	Traveling-Wave Tube
WSCS	Wide Sense CycloStationary
1D	One-Dimensional
2D	Two-Dimensional